

# Universal Moiré-Model-Building Method without Fitting: Application to Twisted MoTe<sub>2</sub> and WSe<sub>2</sub>

Yan Zhang,<sup>1,2,\*</sup> Hanqi Pi,<sup>1,2,\*</sup> Jiakuan Liu,<sup>1,2,\*</sup> Wangqian Miao,<sup>3</sup> Ziyue Qi,<sup>1,2</sup> Nicolas Regnault,<sup>4,5,6</sup> Hongming Weng,<sup>1,2,7</sup> Xi Dai,<sup>3</sup> B. Andrei Bernevig,<sup>5,8,9</sup> Quansheng Wu,<sup>1,2,†</sup> and Jiabin Yu<sup>10,5,‡</sup>

<sup>1</sup>*Beijing National Laboratory for Condensed Matter Physics and Institute of Physics, Chinese Academy of Sciences, Beijing 100190, China*

<sup>2</sup>*University of Chinese Academy of Sciences, Beijing 100049, China*

<sup>3</sup>*Department of Physics, The Hong Kong University of Science and Technology, Clear Water Bay, Hong Kong, China*

<sup>4</sup>*Center for Computational Quantum Physics, Flatiron Institute, 162 5th Avenue, New York, NY 10010, USA*

<sup>5</sup>*Department of Physics, Princeton University, Princeton, New Jersey 08544, USA*

<sup>6</sup>*Laboratoire de Physique de l'École normale supérieure, ENS, Université PSL, CNRS, Sorbonne Université,*

*Université Paris-Diderot, Sorbonne Paris Cité, 75005 Paris, France*

<sup>7</sup>*Songshan Lake Materials Laboratory, Dongguan, Guangdong 523808, China*

<sup>8</sup>*Donostia International Physics Center, P. Manuel de Lardizabal 4, 20018 Donostia-San Sebastian, Spain*

<sup>9</sup>*IKERBASQUE, Basque Foundation for Science, Bilbao, Spain*

<sup>10</sup>*Department of Physics, University of Florida, Gainesville, FL, USA*

(Dated: November 14, 2024)

We develop a comprehensive method to construct analytical continuum models for moiré systems directly from first-principle calculations *without any parameter fitting*. The core idea of this method is to interpret the terms in the continuum model as a basis, allowing us to determine model parameters as coefficients of this basis through Gram-Schmidt orthogonalization. We apply our method to twisted MoTe<sub>2</sub> and WSe<sub>2</sub> with twist angles ranging from 2.13° to 3.89°, producing continuum models that exhibit excellent agreement with both energy bands and wavefunctions obtained from first-principles calculations. We further propose a strategy to integrate out the higher-energy degrees of freedom to reduce the number of the parameters in the model without sacrificing the accuracy for low-energy bands. Our findings reveal that decreasing twist angles typically need an increasing number of harmonics in the moiré potentials to accurately replicate first-principles results. We provide parameter values for all derived continuum models, facilitating further robust many-body calculations. Our approach is general and applicable to any commensurate moiré materials accessible by first-principles calculations.

## I. INTRODUCTION

The groundbreaking discovery of superconductivity in twisted bilayer graphene [1–8] has ignited a surge of research into moiré materials as promising platforms for hosting a plethora of exotic correlated and topological phenomena [9–12]. Subsequently, experiments have observed (or showed strong signatures of) fractional Chern insulators in moiré materials [13–25], following earlier observations of fractional-quantum-Hall-like states in lattice systems under magnetic fields [26, 27].

A defining characteristic of moiré materials is their ability to host nearly flat topological bands, which significantly enhance electron-electron interactions and facilitate the emergence of correlated phases. This unique electronic structure underscores the necessity for robust single-particle models that can accurately capture the low-energy physics intrinsic to these systems. The continuum model, pioneered by Ref. [28–30] has become a fundamental tool in this context. Analogous to the  $k \cdot p$

models [31–33], the continuum model effectively encapsulates the physics arising from the large moiré lattice constant relative to the underlying atomic lattices.

Despite the generality afforded by symmetry considerations in formulating continuum models, the determination of precise model parameters remains a critical challenge. Traditionally, these parameters are extracted by fitting the continuum model's band structure to that obtained from Density Functional Theory (DFT) calculations [29, 34–48]. In graphene-based systems, parameters can be derived through Fourier analysis (or perturbation analysis) of hopping functions [29, 36, 38, 41, 49–56]. However, the determination of the hopping parameters in the hopping functions still require fitting to DFT results [57, 58], a process that can introduce significant uncertainties and inconsistencies.

Parameter fitting introduces several critical limitations: firstly, a model optimized solely for band structure alignment may fail to accurately reproduce the corresponding wavefunctions; secondly, when the number of moiré bands involved is large (for example, due to large fillings or strong interaction), achieving an exact match between model and DFT wavefunctions through fitting becomes very challenging due to the large number of needed parameters. Disparate parameter sets can lead to different flat band topology [29, 34, 40, 43–47, 59–

\* These authors contributed equally.

† quansheng.wu@iphy.ac.cn

‡ yujiabin@ufl.edu

[65] due to the different wavefunctions. Different wavefunctions can also lead to divergent predictions of the nature of correlated phases induced by interactions [43–45, 47, 48, 60–63, 66–93], since the wavefunctions directly determine the form of the projected interactions, which dominate the correlation physics in the moiré flat-band systems.

These challenges underscore the urgent need for a novel approach to constructing faithful continuum models that obviates the reliance on parameter fitting. Such an approach would not only enhance the accuracy and reliability of the models but also streamline the process of exploring and predicting new correlated and topological phenomena in moiré materials. Recently, directly Wannierization of the moiré DFT Hamiltonian has been done in Ref. [63], which can provide a precise numerical low-energy Hamiltonian. Nevertheless, this method cannot provide a continuum model, as the continuum model is built on plane wave basis instead of the moiré Wannier functions.

In this work, we introduce a universal framework for constructing *ab initio* continuum models for moiré materials, eliminating the need for parameter fitting. Our method leverages the fact that different terms in the continuum model serve as the basis of the Hamiltonian, and the model parameters are essentially the coefficients of the basis, which can be determined from DFT calculations via projections. The method removes the ambiguities and inaccuracies typically associated with traditional fitting procedures. Our method is complementary to Ref. [63].

To demonstrate the efficacy of our approach, we apply it to twisted bilayer  $\text{MoTe}_2$  ( $t\text{MoTe}_2$ ) and twisted bilayer  $\text{WSe}_2$  ( $t\text{WSe}_2$ ) with twist angles ranging from  $2.13^\circ$  to  $3.89^\circ$ . Our continuum models exhibit exceptional agreement with DFT results—for example, the maximal energy deviation is less than 0.5 meV for  $2.13^\circ t\text{MoTe}_2$  and 1.3 meV for  $2.13^\circ t\text{WSe}_2$  for the top four energy bands, and the wavefunction overlap probability exceeds 97% across all these bands, excluding the regions where bands touch. These results validate the accuracy and reliability of our continuum models, providing a reliable foundation for numerical studies of the correlated phases. Moreover, we propose a strategy to integrate out the higher-energy degrees of freedom to reduce the number of the terms (and thus parameters) in the model without sacrificing essential physical characteristics. This simplification produces a reduced continuum model that has smaller parameters; for example, the reduced continuum model for  $t\text{MoTe}_2$  has 23 parameters compared to 148 parameters of the full continuum model (148 parameters represent the minimum required to keep energy deviations below 0.5 meV and wavefunction overlaps above 97% for the top four energy bands). Notably, the reduced model still well capture the top three DFT bands. The reduced continuum model can facilitate future analytical studies.

All the parameter values of the full and reduced continuum models for  $t\text{MoTe}_2$  and  $t\text{WSe}_2$  with twist angles

ranging from  $2.13^\circ$  to  $3.89^\circ$  are provided in Tabs. III to XX and on GitHub [94]. The parameter values indicate that as the twist angle decreases, we typically need an increasing number of harmonics in the moiré potentials to capture the DFT results. For example, the number of intralayer (interlayer) harmonics for  $t\text{MoTe}_2$  increases from 4 (4) for  $3.89^\circ$  to 5 (6) for  $2.13^\circ$  for the full model, and increases from 1 (2) for  $3.89^\circ$  to 5 (4) for  $2.13^\circ$  for the reduced model.

## II. DFT-BASED STRUCTURAL AND ELECTRONIC CALCULATIONS

We first present a method for efficiently obtaining reliable electronic structures of moiré systems from first-principles calculations. We start by obtaining a relaxed structure of a moiré system. Traditional methods face convergence challenges when dealing with moiré systems due to the large number of atoms in the unit cell (e.g., 4326 atoms for a  $2.13^\circ t\text{MoTe}_2$ ). To address this, we employed a Machine Learning Force Field (MLFF) trained on ab-initio data [46, 47, 64, 95]. After using VASP’s MLFF module [96–101] to generate training data from molecular dynamics simulations, we then utilized Allegro [102], an E(3)-equivariant neural network, to train an accurate MLFF. Allegro’s architecture ensures that both the input and output of each neural network layer are equivariant under rotations, reflections, and translations in three-dimensional space. This capability allows our MLFF to accurately predict forces and energies while effectively handling the rotational and translational symmetries inherent in the relaxed structures of moiré systems.

After relaxing the crystal structures, we performed DFT calculations using OpenMX software [103–105] with norm-conserving pseudopotentials and localized basis functions, which is particularly efficient for large moiré systems due to its optimized handling of localized orbitals and its capability to handle large-scale computations. Consequently, we obtained an *ab initio* tight binding Hamiltonian based on non-orthogonal pseudo-atomic orbitals (PAOs), resulting in a generalized eigenvalue problem. Alternatively, other software packages using numerical atomic orbitals such as SIESTA [106] and ABACUS [107, 108] can also be used to perform these DFT calculations. A detailed description of the relaxation and DFT calculation methodologies can be found in App. [A]

Solving a generalized eigenvalue problem in moiré systems presents substantial computational challenges due to the Hamiltonian’s high dimensionality. To overcome this, we adopt the truncated atomic plane wave (TAPW) method, initially proposed to study twisted bilayer graphene systems in Ref. [109–111]. In this work, we extend this method to non-orthogonal basis.

Using  $t\text{MoTe}_2$  as a case study, where the low-energy physics is dominated by two atomic valleys (labeled by

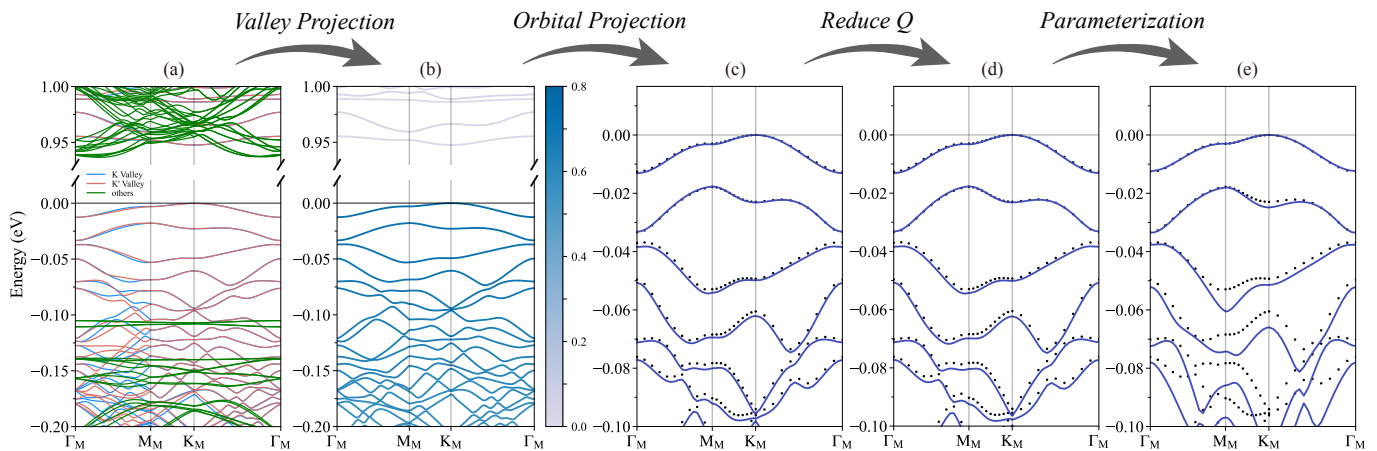


FIG. 1. **DFT to Reduced Model.** (a) Band structure of the full Hamiltonian for  $3.89^\circ$   $t\text{MoTe}_2$  computed using OpenMX. Blue lines denote the K valley, red lines represent the  $K'$  valley bands, and green lines correspond to the bands of other valleys, including the  $\Gamma$  valley. (b) Valley-projected band structure obtained via the Truncated Atomic Plane Wave (TAPW) method, exclusively displaying the K valley. The color intensity indicates the contribution of Mo's  $d_{xy}$  and  $d_{x^2+y^2}$  orbitals to each band. (c) Orbital projection focusing solely on Mo's  $d_{xy}$  and  $d_{x^2+y^2}$  orbitals. (d) Band structure derived from the reduced DFT model. (e) Band structure obtained from the reduced continuum model. In panels (c) to (e), the black dotted lines correspond to the DFT results for comparison.

$\pm K$ ), we project the *ab initio* tight binding Hamiltonian onto a group of atomic plane waves localized around the K valley to significantly reduce computational costs (the  $-K$  valley Hamiltonian can be obtained using time-reversal symmetry), as shown in Fig. 1(a) to (b). Specifically, Fig. 1(a) displays the full Hamiltonian's band structure of  $3.89^\circ$   $t\text{MoTe}_2$  computed using OpenMX, while Fig. 1(b) presents the K valley-projected band structure. This approach effectively captures the essential electronic properties of the moiré system with reduced computational complexity.

The atomic plane wave basis for the  $l$ -th layer at the K valley is defined as:

$$|\psi_{l,\tilde{\mathbf{G}}_l,\alpha}(\mathbf{k})\rangle = \frac{1}{\sqrt{N_m N_a}} \sum_{\mathbf{I},i} e^{i(\mathbf{k}+\tilde{\mathbf{G}}_l)(\mathbf{R}_I+\tau_{i\alpha})} |\phi_{\alpha,\mathbf{R}_I+\tau_{i\alpha}}\rangle, \quad (1)$$

where  $\tilde{\mathbf{G}}_l$  denotes a moiré reciprocal lattice vector for the  $l$ -th layer in the DFT convention (which has a large shift compared to the model convention as discussed in Sec. III), and  $\mathbf{k}$  represents the momentum in the first moiré Brillouin zone.  $\mathbf{R}_I$  is the moiré lattice vector,  $\tau_{i\alpha}$  indicates the displacement of the  $\alpha$ -th orbital in the  $i$ -th non-twisted unit cell of the  $l$ -th layer,  $|\phi_{\alpha,\mathbf{R}_I+\tau_{i\alpha}}\rangle$  is the  $\alpha$ -th PAO centered at  $\mathbf{R}_I + \tau_{i\alpha}$ .  $N_m$  represents the number of moiré unit cells and  $N_a$  refers to the number of non-twisted unit cells within a single moiré unit cell.

The matrix element of the Hamiltonian and overlap integral can be obtained under the TAPW basis defined

in Eq. (1),

$$\begin{aligned} H_{l\alpha,l'm\beta}^{\text{TAPW}}(\mathbf{k}) &= \sum_{ij} X_{li\alpha,l'n\alpha}^\dagger H_{li\alpha,l'j\beta}(\mathbf{k}) X_{l'j\beta,lm\beta}, \\ S_{l\alpha,l'm\beta}^{\text{TAPW}}(\mathbf{k}) &= \sum_{ij} X_{li\alpha,l'n\alpha}^\dagger S_{li\alpha,l'j\beta}(\mathbf{k}) X_{l'j\beta,lm\beta}, \end{aligned} \quad (2)$$

where  $H(\mathbf{k})$  and  $S(\mathbf{k})$  represent the full non-orthogonal *ab initio* tight binding matrix and overlap matrix, respectively, and  $X$  denotes the plane wave projector under continuum approximation [109]. Eq. (2) represents for an unitary transformation when all atomic plane waves are preserved. However, in moiré systems, we can truncate the atomic plane waves near specific atomic valley we concern to simplify the problem. The explicit expressions for  $H(\mathbf{k})$ ,  $S(\mathbf{k})$ , and  $X$ , along with further details on the TAPW method, are provided in App. [A]. By defining the normalized Hamiltonian as:

$$H_{\text{DFT}}(\mathbf{k}) = (S^{\text{TAPW}}(\mathbf{k}))^{-1/2} H^{\text{TAPW}}(\mathbf{k}) (S^{\text{TAPW}}(\mathbf{k}))^{-1/2}, \quad (3)$$

we can reduce the generalized eigenvalue problem to a standard eigenvalue problem.

### III. CONSTRUCTING CONTINUUM MODEL

Based on DFT calculations, we propose a general method of constructing continuum model without parameter fitting for all twisted materials. We first outline the workflow of the general method in Fig. 2. After performing DFT calculations on the relaxed crystal structure and TAPW method, we get a  $H_{\text{DFT}}$  that focus on the specific valley. Then we use second-order perturbation theory to

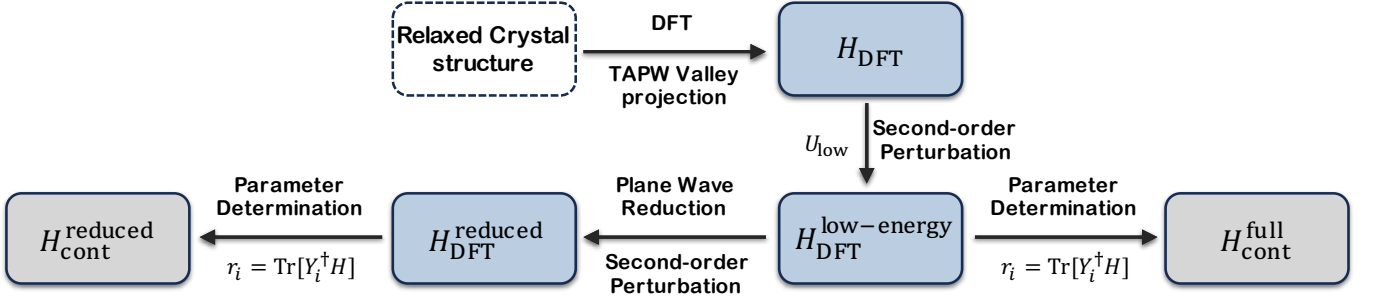


FIG. 2. **Workflow overview.** A workflow to obtain the continuum model directly from DFT calculations without parameters fitting.

obtain a low-energy DFT Hamiltonian  $H_{\text{DFT}}^{\text{low-energy}}$  from the TAPW DFT Hamiltonian  $H_{\text{DFT}}$ . Then, we use the orthogonalization and projection method to determine the parameter values of a full continuum model  $H_{\text{cont}}^{\text{full}}$  from  $H_{\text{DFT}}^{\text{low-energy}}$ . Given that fact that the full continuum model may require a large number of parameters, we use the second-order perturbation theory to integrate out the high-energy degrees of freedom, which can reduce the number of plane waves in  $H_{\text{DFT}}^{\text{low-energy}}$  and give a reduced DFT Hamiltonian  $H_{\text{DFT}}^{\text{reduced}}$ . (The procedure was also called Löwdin’s partitioning method [112].) We can again use the orthogonalization and projection method to determine the parameter values of a reduced continuum model  $H_{\text{cont}}^{\text{reduced}}$  from  $H_{\text{DFT}}^{\text{reduced}}$ . We provide more details for the general methods in App. [C].

In the rest of this section, we will illustrate the method by considering two specific cases, *i.e.*, AA-stacked  $t\text{MoTe}_2$  and  $t\text{WSe}_2$ . In AA-stacked  $t\text{MoTe}_2$  and  $t\text{WSe}_2$ , the low-energy moiré bands originate from the highest valence bands near the K and  $-\text{K}$  valleys in each layer. Strong spin-orbit coupling constrains the spin-up states to the K valley and the spin-down states to the  $-\text{K}$  valley. This section focuses on the continuum model at the K valley, as the  $-\text{K}$  valley model can be derived through time-reversal symmetry [113, 114].

### A. Low-energy DFT Hamiltonian

We note that the DFT Hamiltonian around the K valley can be expressed as:

$$\begin{aligned}
 H_{\text{DFT}} &= \sum_{\mathbf{k}} \sum_{l,l'} \sum_{\tilde{\mathbf{G}}_l, \tilde{\mathbf{G}}_{l'}} \sum_{\alpha_1 \alpha_2} c_{\mathbf{k}+\tilde{\mathbf{G}}_l, \alpha_1}^\dagger c_{\mathbf{k}+\tilde{\mathbf{G}}_{l'}, \alpha_2} [H_{\text{DFT}}(\mathbf{k})]_{l\tilde{\mathbf{G}}_l, \alpha_1, l'\tilde{\mathbf{G}}_{l'}, \alpha_2} \\
 &= \sum_{\mathbf{k}} \sum_{\mathbf{Q}_1, \mathbf{Q}_2} \sum_{\alpha_1 \alpha_2} c_{\mathbf{k}+\mathbf{K}_{l_{\mathbf{Q}_1}} - \mathbf{Q}_1, \alpha_1}^\dagger c_{\mathbf{k}+\mathbf{K}_{l'_{\mathbf{Q}_2}} - \mathbf{Q}_2, \alpha_2} [H_{\text{DFT}}(\mathbf{k})]_{\mathbf{Q}_1 \alpha_1, \mathbf{Q}_2 \alpha_2} \ ,
 \end{aligned} \tag{4}$$

where  $c_{\mathbf{k}+\tilde{\mathbf{G}}_l, \alpha}^\dagger$  denotes the DFT basis,  $\tilde{\mathbf{G}}_l$  is defined in Eq. (1), and  $\mathbf{K}_l$  represents the monolayer K-point of the  $l$ -th layer.  $\mathbf{Q}$  is a combination of the layer index and  $\tilde{\mathbf{G}}_l$ , and  $l_{\mathbf{Q}}$  indicates the layer that  $\mathbf{Q}$  corresponds to. Specifically, we have  $\mathbf{Q} = -\tilde{\mathbf{G}}_{l_{\mathbf{Q}}} + \mathbf{K}_{l_{\mathbf{Q}}}$ . The DFT basis include  $N_\alpha$  spin- $\uparrow$  orbitals per monolayer unit cell. For instance, in  $t\text{MoTe}_2$  calculations, we use the PAO basis sets Mo- $s3p2d2$  and Te- $s3p2d2f1$ , yielding a total of  $N_\alpha = 71$  functions. The basis selection adheres to OpenMX guidelines, with alternatives detailed in App. [A].

The DFT Hamiltonian in Eq. (4) contains a lot of high-energy degrees of freedom that are irrelevant to the low-energy physics of interest. To simplify Eq. (4), we recall that the low-energy physics happens among the low-energy states of monolayer Hamiltonians—we al-

ways choose the low-energy states of monolayer Hamiltonians as the basis of the continuum model. In other words, the most dominant energy scale in the continuum model is the kinetic energy directly inherited from the monolayer Hamiltonians, which do not couple different  $\mathbf{Q}$ ’s for a fixed  $\mathbf{k}$ . Therefore, to isolate the low-energy states, we can simply diagonalize each  $N_\alpha \times N_\alpha$  block of  $H_{\text{DFT}}(\mathbf{k})$  for a fixed  $\mathbf{Q}$ , denoted as  $D_{\mathbf{Q}}(\mathbf{k})$  with elements  $[D_{\mathbf{Q}}(\mathbf{k})]_{\alpha_1, \alpha_2} = [H_{\text{DFT}}(\mathbf{k})]_{\mathbf{Q}\alpha_1, \mathbf{Q}\alpha_2}$ . This yields eigenvalues  $\lambda_n^{k, \mathbf{Q}}$  and eigenvectors  $U_n^{k, \mathbf{Q}}$ . For each  $\mathbf{k}$  and  $\mathbf{Q}$ , we identify a single eigenvalue close to the Fermi level and distinctly separated from other states. These states are illustrated with green dots in Fig. 3, which shows the eigenvalues of each  $\mathbf{Q}$ -block of  $H_{\text{DFT}}(\Gamma_M)$ . The corresponding eigenvector,  $U_{\text{low}}^{k, \mathbf{Q}}$ , is then used to construct

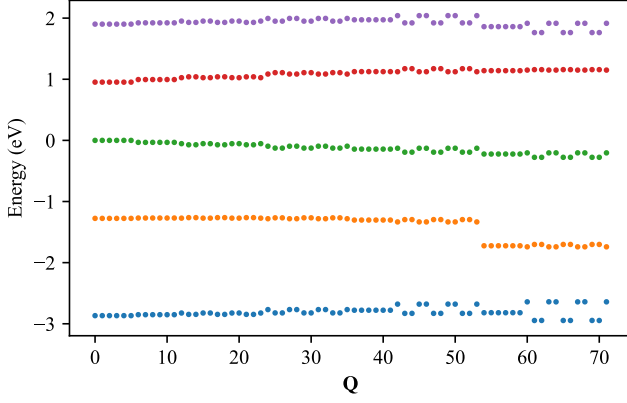


FIG. 3. **Eigenvalues of each diagonal block of  $H_{\text{DFT}}(\mathbf{k}_0)$  of  $2.13^\circ$   $t\text{MoTe}_2$ .** The horizontal axis represents the  $\mathbf{Q}$ -label index, and the vertical axis shows the energy spectrum obtained by diagonalizing each  $\mathbf{Q}$ -block ( $D_{\mathbf{Q}}(\mathbf{k}_0)$ ) from  $H_{\text{DFT}}(\mathbf{k}_0)$ . The green states near the Fermi level, which is set to zero, correspond to the energy states of interest. Here,  $\mathbf{k}_0$  is chosen at the  $\Gamma_M$  point. The  $\mathbf{Q}$ -label index corresponds to specific  $\mathbf{Q}$ -points, which are detailed in Fig. 10 of Appendix.

the low-energy basis:

$$\psi_{\mathbf{k},\mathbf{Q}}^\dagger = \sum_{\alpha} c_{\mathbf{k}+\mathbf{K}_l-\mathbf{Q},\alpha}^\dagger \left[ U_{\text{low}}^{\mathbf{k},\mathbf{Q}} \right]_{\alpha} . \quad (5)$$

$U_{\text{low}}^{\mathbf{k},\mathbf{Q}}$  is dominated by the orbital  $d_{xy} + id_{x^2+y^2}$ , consistent with the orbital structure of the top valence band around K in monolayer  $\text{MoTe}_2$  [40, 43–46, 48, 60, 62, 64, 66–69, 74, 114–116]. For convenience, we fix the  $d_{xy}$  component of the eigenvector  $U_{\text{low}}^{\mathbf{k},\mathbf{Q}}$  to be positive definite by fixing the random phase of  $U_{\text{low}}^{\mathbf{k},\mathbf{Q}}$ . Consequently,  $\psi_{\mathbf{k},\mathbf{Q}}^\dagger$  has exactly the same symmetry representations as the continuum basis used in the construction of the moiré continuum model [40, 43–46, 48, 60, 62, 64, 66–69, 74, 114–116]. Thus,  $\psi_{\mathbf{k},\mathbf{Q}}^\dagger$  in Eq. (5) serves as the basis for the continuum model employed in these studies [40, 43–46, 48, 60, 62, 64, 66–69, 74, 114–116]. Using the continuum basis, we can further employ second-order perturbation to derive the low-energy Hamiltonian  $h_{\text{DFT}}(\mathbf{k})$ , resulting in the following low-energy model in the continuum basis directly from DFT calculations:

$$H_{\text{DFT}}^{\text{low-energy}} = \sum_{\mathbf{k}} \sum_{\mathbf{Q}_1, \mathbf{Q}_2} \psi_{\mathbf{k},\mathbf{Q}_1}^\dagger [h_{\text{DFT}}(\mathbf{k})]_{\mathbf{Q}_1, \mathbf{Q}_2} \psi_{\mathbf{k},\mathbf{Q}_2} . \quad (6)$$

(See App. [C] for the perturbation details.) As illustrated in Fig. 1(c),  $H_{\text{DFT}}^{\text{low-energy}}$  reproduces the DFT band structure with very high accuracy, offering a precise framework for further many-body calculations if paired with a normal-ordered interaction term to avoid double counting of the interactions already present in the DFT. However, there is a limitation in directly using  $h_{\text{DFT}}(\mathbf{k})$ —the momentum mesh we use for the many-body calculation must be the same as or a subset of the DFT momentum

mesh for  $h_{\text{DFT}}(\mathbf{k})$ .

To address this issue, we derive a continuum model, which enables calculations on arbitrary meshes. We note that the real-space form of the K-valley continuum Hamiltonian,  $H_{\text{cont,K}}$ , in general reads

$$H_{\text{cont,K}} = \sum_{M_x, M_y \in \mathbb{N}} \sum_{l, l'} \int d^2r \left( i^{M_x+M_y} \partial_x^{M_x} \partial_y^{M_y} \psi_{\mathbf{r},\mathbf{K}_l}^\dagger \right) t_{ll'}^{M_x M_y}(\mathbf{r}) \psi_{\mathbf{r},\mathbf{K}_{l'}} , \quad (7)$$

where  $\mathbb{N}$  is the set of non-negative integers. In Eq. (7), derivatives on  $t$  terms are not explicitly required since differentiating a potential still yields a potential. Derivatives on  $\psi_{\mathbf{r},\mathbf{K}_l}$  terms are not explicitly included since they relate to derivatives on  $\psi_{\mathbf{r},\mathbf{K}_l}^\dagger$  and  $t$  terms by integration by parts.

Under the continuum approximation, we have  $H_{\text{DFT}}^{\text{low-energy}} = H_{\text{cont,K}}$ , and thus  $h_{\text{DFT}}(\mathbf{k})$  can be approximated by Fourier transformation of Eq. (7), expressed as:

$$[h_{\text{DFT}}(\mathbf{k})]_{\mathbf{Q}\mathbf{Q}'} = \sum_{M_x, M_y \in \mathbb{N}} \sum_{l, l'} \sum_{\mathbf{G}_M} r_{ll',\mathbf{G}_M}^{M_x M_y} \left[ Y_{ll',\mathbf{p}}^{M_x M_y}(\mathbf{k}) \right]_{\mathbf{Q}\mathbf{Q}'} , \quad (8)$$

where  $\mathbf{p} = \mathbf{K}_l - \mathbf{K}_{l'} + \mathbf{G}_M$  for simplicity,  $\mathbf{G}_M$  is the Moiré reciprocal lattice vector, and

$$\left[ Y_{ll',\mathbf{p}}^{M_x M_y}(\mathbf{k}) \right]_{\mathbf{Q}\mathbf{Q}'} = \delta_{l_{\mathbf{Q}}, l} \delta_{l_{\mathbf{Q}'}, l'} (\mathbf{k}-\mathbf{Q})_x^{M_x} (\mathbf{k}-\mathbf{Q})_y^{M_y} \delta_{\mathbf{Q}, \mathbf{Q}'+\mathbf{p}} . \quad (9)$$

Here  $|\mathbf{p}|$  determines the harmonics of the moiré potential, since  $\mathbf{p}$  is the momentum difference between the creation and annihilation operators. Specifically, when  $l = l'$  and  $\mathbf{G}_M = 0$ ,  $\mathbf{p} = 0$  and the term represents the kinetic energy within each individual layer; when  $l = l'$  but  $\mathbf{G}_M \neq 0$ ,  $\mathbf{p} = \mathbf{G}_M$  and the term describes intralayer moiré potential; finally, when  $l \neq l'$ ,  $\mathbf{p}$  is again nonzero and the term describes interlayer moiré coupling. (See details in App. [C].) In Sec. VA, we provide a relation between  $r_{ll',\mathbf{G}_M}^{M_x M_y}$  and the commonly used notations in the literature.

## B. Determining Parameter Values

The goal is to determine the values of  $r_{ll',\mathbf{G}_M}^{M_x M_y}$ . If the  $\mathbf{Q}$  lattice were infinite, we could determine the values of all  $r_{ll',\mathbf{G}_M}^{M_x M_y}$  at a fixed  $\mathbf{k} = \mathbf{k}_0$ : we first apply the Gram-Schmidt process to orthogonalize the  $Y$  terms in Eq. (9), and then project  $h_{\text{DFT}}$  onto the orthogonalized  $Y$  terms by taking the trace between them to determine  $r_{ll',\mathbf{G}_M}^{M_x M_y}$ , as discussed in Sec. VB. Although an infinite  $\mathbf{Q}$  lattice is not feasible in practice, we adapt this method to finite sets of  $(M_x, M_y, l, l', \mathbf{G}_M)$  terms, providing the corresponding  $r_{ll',\mathbf{G}_M}^{M_x M_y}$  values. Should a single  $\mathbf{k}$  point prove

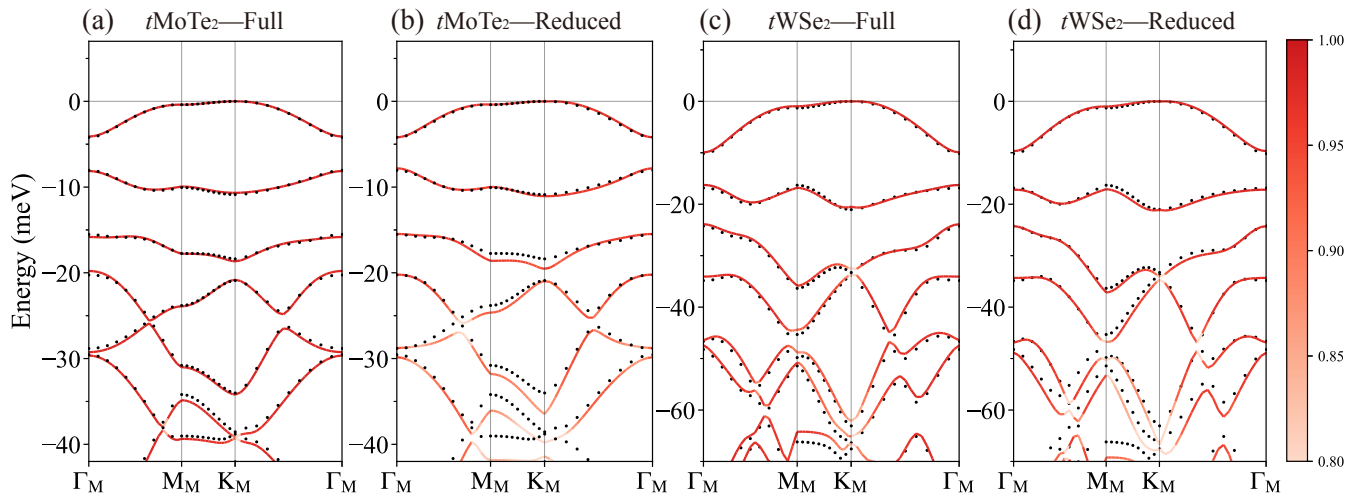


FIG. 4. **Continuum Models for  $2.13^\circ$   $t\text{MoTe}_2$  and  $t\text{WSe}_2$ .** (a) Full continuum model of  $t\text{MoTe}_2$ . (b) Reduced continuum model of  $t\text{MoTe}_2$ . (c) Full continuum model of  $t\text{WSe}_2$ . (d) Reduced continuum model of  $t\text{WSe}_2$ . Black lines represent the K valley bands calculated using the TAPW method, while red lines depict bands computed by the continuum model. The gradient from dark to light red in the red lines illustrates the overlap probability between the continuum model wavefunctions and the TAPW wavefunctions for each corresponding band. The full lattice includes harmonics up to the 8th order, corresponding to the  $\tilde{\mathbf{G}}$  vectors used in the TAPW method, whereas the reduced lattice includes harmonics up to the 3rd order.

insufficient, we can include multiple  $\mathbf{k}$  points (in a direct sum manner) to accurately determine the parameter values (see App. [C] for details). Notably, this procedure requires no parameter fitting, as  $h_{\text{DFT}}(\mathbf{k})$  is derived directly from DFT calculations. This yields a continuum model with the same  $\mathbf{Q}$  lattice as the DFT Hamiltonian, termed the “full model”.

To demonstrate our method, we present the full continuum models for  $2.13^\circ$   $t\text{MoTe}_2$  and  $t\text{WSe}_2$  in Fig. 4(a,c), where the results for  $t\text{MoTe}_2$  and  $t\text{WSe}_2$  of twisted angles from  $2.45^\circ$  to  $3.89^\circ$  are displayed in Figs. 11 to 13. As shown in Fig. 4(a,c), the low-energy bands and their eigen-wavefunctions calculated from the full continuum models exhibit excellent agreement with the DFT results. Specifically, the maximum energy difference between the full continuum model and DFT bands is less than 0.5 meV and 1.3 meV for  $t\text{MoTe}_2$  and  $t\text{WSe}_2$ , respectively; the minimum wavefunction overlap probability (excluding the band-touching regions) exceeds 97% for the top four bands for both  $t\text{MoTe}_2$  and  $t\text{WSe}_2$ . The wavefunction match is also evident in the Berry curvature distributions shown in Fig. 5. Interestingly, the top three bands of  $2.13^\circ$   $t\text{MoTe}_2$  all have Chern number 1, with integrated trace of quantum metric of 1.13, 3.25, and 5.27 (from energetically higher to lower bands) calculated directly from the DFT wave-functions. (See the expression of quantum metric in Sec. V C.) The full continuum model yields identical Chern numbers for the top three bands and similar values for the integrated trace of quantum metric—1.12, 3.20, and 5.25 (from energetically higher to lower bands). This implies that the top three bands of  $2.13^\circ$   $t\text{MoTe}_2$  resemble the zeroth, first, and second Landau levels, although the distribution of

Berry curvature and quantum metric is somewhat non-uniform, as shown in Fig. 5. Similar statements were also made in previous studies [47, 63, 71, 72].

In Tabs. IX to XI and XV to XVII, we list the parameter values for the full model with twist angle ranging from  $2.13^\circ$  to  $3.89^\circ$ . As we can see, the full model has a large number of parameters. For  $2.13^\circ$   $t\text{MoTe}_2$ , the model consists of 6 diagonal terms  $m$ , 72 interlayer coupling terms  $V$ , and 70 intralayer coupling terms  $w$ , resulting in 148 parameters. Similarly, for  $2.13^\circ$   $t\text{WSe}_2$ , the model includes 9 diagonal terms  $m$ , 45 interlayer coupling terms  $V$ , and 33 intralayer coupling terms  $w$ , leading to a total of 87 parameters. The large number of terms pose no difficulty in numerical calculations, where the form factors of interactions are always computed numerically, but can complicate possible analytical studies.

### C. Plane Wave Reduction

To support analytical investigations, we derive a “reduced model”. We will first impose a cutoff on the  $\mathbf{Q}$  lattice, and treat all  $\psi_{\mathbf{k},\mathbf{Q}}^\dagger$  with  $|\mathbf{Q}|$  larger than the cutoff as high-energy degrees of freedom. Then, we then integrate out the high-energy degrees of freedom in the DFT Hamiltonian  $h_{\text{DFT}}(\mathbf{k})$ , and obtain an effective DFT Hamiltonian  $h_{\text{DFT}}^{\text{reduced}}(\mathbf{k})$ . Finally, we can construct a reduced model from  $h_{\text{DFT}}^{\text{reduced}}(\mathbf{k})$  in the same way as constructing the full model from  $h_{\text{DFT}}(\mathbf{k})$ . The reduced model includes only a subset of  $\mathbf{Q}$  points, significant lowering the number of parameters: for instance, the reduced model contains 23 parameters for  $2.13^\circ$   $t\text{MoTe}_2$  and 15 parameters for  $2.13^\circ$   $t\text{WSe}_2$ . Nevertheless, the reduced

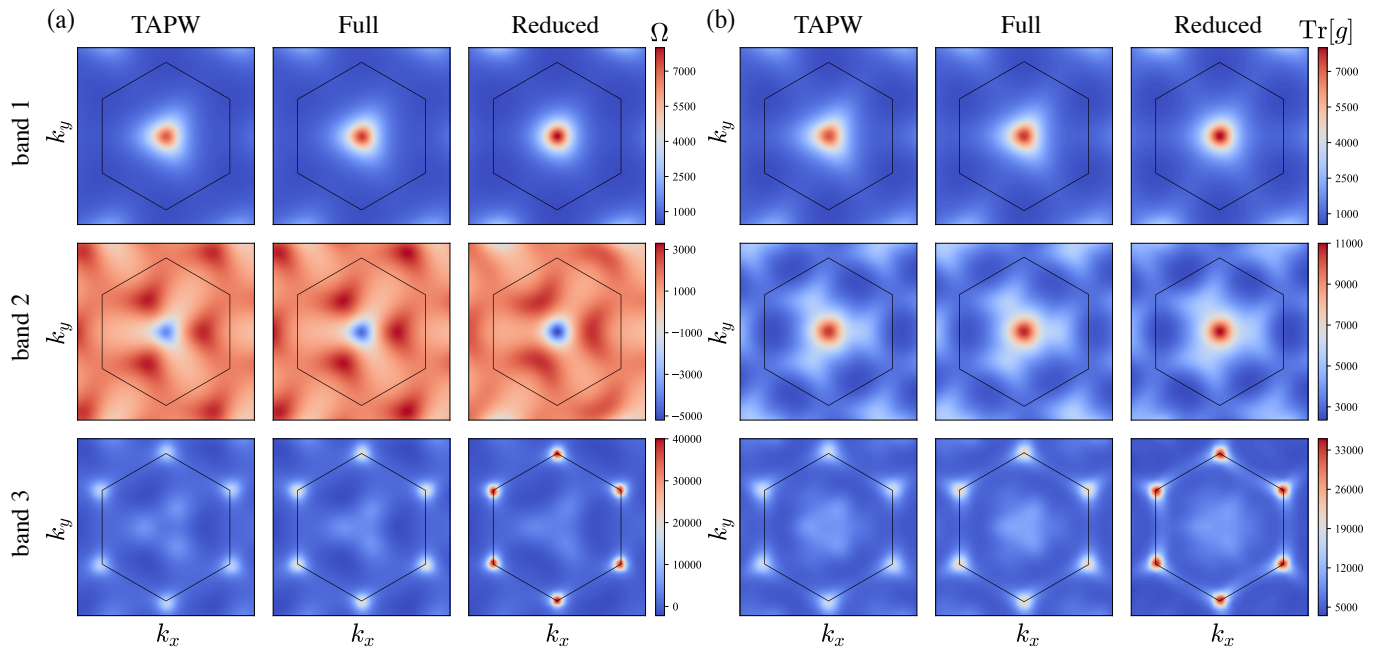


FIG. 5. **Distribution of Berry curvature and quantum metric of  $2.13^\circ$   $t\text{MoTe}_2$ .** (a):Berry curvature. (b):Trace of Quantum metric. Each row corresponds to different energy bands (band 1, band 2, and band 3), and each column compares different methods: TAPW, full model, and reduced model. The hexagonal boundary in each subplot represents the first moiré Brillouin zone.

model can still well capture the essential low-energy part, as shown in Fig. 4(b,d): the energy deviations under 1.2 meV and 1.8 meV for the top four bands for both  $t\text{MoTe}_2$  and  $t\text{WSe}_2$ , respectively, and minimum overlap probability for the reduced model remains above 95%.

The parameter values at different angles for the full and reduced models immediately shows a trend: we typically need more harmonics (*i.e.*, a larger number of different values of  $|\mathbf{p}|$  in Eq. (9)) in the moiré potential to capture the DFT results, as the angle decreases. Specifically, we find that for  $t\text{MoTe}_2$ , the number of intralayer (interlayer) harmonics increases from 4 (4) for  $3.89^\circ$  to 5 (6) for  $2.13^\circ$  for the full model, and increases from 1 (2) for  $3.89^\circ$  to 5 (4) for  $2.13^\circ$  for the reduced model. The trend is similar for  $t\text{WSe}_2$ : the number of intralayer (interlayer) harmonics increases from 2 (2) for  $3.89^\circ$  to 3 (3) for  $2.13^\circ$  for the full model, though the number of harmonics does not change for the reduced model. From the change of the number of harmonics (especially the unchanged number of harmonics of the reduced model of  $t\text{WSe}_2$ ), we can see a smaller angle dependence of  $t\text{WSe}_2$  than  $t\text{MoTe}_2$  in the same range of angles, of which the reason is left for future study.

#### IV. CONCLUSION

In this study, we present a universal framework for constructing continuum models of moiré materials without the necessity of parameter fitting. Our method accurately captures the essential electronic properties of moiré

systems, including a faithful reproduction of the wavefunction. Although we only use the method on  $t\text{MoTe}_2$  and  $t\text{WSe}_2$  in the current work, it is extendable to other moiré systems, such as multilayer graphene-hBN superlattices, which have been extensively studied both experimentally [21–25, 117] and theoretically [39, 59, 118–132].

## V. METHOD

### A. Parameter Relations

The parameters of the continuum Hamiltonian of  $t\text{MoTe}_2$  and  $t\text{WSe}_2$  in the common notation used in the literature can always be expressed in terms of  $r_{ll'}^{M_x M_y}$  in Eq. (8). For example, the second Harmonic Hamiltonian

in Ref. [46] of AA-stacked  $t\text{MoTe}_2$  in K valley reads

$$\begin{aligned}
h_{\mathbf{K},\mathbf{Q}\mathbf{Q}'}^{AA}(\mathbf{k}) &= \delta_{\mathbf{Q}\mathbf{Q}'} \left( \frac{-\hbar^2(\mathbf{k}-\mathbf{Q})^2}{2m^*} \right) \\
&+ V \sum_{i=1}^3 \left[ e^{-i\psi(-)\mathbf{Q}} \delta_{\mathbf{Q}+\mathbf{g}_i,\mathbf{Q}'} + e^{i\psi(-)\mathbf{Q}} \delta_{\mathbf{Q}-\mathbf{g}_i,\mathbf{Q}'} \right] \\
&+ V_2 \sum_{i=1}^3 [\delta_{\mathbf{Q}+\mathbf{g}_{2i},\mathbf{Q}'} + \delta_{\mathbf{Q},\mathbf{Q}'+\mathbf{g}_{2i}}] \\
&+ w \sum_{i=1}^3 [\delta_{\mathbf{Q}+\mathbf{q}_i,\mathbf{Q}'} + \delta_{\mathbf{Q},\mathbf{Q}'+\mathbf{q}_i}] \\
&+ w_2 \sum_{i=1}^3 [\delta_{\mathbf{Q}+\mathbf{q}_{2i},\mathbf{Q}'} + \delta_{\mathbf{Q},\mathbf{Q}'+\mathbf{q}_{2i}}] .
\end{aligned} \tag{10}$$

In the notation of Eq. (7), Eq. (10) just corresponds to  $m^{11} = m^*$ ,  $V_{\mathbf{l}\mathbf{Q},\mathbf{b}_{M1}}^{00} = V e^{-i\psi(-)\mathbf{Q}}$ ,  $V_{\mathbf{l},\mathbf{b}_{M1}+\mathbf{b}_{M2}}^{00} = V_2$ ,  $w_{ll'}^{00} = w$ ,  $w_{ll',\mathbf{b}_{M1}}^{00} = w_2$ , with all other parameters set to zero. Here  $r_{ll',\mathbf{G}_M}^{M_x M_y}|_{l=l',\mathbf{G}_M=0} = \hbar^2/(2m^{M_x M_y})$ ,  $r_{ll',\mathbf{G}_M}^{M_x M_y}|_{l=l',\mathbf{G}_M \neq 0} = V_{\mathbf{l},\mathbf{G}_M}^{M_x M_y}$ ,  $r_{ll',\mathbf{G}_M}^{M_x M_y}|_{l \neq l'} = w_{ll'}^{M_x M_y}$ .

## B. Orthonormalization and Projection

In this part, we outline the orthonormalization and projection process to determine the parameters  $r_{ll',\mathbf{G}_M}^{M_x M_y}$  in Eq. (8). We will focus on the case where the  $\mathbf{Q}$  lattice is infinite, since the procedure for the finite  $\mathbf{Q}$  lattice is very similar, as discussed in App. [C3]. We start by noting that the terms  $Y_{ll',\mathbf{p}}^{M_x M_y}(\mathbf{k})$  in Eq. (9) are linearly independent at a fixed  $\mathbf{k}$ , *i.e.*,  $\sum r_{ll',\mathbf{G}_M}^{M_x M_y} Y_{ll',\mathbf{p}}^{M_x M_y}(\mathbf{k}) = 0$  can only be satisfied when  $r_{ll',\mathbf{G}_M}^{M_x M_y} = 0$  for all  $(M_x, M_y, l, l', \mathbf{G}_M)$ , where  $\mathbf{p} = \mathbf{K}_l - \mathbf{K}_{l'} + \mathbf{G}_M$  and the sum is over all values of  $(M_x, M_y, l, l', \mathbf{G}_M)$ . (See proof in App. [C3].) It means that we could determine the values of  $r_{ll',\mathbf{G}_M}^{M_x M_y}$  at a single fixed  $\mathbf{k} = \mathbf{k}_0$  for all  $M_x, M_y \in \mathbb{N}$ , all moiré reciprocal lattice vectors  $\mathbf{G}_M$  and all  $l, l' = b, t$ . Specifically, we apply the Gram-Schmidt process to orthonormalize the  $Y_{ll',\mathbf{p}}^{M_x M_y}(\mathbf{k}_0)$  terms, *i.e.*, finding new  $\tilde{Y}_{ll',\mathbf{p}}^{M_x M_y}(\mathbf{k}_0)$  terms that are related to  $Y_{ll',\mathbf{p}}^{M_x M_y}(\mathbf{k}_0)$  by

$$\tilde{Y}_{ll',\mathbf{p}}^{M_x M_y}(\mathbf{k}_0) = \sum_{\tilde{M}_x \tilde{M}_y} Y_{\tilde{M}_x \tilde{M}_y}^{M_x M_y}(\mathbf{k}_0) z_{\tilde{M}_x \tilde{M}_y, M_x M_y}^{ll',\mathbf{p}} \tag{11}$$

such that

$$\text{Tr} \left\{ \left[ \tilde{Y}_{ll',\mathbf{p}}^{M_x M_y}(\mathbf{k}_0) \right]^\dagger \tilde{Y}_{ll',\mathbf{p}}^{M'_x M'_y}(\mathbf{k}_0) \right\} = \delta_{M_x, M'_x} \delta_{M_y, M'_y} . \tag{12}$$

In this process, we do not need to linearly combine different values of  $(l, l', \mathbf{G}_M)$ , since the terms  $Y_{ll',\mathbf{p}}^{M_x M_y}(\mathbf{k})$  (with

$\mathbf{p} = \mathbf{K}_l - \mathbf{K}_{l'} + \mathbf{G}_M$ ) are naturally orthogonal for different values of  $(l, l', \mathbf{G}_M)$ , as proved in App. [C3]. Then, we can obtain

$$\tilde{r}_{ll',\mathbf{G}_M}^{M_x M_y} = \text{Tr} \left\{ \left[ \tilde{Y}_{ll',\mathbf{p}}^{M_x M_y}(\mathbf{k}_0) \right]^\dagger h_{\text{DFT}}(\mathbf{k}_0) \right\} , \tag{13}$$

resulting in

$$r_{ll',\mathbf{G}_M}^{M_x M_y} = \sum_{\tilde{M}_x \tilde{M}_y} z_{\tilde{M}_x \tilde{M}_y, M_x M_y}^{ll',\mathbf{p}} \tilde{r}_{ll',\mathbf{G}_M}^{\tilde{M}_x \tilde{M}_y} , \tag{14}$$

where  $r_{ll',\mathbf{G}_M}^{M_x M_y}$  represent the original parameters in Eq. (8), and  $\tilde{r}_{ll',\mathbf{G}_M}^{M_x M_y}$  is defined in Eq. (13).

## C. Quantum Metric and Berry Curvature

To characterize the quantum geometric properties of the electronic bands in our continuum models, we calculate both the Berry curvature and the quantum metric.

The Berry curvature  $\Omega_n(\mathbf{k})$  for the  $n$ -th band is expressed in terms of the projection operator  $P_n(\mathbf{k}) = |u_n(\mathbf{k})\rangle\langle u_n(\mathbf{k})|$  as follows:

$$\Omega_n(\mathbf{k}) = i \text{Tr} \left[ P_n(\mathbf{k}) \partial_{k_x} P_n(\mathbf{k}) \partial_{k_y} P_n(\mathbf{k}) \right] - (x \leftrightarrow y), \tag{15}$$

where  $|u_n(\mathbf{k})\rangle$  is the periodic part of the Bloch state of the  $n$ th band.

Similarly, the quantum metric tensor  $g_{n,ij}(\mathbf{k})$  is defined as:

$$g_{n,ij}(\mathbf{k}) = \frac{1}{2} \text{Tr} \left[ \partial_{k_i} P_n(\mathbf{k}) \partial_{k_j} P_n(\mathbf{k}) \right], \tag{16}$$

where  $i, j = x, y$ . We show the distribution of  $\Omega_n(\mathbf{k})$  and trace of quantum metric  $\text{Tr}[g_n(\mathbf{k})]$  in Fig. 5, and we are also interested in the integration of  $\text{Tr}[g_n(\mathbf{k})]$  in the first moiré Brillouin zone:

$$\chi = \frac{1}{2\pi} \int_{\text{BZ}} d\mathbf{k} \text{Tr}[g_n(\mathbf{k})] . \tag{17}$$

## VI. ACKNOWLEDGMENTS

The authors thank Di Xiao and Oskar Vafek for helpful discussions. This work was supported by the Ministry of Science and Technology of China (Grant No. 2023YFA1607400, 2022YFA1403800), the National Natural Science Foundation of China (Grant No.12274436) and the Science Center of the National Natural Science Foundation of China (Grant No. 12188101) and . H.W. acknowledge support from the Informatization Plan of the Chinese Academy of Sciences (CASWX2021SF-0102). B. A. B.'s work was primarily supported by the DOE Grant No. DE-SC0016239 and the Simons Investigator Grant No. 404513. N.R. also acknowledges support from the QuantERA II Programme that



has received funding from the European Union's Horizon 2020 research and innovation programme under Grant Agreement No 101017733 and from the European Research Council (ERC) under the European Union's Horizon 2020 Research and Innovation Programme (Grant Agreement No. 101020833). The Flatiron Institute is a division of the Simons Foundation. X. Dai is supported by a fellowship award and a CRF award from the Research Grants Council of the Hong Kong Special Administrative Region, China (Project No. SRFS2324-6S01 and No. C7037-22GF). J. Y.'s work at Princeton University is supported by the Gordon and Betty Moore Foundation through Grant No. GBMF8685 towards the Princeton theory program. J. Y.'s work at University of Florida is supported by startup funds at University of Florida.

- [1] Y. Cao, V. Fatemi, S. Fang, K. Watanabe, T. Taniguchi, E. Kaxiras, and P. Jarillo-Herrero, Unconventional superconductivity in magic-angle graphene superlattices, *Nature* **556**, 43 (2018).
- [2] M. Yankowitz, S. Chen, H. Polshyn, Y. Zhang, K. Watanabe, T. Taniguchi, D. Graf, A. F. Young, and C. R. Dean, Tuning superconductivity in twisted bilayer graphene, *Science* **363**, 1059 (2019).
- [3] E. Codecido, Q. Wang, R. Koester, S. Che, H. Tian, R. Lv, S. Tran, K. Watanabe, T. Taniguchi, F. Zhang, M. Bockrath, and C. N. Lau, Correlated insulating and superconducting states in twisted bilayer graphene below the magic angle, *Science Advances* **5**, eaaw9770 (2019).
- [4] X. Lu, P. Stepanov, W. Yang, M. Xie, M. A. Aamir, I. Das, C. Urgell, K. Watanabe, T. Taniguchi, G. Zhang, A. Bachtold, A. H. MacDonald, and D. K. Efetov, Superconductors, orbital magnets and correlated states in magic-angle bilayer graphene, *Nature* **574**, 653 (2019).
- [5] H. S. Arora, R. Polski, Y. Zhang, A. Thomson, Y. Choi, H. Kim, Z. Lin, I. Z. Wilson, X. Xu, J.-H. Chu, K. Watanabe, T. Taniguchi, J. Alicea, and S. Nadj-Perge, Superconductivity in metallic twisted bilayer graphene stabilized by WSe<sub>2</sub>, *Nature* **583**, 379 (2020).
- [6] P. Stepanov, I. Das, X. Lu, A. Fahimniya, K. Watanabe, T. Taniguchi, F. H. L. Koppens, J. Lischner, L. Levitov, and D. K. Efetov, Untying the insulating and superconducting orders in magic-angle graphene, *Nature* **583**, 375 (2020).
- [7] Y. Saito, J. Ge, K. Watanabe, T. Taniguchi, and A. F. Young, Independent superconductors and correlated insulators in twisted bilayer graphene, *Nature Physics* **16**, 926 (2020).
- [8] M. Oh, K. P. Nuckolls, D. Wong, R. L. Lee, X. Liu, K. Watanabe, T. Taniguchi, and A. Yazdani, Evidence for unconventional superconductivity in twisted bilayer graphene, *Nature* **600**, 240 (2021).
- [9] L. Balents, C. R. Dean, D. K. Efetov, and A. F. Young, Superconductivity and strong correlations in moiré flat bands, *Nature Physics* **16**, 725 (2020).
- [10] E. Y. Andrei, D. K. Efetov, P. Jarillo-Herrero, A. H. MacDonald, K. F. Mak, T. Senthil, E. Tutuc, A. Yazdani, and A. F. Young, The marvels of moiré materials, *Nature Reviews Materials* **6**, 201 (2021).
- [11] N. Regnault, Y. Xu, M.-R. Li, D.-S. Ma, M. Jovanovic, A. Yazdani, S. S. P. Parkin, C. Felser, L. M. Schoop, N. P. Ong, R. J. Cava, L. Elcoro, Z.-D. Song, and B. A. Bernevig, Catalogue of flat-band stoichiometric materials, *Nature* **603**, 824 (2022).
- [12] J. G. Checkelsky, B. A. Bernevig, P. Coleman, Q. Si, and S. Paschen, Flat bands, strange metals and the kondo effect, *Nature Reviews Materials* **9**, 509 (2024).
- [13] J. Cai, E. Anderson, C. Wang, X. Zhang, X. Liu, W. Holtzmann, Y. Zhang, F. Fan, T. Taniguchi, K. Watanabe, Y. Ran, T. Cao, L. Fu, D. Xiao, W. Yao, and X. Xu, Signatures of fractional quantum anomalous hall states in twisted MoTe<sub>2</sub>, *Nature* **622**, 63 (2023).
- [14] Y. Zeng, Z. Xia, K. Kang, J. Zhu, P. Knüppel, C. Vaswani, K. Watanabe, T. Taniguchi, K. F. Mak, and J. Shan, Thermodynamic evidence of fractional chern insulator in moiré MoTe<sub>2</sub>, *Nature* **622**, 69 (2023).
- [15] H. Park, J. Cai, E. Anderson, Y. Zhang, J. Zhu, X. Liu, C. Wang, W. Holtzmann, C. Hu, Z. Liu, T. Taniguchi, K. Watanabe, J.-H. Chu, T. Cao, L. Fu, W. Yao, C.-Z. Chang, D. Cobden, D. Xiao, and X. Xu, Observation of fractionally quantized anomalous hall effect, *Nature* **622**, 74 (2023).
- [16] F. Xu, Z. Sun, T. Jia, C. Liu, C. Xu, C. Li, Y. Gu, K. Watanabe, T. Taniguchi, B. Tong, J. Jia, Z. Shi, S. Jiang, Y. Zhang, X. Liu, and T. Li, Observation of integer and fractional quantum anomalous hall effects in twisted bilayer MoTe<sub>2</sub>, *Physical Review X* **13**, 031037 (2023).
- [17] K. Kang, B. Shen, Y. Qiu, Y. Zeng, Z. Xia, K. Watanabe, T. Taniguchi, J. Shan, and K. F. Mak, Evidence of the fractional quantum spin hall effect in moiré MoTe<sub>2</sub>, *Nature* **628**, 522 (2024).
- [18] Z. Ji, H. Park, M. E. Barber, C. Hu, K. Watanabe, T. Taniguchi, J.-H. Chu, X. Xu, and Z.-x. Shen, Local probe of bulk and edge states in a fractional chern insulator (2024), arXiv:2404.07157 [cond-mat].
- [19] E. Redekop, C. Zhang, H. Park, J. Cai, E. Anderson, O. Sheekey, T. Arp, G. Babikyan, S. Salters, K. Watanabe, T. Taniguchi, X. Xu, and A. F. Young, Direct magnetic imaging of fractional chern insulators in twisted MoTe<sub>2</sub> with a superconducting sensor (2024), arXiv:2405.10269 [cond-mat].
- [20] F. Xu, X. Chang, J. Xiao, Y. Zhang, F. Liu, Z. Sun, N. Mao, N. Peshcherenko, J. Li, K. Watanabe, T. Taniguchi, B. Tong, L. Lu, J. Jia, D. Qian, Z. Shi, Y. Zhang, X. Liu, S. Jiang, and T. Li, Interplay between topology and correlations in the second moiré band of twisted bilayer MoTe<sub>2</sub> (2024), arXiv:2406.09687 [cond-mat].
- [21] Z. Lu, T. Han, Y. Yao, A. P. Reddy, J. Yang, J. Seo, K. Watanabe, T. Taniguchi, L. Fu, and L. Ju, Fractional quantum anomalous hall effect in multilayer graphene, *Nature* **626**, 759 (2024).
- [22] J. Xie, Z. Huo, X. Lu, Z. Feng, Z. Zhang, W. Wang, Q. Yang, K. Watanabe, T. Taniguchi, K. Liu, Z. Song, X. C. Xie, J. Liu, and X. Lu, Even and odd-denominator fractional quantum anomalous hall effect in graphene moiré superlattices (2024), arXiv:2405.16944 [cond-mat].
- [23] H. Park, J. Cai, E. Anderson, X.-W. Zhang, X. Liu, W. Holtzmann, W. Li, C. Wang, C. Hu, Y. Zhao, T. Taniguchi, K. Watanabe, J. Yang, D. Cobden, J.-H. Chu, N. Regnault, B. A. Bernevig, L. Fu, T. Cao, D. Xiao, and X. Xu, Ferromagnetism and topology of the higher flat band in a fractional chern insulator (2024), arXiv:2406.09591 [cond-mat].
- [24] Y. Choi, Y. Choi, M. Valentini, C. L. Patterson, L. F. W. Holleis, O. I. Sheekey, H. Stoyanov, X. Cheng, T. Taniguchi, K. Watanabe, and A. F. Young, Electric field control of superconductivity and quantized anomalous hall effects in rhombohedral tetralayer graphene (2024), arXiv:2408.12584 [cond-mat].
- [25] Z. Lu, T. Han, Y. Yao, J. Yang, J. Seo, L. Shi, S. Ye, K. Watanabe, T. Taniguchi, and L. Ju, Extended quantum anomalous hall states in graphene/hBN moiré superlattices (2024), arXiv:2408.10203.

- [26] E. M. Spanton, A. A. Zibrov, H. Zhou, T. Taniguchi, K. Watanabe, M. P. Zaletel, and A. F. Young, Observation of fractional chern insulators in a van der waals heterostructure, *Science* **360**, 62 (2018).
- [27] Y. Xie, A. T. Pierce, J. M. Park, D. E. Parker, E. Khalaf, P. Ledwith, Y. Cao, S. H. Lee, S. Chen, P. R. Forrester, K. Watanabe, T. Taniguchi, A. Vishwanath, P. Jarillo-Herrero, and A. Yacoby, Fractional chern insulators in magic-angle twisted bilayer graphene, *Nature* **600**, 439 (2021).
- [28] J. M. B. Lopes dos Santos, N. M. R. Peres, and A. H. Castro Neto, Graphene bilayer with a twist: Electronic structure, *Physical Review Letters* **99**, 256802 (2007).
- [29] R. Bistritzer and A. H. MacDonald, Moiré bands in twisted double-layer graphene, *Proceedings of the National Academy of Sciences* **108**, 12233 (2011).
- [30] J. M. B. Lopes dos Santos, N. M. R. Peres, and A. H. Castro Neto, Continuum model of the twisted graphene bilayer, *Physical Review B* **86**, 155449 (2012).
- [31] J. M. Luttinger and W. Kohn, Motion of electrons and holes in perturbed periodic fields, *Physical Review* **97**, 869 (1955).
- [32] E. O. Kane, Chapter 3 the  $k \cdot p$  method, in *Semiconductors and Semimetals*, Semiconductors and Semimetals, Vol. 1, edited by R. K. Willardson and A. C. Beer (Elsevier, 1966) pp. 75–100.
- [33] C.-X. Liu, X.-L. Qi, H. Zhang, X. Dai, Z. Fang, and S.-C. Zhang, Model hamiltonian for topological insulators, *Physical Review B* **82**, 045122 (2010).
- [34] J. Jung, A. Raoux, Z. Qiao, and A. H. MacDonald, Ab initio theory of moiré superlattice bands in layered two-dimensional materials, *Physical Review B* **89**, 205414 (2014).
- [35] P. Moon and M. Koshino, Electronic properties of graphene/hexagonal-boron-nitride moiré superlattice, *Physical Review B* **90**, 155406 (2014).
- [36] B. L. Chittari, G. Chen, Y. Zhang, F. Wang, and J. Jung, Gate-tunable topological flat bands in trilayer graphene boron-nitride moiré superlattices, *Physical Review Letters* **122**, 016401 (2019).
- [37] Z. Song, Z. Wang, W. Shi, G. Li, C. Fang, and B. A. Bernevig, All magic angles in twisted bilayer graphene are topological, *Physical Review Letters* **123**, 036401 (2019).
- [38] S. Carr, S. Fang, Z. Zhu, and E. Kaxiras, Exact continuum model for low-energy electronic states of twisted bilayer graphene, *Physical Review Research* **1**, 013001 (2019).
- [39] J. Herzog-Arbeitman, Y. Wang, J. Liu, P. M. Tam, Z. Qi, Y. Jia, D. K. Efetov, O. Vafek, N. Regnault, H. Weng, Q. Wu, B. A. Bernevig, and J. Yu, Moiré fractional chern insulators. ii. first-principles calculations and continuum models of rhombohedral graphene superlattices, *Physical Review B* **109**, 205122 (2024).
- [40] F. Wu, T. Lovorn, E. Tutuc, I. Martin, and A. MacDonald, Topological Insulators in Twisted Transition Metal Dichalcogenide Homobilayers, *Physical Review Letters* **122**, 086402 (2019).
- [41] M. Koshino and N. N. T. Nam, Effective continuum model for relaxed twisted bilayer graphene and moiré electron-phonon interaction, *Physical Review B* **101**, 195425 (2020).
- [42] M. Angeli and A. H. MacDonald,  $\Gamma$  valley transition metal dichalcogenide moiré bands, *Proceedings of the National Academy of Sciences* **118**, e2021826118 (2021).
- [43] A. P. Reddy, F. Alsallom, Y. Zhang, T. Devakul, and L. Fu, Fractional quantum anomalous Hall states in twisted bilayer  $\text{MoTe}_2$  and  $\text{WSe}_2$ , *Physical Review B* **108**, 085117 (2023).
- [44] C. Wang, X.-W. Zhang, X. Liu, Y. He, X. Xu, Y. Ran, T. Cao, and D. Xiao, Fractional Chern Insulator in Twisted Bilayer  $\text{MoTe}_2$ , *Physical Review Letters* **132**, 036501 (2024).
- [45] C. Xu, J. Li, Y. Xu, Z. Bi, and Y. Zhang, Maximally localized Wannier functions, interaction models, and fractional quantum anomalous Hall effect in twisted bilayer  $\text{MoTe}_2$ , *Proceedings of the National Academy of Sciences* **121**, e2316749121 (2024).
- [46] Y. Jia, J. Yu, J. Liu, J. Herzog-Arbeitman, Z. Qi, H. Pi, N. Regnault, H. Weng, B. A. Bernevig, and Q. Wu, Moiré fractional chern insulators. I. First-principles calculations and continuum models of twisted bilayer  $\text{MoTe}_2$ , *Physical Review B* **109**, 205121 (2024).
- [47] C. Xu, N. Mao, T. Zeng, and Y. Zhang, Multiple chern bands in twisted  $\text{MoTe}_2$  and possible non-abelian states (2024), arXiv:2403.17003 [cond-mat].
- [48] T. Devakul, V. Crépel, Y. Zhang, and L. Fu, Magic in twisted transition metal dichalcogenide bilayers, *Nature Communications* **12**, 6730 (2021).
- [49] N. N. T. Nam and M. Koshino, Lattice relaxation and energy band modulation in twisted bilayer graphene, *Physical Review B* **96**, 075311 (2017).
- [50] M. Koshino, N. F. Q. Yuan, T. Koretsune, M. Ochi, K. Kuroki, and L. Fu, Maximally localized wannier orbitals and the extended hubbard model for twisted bilayer graphene, *Physical Review X* **8**, 031087 (2018).
- [51] L. Balents, General continuum model for twisted bilayer graphene and arbitrary smooth deformations, *SciPost Physics* **7**, 10.21468/scipostphys.7.4.048 (2019).
- [52] F. Guinea and N. R. Walet, Continuum models for twisted bilayer graphene: Effect of lattice deformation and hopping parameters, *Physical Review B* **99**, 205134 (2019).
- [53] B. A. Bernevig, Z.-D. Song, N. Regnault, and B. Lian, Twisted bilayer graphene. i. matrix elements, approximations, perturbation theory, and a  $k \cdot p$  two-band model, *Physical Review B* **103**, 205411 (2021).
- [54] O. Vafek and J. Kang, Continuum effective hamiltonian for graphene bilayers for an arbitrary smooth lattice deformation from microscopic theories, *Physical Review B* **107**, 075123 (2023).
- [55] J. Kang and O. Vafek, Pseudomagnetic fields, particle-hole asymmetry, and microscopic effective continuum hamiltonians of twisted bilayer graphene, *Physical Review B* **107**, 075408 (2023).
- [56] B. Xie and J. Liu, Lattice distortions, moiré phonons, and relaxed electronic band structures in magic-angle twisted bilayer graphene, *Phys. Rev. B* **108**, 094115 (2023).
- [57] P. Moon and M. Koshino, Energy spectrum and quantum hall effect in twisted bilayer graphene, *Physical Review B* **85**, 195458 (2012).
- [58] S. Fang and E. Kaxiras, Electronic structure theory of weakly interacting bilayers, *Physical Review B* **93**, 235153 (2016).
- [59] Y. Park, Y. Kim, B. L. Chittari, and J. Jung, Topological flat bands in rhombohedral tetralayer and multilayer graphene on hexagonal boron nitride moiré su-

- perlattices, *Physical Review B* **108**, 155406 (2023).
- [60] T. Wang, M. Wang, W. Kim, S. G. Louie, L. Fu, and M. P. Zaletel, *Topology, magnetism and charge order in twisted MoTe<sub>2</sub> at higher integer hole fillings* (2023).
- [61] H. Goldman, A. P. Reddy, N. Paul, and L. Fu, Zero-field composite fermi liquid in twisted semiconductor bilayers, *Physical Review Letters* **131**, 136501 (2023).
- [62] A. Abouelkomsan, A. P. Reddy, L. Fu, and E. J. Bergholtz, Band mixing in the quantum anomalous Hall regime of twisted semiconductor bilayers, *Physical Review B* **109**, L121107 (2024).
- [63] C. Wang, X.-W. Zhang, X. Liu, J. Wang, T. Cao, and D. Xiao, *Higher landau-level analogues and signatures of non-abelian states in twisted bilayer MoTe<sub>2</sub>* (2024), [arXiv:2404.05697 \[cond-mat\]](https://arxiv.org/abs/2404.05697).
- [64] X.-W. Zhang, C. Wang, X. Liu, Y. Fan, T. Cao, and D. Xiao, Polarization-driven band topology evolution in twisted MoTe<sub>2</sub> and WSe<sub>2</sub>, *Nature Communications* **15**, 4223 (2024).
- [65] V. Crépel, N. Regnault, and R. Queiroz, Chiral limit and origin of topological flat bands in twisted transition metal dichalcogenide homobilayers, *Communications Physics* **7**, 1 (2024).
- [66] W.-X. Qiu, B. Li, X.-J. Luo, and F. Wu, Interaction-Driven Topological Phase Diagram of Twisted Bilayer MoTe<sub>2</sub>, *Physical Review X* **13**, 041026 (2023).
- [67] J. Dong, J. Wang, P. J. Ledwith, A. Vishwanath, and D. E. Parker, Composite Fermi Liquid at Zero Magnetic Field in Twisted MoTe<sub>2</sub>, *Physical Review Letters* **131**, 136502 (2023).
- [68] A. P. Reddy and L. Fu, Toward a global phase diagram of the fractional quantum anomalous Hall effect, *Physical Review B* **108**, 245159 (2023).
- [69] J. Yu, J. Herzog-Arbeitman, M. Wang, O. Vafek, B. A. Bernevig, and N. Regnault, Fractional Chern insulators versus nonmagnetic states in twisted bilayer MoTe<sub>2</sub>, *Physical Review B* **109**, 045147 (2024).
- [70] Y. H. Kwan, G. Wagner, J. Yu, A. K. Dagnino, Y. Jiang, X. Xu, B. A. Bernevig, T. Neupert, and N. Regnault, *When could abelian fractional topological insulators exist in twisted MoTe<sub>2</sub> (and other systems)* (2024), [arXiv:2407.02560 \[cond-mat\]](https://arxiv.org/abs/2407.02560).
- [71] A. P. Reddy, N. Paul, A. Abouelkomsan, and L. Fu, Non-abelian fractionalization in topological minibands, *Physical Review Letters* **133**, 166503 (2024).
- [72] C.-E. Ahn, W. Lee, K. Yananose, Y. Kim, and G. Y. Cho, Non-abelian fractional quantum anomalous hall states and first landau level physics of the second moiré band of twisted bilayer MoTe<sub>2</sub>, *Physical Review B* **110**, L161109 (2024).
- [73] T. Wang, T. Devakul, M. P. Zaletel, and L. Fu, *Diverse magnetic orders and quantum anomalous hall effect in twisted bilayer MoTe<sub>2</sub> and WSe<sub>2</sub>* (2024), [arXiv:2306.02501](https://arxiv.org/abs/2306.02501).
- [74] H. Pan, F. Wu, and S. Das Sarma, Band topology, Hubbard model, Heisenberg model, and Dzyaloshinskii-Moriya interaction in twisted bilayer WSe<sub>2</sub>, *Physical Review Research* **2**, 033087 (2020).
- [75] L. Wang, E.-M. Shih, A. Ghiotto, L. Xian, D. A. Rhodes, C. Tan, M. Claassen, D. M. Kennes, Y. Bai, B. Kim, K. Watanabe, T. Taniguchi, X. Zhu, J. Hone, A. Rubio, A. N. Pasupathy, and C. R. Dean, Correlated electronic phases in twisted bilayer transition metal dichalcogenides, *Nature Materials* **19**, 861 (2020).
- [76] V. Crépel and L. Fu, Anomalous hall metal and fractional chern insulator in twisted transition metal dichalcogenides, *Physical Review B* **107**, L201109 (2023).
- [77] Y. Guo, J. Pack, J. Swann, L. Holtzman, M. Cothrine, K. Watanabe, T. Taniguchi, D. Mandrus, K. Barkmak, J. Hone, A. J. Millis, A. N. Pasupathy, and C. R. Dean, *Superconductivity in twisted bilayer WSe<sub>2</sub>* (2024), [arXiv:2406.03418](https://arxiv.org/abs/2406.03418).
- [78] Y. Xia, Z. Han, K. Watanabe, T. Taniguchi, J. Shan, and K. F. Mak, Superconductivity in twisted bilayer WSe<sub>2</sub>, *Nature*, 1 (2024).
- [79] S. Kim, J. F. Mendez-Valderrama, X. Wang, and D. Chowdhury, *Theory of correlated insulator(s) and superconductor at  $\nu = 1$  in twisted WSe<sub>2</sub>* (2024), [arXiv:2406.03525](https://arxiv.org/abs/2406.03525).
- [80] B. A. Foutty, C. R. Kometter, T. Devakul, A. P. Reddy, K. Watanabe, T. Taniguchi, L. Fu, and B. E. Feldman, Mapping twist-tuned multiband topology in bilayer WSe<sub>2</sub>, *Science* **384**, 343 (2024).
- [81] C. Schrade and L. Fu, Nematic, chiral, and topological superconductivity in twisted transition metal dichalcogenides, *Physical Review B* **110**, 035143 (2024).
- [82] C. Tuo, M.-R. Li, Z. Wu, W. Sun, and H. Yao, *Theory of topological superconductivity and antiferromagnetic correlated insulators in twisted bilayer WSe<sub>2</sub>* (2024), [arXiv:2409.06779](https://arxiv.org/abs/2409.06779).
- [83] M. Bélanger, J. Fournier, and D. Sénéchal, Superconductivity in the twisted bilayer transition metal dichalcogenide WSe<sub>2</sub>: A quantum cluster study, *Physical Review B* **106**, 235135 (2022).
- [84] L. Klebl, A. Fischer, L. Classen, M. M. Scherer, and D. M. Kennes, Competition of density waves and superconductivity in twisted tungsten diselenide, *Physical Review Research* **5**, L012034 (2023).
- [85] A. Wietek, J. Wang, J. Zang, J. Cano, A. Georges, and A. Millis, Tunable stripe order and weak superconductivity in the moiré hubbard model, *Physical Review Research* **4**, 043048 (2022).
- [86] Y.-M. Wu, Z. Wu, and H. Yao, Pair-density-wave and chiral superconductivity in twisted bilayer transition metal dichalcogenides, *Physical Review Letters* **130**, 126001 (2023).
- [87] M. Zegrodnik and A. Biborski, Mixed singlet-triplet superconducting state within the moiré  $t-J-U$  model applied to twisted bilayer WSe<sub>2</sub>, *Physical Review B* **108**, 064506 (2023).
- [88] W. Akbar, A. Biborski, L. Rademaker, and M. Zegrodnik, *Topological superconductivity with mixed singlet-triplet pairing in moiré transition-metal-dichalcogenide bilayers* (2024), [arXiv:2403.05903](https://arxiv.org/abs/2403.05903).
- [89] M. Christos, P. M. Bonetti, and M. S. Scheurer, *Approximate symmetries, insulators, and superconductivity in continuum-model description of twisted WSe<sub>2</sub>* (2024), [arXiv:2407.02393](https://arxiv.org/abs/2407.02393).
- [90] J. Zhu, Y.-Z. Chou, M. Xie, and S. D. Sarma, *Theory of superconductivity in twisted transition metal dichalcogenide homobilayers* (2024), [arXiv:2406.19348](https://arxiv.org/abs/2406.19348).
- [91] N. Myerson-Jain and C. Xu, *Superconductor-insulator transition in the tmd moiré systems and the deconfined quantum critical point* (2024), [arXiv:2406.12971](https://arxiv.org/abs/2406.12971).
- [92] F. Xie, L. Chen, S. Sur, Y. Fang, J. Cano, and Q. Si, *Superconductivity in twisted WSe<sub>2</sub> from topology-induced quantum fluctuations* (2024), [arXiv:2408.10185](https://arxiv.org/abs/2408.10185).

- [93] D. Guerci, D. Kaplan, J. Ingham, J. H. Pixley, and A. J. Millis, **Topological superconductivity from repulsive interactions in twisted WSe<sub>2</sub>** (2024), [arXiv:2408.16075](https://arxiv.org/abs/2408.16075).
- [94] Y. Zhang, Continuum model for twist tmds, <https://github.com/zhangyan31415/continuum-model-twist-tmds> (2024).
- [95] N. Mao, C. Xu, J. Li, T. Bao, P. Liu, Y. Xu, C. Felser, L. Fu, and Y. Zhang, Transfer learning relaxation, electronic structure and continuum model for twisted bilayer MoTe<sub>2</sub>, **Communications Physics** **7**, 1 (2024).
- [96] G. Kresse and J. Hafner, Ab initio molecular dynamics for liquid metals, **Physical Review B** **47**, 558 (1993).
- [97] G. Kresse and J. Hafner, Norm-conserving and ultrasoft pseudopotentials for first-row and transition elements, **Journal of Physics: Condensed Matter** **6**, 8245 (1994).
- [98] P. E. Blöchl, Projector augmented-wave method, **Physical Review B** **50**, 17953 (1994).
- [99] G. Kresse and J. Furthmüller, Efficient iterative schemes for ab initio total-energy calculations using a plane-wave basis set, **Physical Review B** **54**, 11169 (1996).
- [100] G. Kresse and D. Joubert, From ultrasoft pseudopotentials to the projector augmented-wave method, **Physical Review B** **59**, 1758 (1999).
- [101] R. Jinnouchi, F. Karsai, and G. Kresse, On-the-fly machine learning force field generation: Application to melting points, **Physical Review B** **100**, 014105 (2019).
- [102] A. Musaelian, S. Batzner, A. Johansson, L. Sun, C. J. Owen, M. Kornbluth, and B. Kozinsky, Learning local equivariant representations for large-scale atomistic dynamics, **Nature Communications** **14**, 579 (2023).
- [103] T. Ozaki, Variationally optimized atomic orbitals for large-scale electronic structures, **Physical Review B** **67**, 155108 (2003).
- [104] T. Ozaki and H. Kino, Numerical atomic basis orbitals from H to Kr, **Physical Review B** **69**, 195113 (2004).
- [105] T. Ozaki and H. Kino, Efficient projector expansion for the ab initio lcao method, **Physical Review B** **72**, 045121 (2005).
- [106] J. M. Soler, E. Artacho, J. D. Gale, A. García, J. Junquera, P. Ordejón, and D. Sánchez-Portal, The siesta method for ab initio order-n materials simulation, **Journal of Physics: Condensed Matter** **14**, 2745 (2002).
- [107] P. Li, X. Liu, M. Chen, P. Lin, X. Ren, L. Lin, C. Yang, and L. He, Large-scale *ab initio* simulations based on systematically improvable atomic basis, **Computational Materials Science Computational Materials Science in China**, **112**, 503 (2016).
- [108] M. Chen, G.-C. Guo, and L. He, Systematically improvable optimized atomic basis sets for ab initio calculations, **Journal of Physics: Condensed Matter** **22**, 445501 (2010).
- [109] W. Miao, C. Li, X. Han, D. Pan, and X. Dai, Truncated atomic plane wave method for subband structure calculations of moiré systems, **Physical Review B** **107**, 125112 (2023).
- [110] C. Chen, K. P. Nuckolls, S. Ding, W. Miao, D. Wong, M. Oh, R. L. Lee, S. He, C. Peng, D. Pei, Y. Li, S. Zhang, J. Liu, Z. Liu, C. Jozwiak, A. Bostwick, E. Rotenberg, C. Li, X. Han, D. Pan, X. Dai, C. Liu, B. A. Bernevig, Y. Wang, A. Yazdani, and Y. Chen, Strong inter-valley electron-phonon coupling in magic-angle twisted bilayer graphene, [arXiv.org](https://arxiv.org/abs/2303.14903) (2023), [2303.14903](https://arxiv.org/abs/2303.14903) [cond-mat.mes-hall].
- [111] H. Shi, W. Miao, and X. Dai, Moiré optical phonons dancing with heavy electrons in magic-angle twisted bilayer graphene, [arXiv.org](https://arxiv.org/abs/2402.11824) (2024), [2402.11824](https://arxiv.org/abs/2402.11824) [cond-mat.mes-hall].
- [112] P.-O. Löwdin, A note on the quantum-mechanical perturbation theory, **The Journal of Chemical Physics** **19**, 1396 (1951).
- [113] T. Cao, G. Wang, W. Han, H. Ye, C. Zhu, J. Shi, Q. Niu, P. Tan, E. Wang, B. Liu, and J. Feng, Valley-selective circular dichroism of monolayer molybdenum disulphide, **Nature Communications** **3**, 887 (2012).
- [114] D. Xiao, G.-B. Liu, W. Feng, X. Xu, and W. Yao, Coupled Spin and Valley Physics in Monolayers of MoS<sub>2</sub> and Other Group-VI Dichalcogenides, **Physical Review Letters** **108**, 196802 (2012).
- [115] Y. Zhang, T. Liu, and L. Fu, Electronic structures, charge transfer, and charge order in twisted transition metal dichalcogenide bilayers, **Physical Review B** **103**, 155142 (2021).
- [116] T. Wang, T. Devakul, M. P. Zaletel, and L. Fu, **Topological magnets and magnons in twisted bilayer MoTe<sub>2</sub> and WSe<sub>2</sub>** (2023), [arXiv:2306.02501](https://arxiv.org/abs/2306.02501) [cond-mat].
- [117] Y.-Y. Zhou, Y. Zhang, S. Zhang, H. Cai, L.-H. Tong, Y. Tian, T. Chen, Q. Tian, C. Zhang, Y. Wang, X. Zou, X. Liu, Y. Hu, L. Zhang, L. Zhang, W.-X. Wang, L. Liao, Z. Qin, and L.-J. Yin, **Layer-dependent evolution of electronic structures and correlations in rhombohedral multilayer graphene** (2023), [arXiv:2312.13637](https://arxiv.org/abs/2312.13637).
- [118] Y. H. Kwan, J. Yu, J. Herzog-Arbeitman, D. K. Efetov, N. Regnault, and B. A. Bernevig, **Moiré fractional chern insulators iii: Hartree-fock phase diagram, magic angle regime for chern insulator states, the role of the moiré potential and goldstone gaps in rhombohedral graphene superlattices** (2023), [arXiv:2312.11617](https://arxiv.org/abs/2312.11617).
- [119] J. Yu, J. Herzog-Arbeitman, Y. H. Kwan, N. Regnault, and B. A. Bernevig, **Moiré fractional chern insulators iv: Fluctuation-driven collapse of fcis in multi-band exact diagonalization calculations on rhombohedral graphene** (2024), [arXiv:2407.13770](https://arxiv.org/abs/2407.13770).
- [120] Z. Guo, X. Lu, B. Xie, and J. Liu, Fractional chern insulator states in multilayer graphene moiré superlattices, **Physical Review B** **110**, 075109 (2024).
- [121] B. Zhou, H. Yang, and Y.-H. Zhang, **Fractional quantum anomalous hall effects in rhombohedral multilayer graphene in the moiréless limit and in coulomb imprinted superlattice** (2024), [arXiv:2311.04217](https://arxiv.org/abs/2311.04217).
- [122] J. Dong, T. Wang, T. Wang, T. Soejima, M. P. Zaletel, A. Vishwanath, and D. E. Parker, **Anomalous hall crystals in rhombohedral multilayer graphene i: Interaction-driven chern bands and fractional quantum hall states at zero magnetic field** (2024), [arXiv:2311.05568](https://arxiv.org/abs/2311.05568).
- [123] T. Soejima, J. Dong, T. Wang, T. Wang, M. P. Zaletel, A. Vishwanath, and D. E. Parker, **Anomalous hall crystals in rhombohedral multilayer graphene ii: General mechanism and a minimal model** (2024), [arXiv:2403.05522](https://arxiv.org/abs/2403.05522).
- [124] K. Huang, S. D. Sarma, and X. Li, **Impurity-induced thermal crossover in fractional chern insulators** (2024), [arXiv:2409.04349](https://arxiv.org/abs/2409.04349).
- [125] T. Tan, J. May-Mann, and T. Devakul, **Wavefunction approach to the fractional anomalous hall crystal** (2024), [arXiv:2409.06775](https://arxiv.org/abs/2409.06775).
- [126] Z. Dong, A. S. Patri, and T. Senthil, **Theory of quantum anomalous hall phases in pentalayer rhombohedral**

- graphene moiré structures (2024), [arXiv:2311.03445](https://arxiv.org/abs/2311.03445).
- [127] K. Huang, X. Li, S. Das Sarma, and F. Zhang, Self-consistent theory of fractional quantum anomalous hall states in rhombohedral graphene, *Physical Review B* **110**, 115146 (2024).
- [128] S. Das Sarma and M. Xie, Thermal crossover from a chern insulator to a fractional chern insulator in pentalayer graphene, *Physical Review B* **110**, 155148 (2024).
- [129] M. Xie and S. Das Sarma, Integer and fractional quantum anomalous hall effects in pentalayer graphene, *Physical Review B* **109**, L241115 (2024).
- [130] Z. Dong, A. S. Patri, and T. Senthil, Stability of anomalous hall crystals in multilayer rhombohedral graphene (2024), [arXiv:2403.07873](https://arxiv.org/abs/2403.07873).
- [131] K. Kudo, R. Nakai, and K. Nomura, Quantum anomalous, quantum spin, and quantum valley hall effects in pentalayer rhombohedral graphene (2024), [arXiv:2406.14354](https://arxiv.org/abs/2406.14354).
- [132] B. Zhou and Y.-H. Zhang, New classes of quantum anomalous hall crystals in multilayer graphene (2024), [arXiv:2411.04174](https://arxiv.org/abs/2411.04174).
- [133] T. Zhang, N. Regnault, B. A. Bernevig, X. Dai, and H. Weng, O (N) *ab initio* calculation scheme for large-scale moiré structures, *Physical Review B* **105**, 125127 (2022).
- [134] OpenMX Forum, Forces and symmetry, <https://www.openmx-square.org/forum/patio.cgi?mode=view&no=119> (2006).
- [135] OpenMX Forum, Use of symmetry in openmx, <https://www.openmx-square.org/forum/patio.cgi?mode=view&no=1287> (2011).

## CONTENTS

I. Introduction	1
II. DFT-Based Structural and Electronic Calculations	2
III. Constructing Continuum Model	3
A. Low-energy DFT Hamiltonian	4
B. Determining Parameter Values	5
C. Plane Wave Reduction	6
IV. Conclusion	7
V. Method	7
A. Parameter Relations	7
B. Orthonormalization and Projection	8
C. Quantum Metric and Berry Curvature	8
VI. Acknowledgments	8
References	10
A. Crystal Structure Relaxation and DFT Calculation	15
1. Crystal Structure Relaxation	15
2. DFT Calculation	16
B. TAPW with Non-orthogonal Basis	17
1. Construction of the TAPW Basis	17
2. Symmetrization of the Hamiltonian	19
C. Building Analytical Models without Fitting	19
1. Continuum Model Basis Construction	20
2. Projection of DFT Hamiltonian onto the Continuum Basis	21
3. Continuum Model Construction	23
D. Constructing continuum model of AA-stacked $t\text{MoTe}_2$ and $t\text{WSe}_2$	27
1. Procedure for Constructing the Continuum Model	28
2. Symmetry Constraints	31
3. Results and Validation	31

### Appendix A: Crystal Structure Relaxation and DFT Calculation

Accurate determination of electronic properties in moiré systems requires precise relaxation of the crystal structure followed by detailed electronic structure calculations. In this section, we outline our methodology for structural relaxation using Machine Learning Force Fields (MLFF) and subsequent Density Functional Theory (DFT) calculations to obtain reliable electronic band structures for  $t\text{MoTe}_2$  and  $t\text{WSe}_2$ .

#### 1. Crystal Structure Relaxation

To accurately predict the band structures of twisted materials, it is essential to relax the crystal structure with high precision. Given the substantial number of atoms in the moiré supercell (e.g., 4326 atoms for a  $2.13^\circ t\text{MoTe}_2$ ), traditional relaxation methods encounter considerable convergence issues. To overcome this, we adopted MLFF approach.

The procedure is the following. We constructed small supercells of untwisted AA bilayer  $\text{MoTe}_2$ , each with different in-plane shifts between the top and bottom layers. Then, we ran *ab initio* Molecular Dynamics (MD) simulations on these structures with VASP, collecting data to construct a robust training set. (Specifically, the *ab initio* MD simulations were done through the *ab initio* MD steps in VASP MLFF module since the module is efficient to

generate data [46]. Those data were *not* generated using MLFF, and we will not use the MLFF in that module, since it is not precise.) We built the test data set using the data in pure DFT relaxation of large-angle twisted structures to prevent over-fitting on untwisted structures.

Then, we trained an accurate MLFF using the Allegro package on the training set and chose the optimal model on test set. We use the Allegro package, because it is an accurate MLFF based on E(3) equivariant neural network that respects rotation, reflection, and translation symmetries in 3D space. The optimal model is the MLFF that we want.

The MLFF was then used to relax  $t\text{MoTe}_2$  and  $t\text{WSe}_2$  structures at various angles within the Atomic Simulation Environment. This strategy allowed us to relax even the largest moiré structures efficiently. For  $t\text{MoTe}_2$  with a twist angle of  $2.13^\circ$ , we conducted additional DFT relaxation steps using MLFF-relaxed structures as initial inputs.

## 2. DFT Calculation

To accurately determine the electronic properties of  $t\text{MoTe}_2$  and  $t\text{WSe}_2$ , we performed Density Functional Theory (DFT) calculations within the OpenMX software package, which employs norm-conserving pseudopotentials and pseudo-atomic localized basis functions. Same calculations can be done using other software such as SIESTA and ABACUS, which are based on numerical atomic orbitals. The method here is of course not limited to  $t\text{MoTe}_2$  and  $t\text{WSe}_2$ .

To ensure computational efficiency and accuracy, the convergence of the charge density in our DFT calculations only involves the  $\Gamma$  point with a stringent convergence criterion of  $10^{-7}$  Hartree in the Kohn-Sham energy. For systems with SOC, we utilized a two-step method [133] available in OpenMX to efficiently account for SOC effects without compromising accuracy. Initially, collinear DFT calculations were conducted to obtain a converged charge density, which was then utilized as an initial guess for subsequent non-collinear DFT calculations. This approach typically achieved convergence within a single step. This method reduces computational cost by treating SOC perturbations in the band energy, ensuring both accuracy and efficiency.

The basis functions employed for these DFT calculations were specified as Mo7.0- $s3p2d2$ , Te7.0- $s3p2d2f1$ , W7.0- $s3p2d2$ , and Se7.0- $s3p2d1$ . The "7.0" indicates the cutoff radius of the pseudo-atomic orbital (PAO) functions in Bohr units. The notation  $s3p2d2$  for Mo indicates 3  $s$ -orbitals, 2 sets of  $p$ -orbitals, and 2 sets of  $d$ -orbitals, yielding a total of 19 PAO basis functions for each Mo atom ( $3 + 2 \times 3 + 2 \times 5$ ). Similarly, Te, W, and Se utilized 26, 19, and 16 basis functions, respectively. For  $t\text{MoTe}_2$ , we selected the standard basis recommended by the OpenMX manual, but the parameters for the quick-basis DFT-based continuum model are also provided in App. [D]. While for  $t\text{WSe}_2$ , we have so far used the quick basis selection.

To evaluate the suitability of different basis configurations, we benchmarked the electronic band structures of  $3.89^\circ$   $t\text{MoTe}_2$  as shown in Fig. 6. Here, we compare the results from OpenMX using various PAO configurations against VASP-calculated bands. Notably, the PAO basis shown in subfigure (c) was selected for  $t\text{MoTe}_2$ , as it provided an optimal balance between computational cost and accuracy in describing the low-energy K-valley bands.

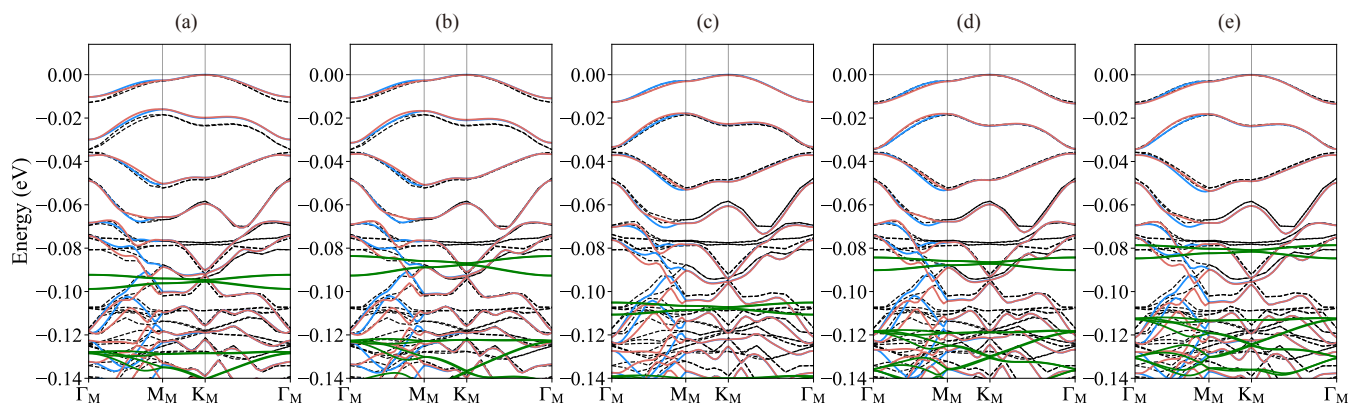


FIG. 6. **Band structures of  $3.89^\circ$   $t\text{MoTe}_2$  with different PAO basis.** Black dotted lines represent the bands calculated using VASP, while blue, red, and green lines represent the K-valley, K'-valley, and  $\Gamma$ -valley bands calculated using OpenMX, respectively. (a): Mo7.0- $s3p2d1$  and Te7.0- $s3p2d2$  (quick basis). (b): Mo7.0- $s3p3d2$  and Te7.0- $s3p3d2$ . (c): Mo7.0- $s3p2d2$  and Te7.0- $s3p2d2f1$  (standard basis). (d): Mo7.0- $s3p2d2f1$  and Te7.0- $s3p3d2f1$ . (e): Mo7.0- $s3p3d2f1$  and Te7.0- $s3p3d2f1$  (precise basis). As we are primarily interested in the K-valley bands in the low-energy region and considering the computational resources, we ultimately selected the basis shown in subfigure (c) for  $t\text{MoTe}_2$ .



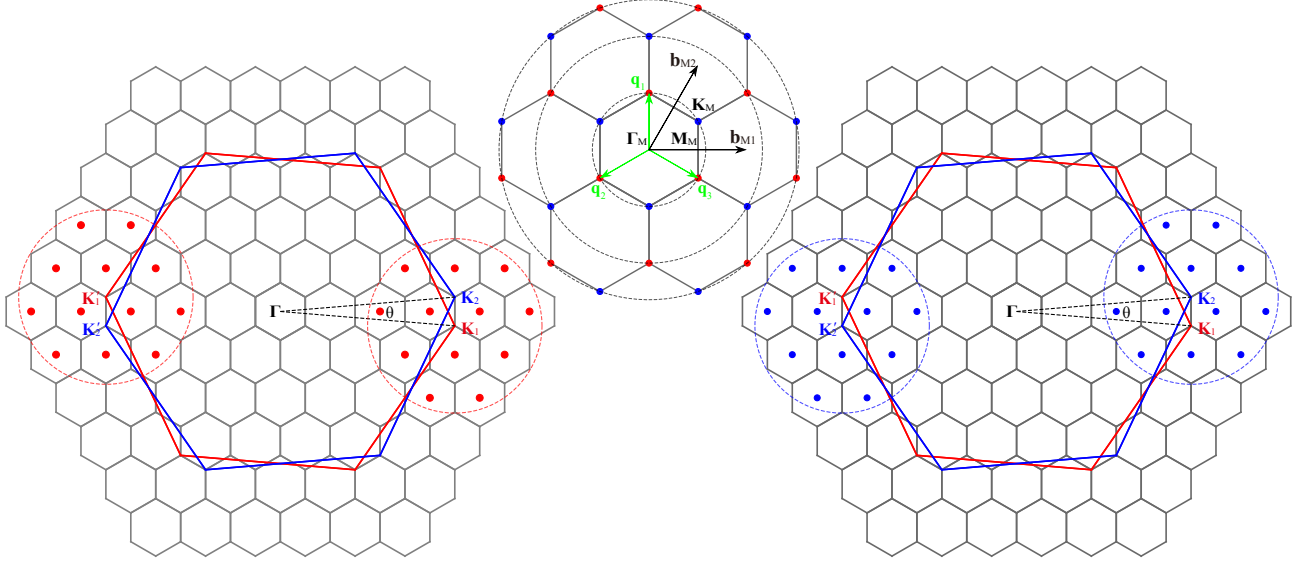


FIG. 7. **Brillouin zone and moiré reciprocal lattice for  $9.43^\circ$   $t\text{MoTe}_2$ .** The red and blue hexagons correspond to the monolayer Brillouin zones (BZ) of the bottom ( $l = 1$ ) and top ( $l = 2$ ) layers, respectively, each rotated by  $\theta/2$  relative to the non-twisted BZ.  $\mathbf{b}_{M1}$  and  $\mathbf{b}_{M2}$  represent the moiré reciprocal lattice vectors. The  $\mathbf{q}$  vectors are defined as  $\mathbf{q}_1 = \mathbf{K}_2 - \mathbf{K}_1$ ,  $\mathbf{q}_2 = C_{3z}\mathbf{q}_1$ , and  $\mathbf{q}_3 = C_{3z}\mathbf{q}_2$ , here  $\mathbf{K}_l$  means  $\mathbf{K}$  point in the  $l$ -th layer's monolayer BZ. In the left panel, the red dots denote the  $\tilde{\mathbf{G}}_l$  vectors chosen in the bottom layer, while the blue dots in the right panel denote those in the top layer, with their origins at the  $\Gamma$  point of the monolayer BZ. The middle panel shows the  $\mathbf{Q}$  vectors we used in the continuum model, where the red dots correspond to  $\mathbf{Q}$  vectors in the top layer, and the blue dots correspond to those in the bottom layer. Each layer's  $\mathbf{Q}_l$  vectors are defined relative to the corresponding  $\mathbf{K}_l$  points, and satisfy the relation  $\tilde{\mathbf{G}}_l + \mathbf{Q}_l = \mathbf{K}_l$ . The dashed circles centered at each layer's  $\mathbf{K}$  point indicates the range from which we select the  $\tilde{\mathbf{G}}$  vectors used to project the original full Hamiltonian.

## Appendix B: TAPW with Non-orthogonal Basis

In this section, we will discuss the construction of a Truncated Atomic Plane Wave (TAPW) basis Hamiltonian derived from the DFT-calculated full Hamiltonian, which serves as the foundation for our subsequent continuum model. This TAPW approach retains the high precision of the full Hamiltonian in capturing low-energy physics while achieving substantial computational savings.

### 1. Construction of the TAPW Basis

The low-energy physics of moiré materials is primarily dominated by states near specific valleys, particularly for small twist angles. To focus on these regions, we define the non-orthogonal truncated atomic plane wave basis centered around a specific valley for the  $l$ -th layer as follows:

$$|\psi_{l,\tilde{\mathbf{G}}_l,\alpha}(\mathbf{k})\rangle = \frac{1}{\sqrt{N_m N_a}} \sum_{\mathbf{R}_1, i} e^{i(\mathbf{k} + \tilde{\mathbf{G}}_l)(\mathbf{R}_1 + \tau_{li\alpha})} |\phi_\alpha(\mathbf{R}_1 + \tau_{li\alpha})\rangle, \quad (\text{B1})$$

where  $\tilde{\mathbf{G}}_l$  is a moiré reciprocal lattice vector in the  $l$ -th layer in the DFT convention which is chosen around the given valley (e.g. see Fig. 7 for K valley),  $\mathbf{k} + \tilde{\mathbf{G}}_l$  is the monolayer momentum, and  $\mathbf{k}$  denotes the momentum in the first moiré Brillouin zone.  $N_m$  and  $N_a$  denote the numbers of moiré unit cells and the number of non-twisted unit cells in one layer, respectively.  $\mathbf{R}_1$  is the lattice vector of the moiré unit cell,  $\tau_{li\alpha}$  is the displacement of  $\alpha$ -th orbital in the  $i$ -th unit cell of  $l$ -th layer.  $\alpha \equiv (aplm)$  represents an atom number index  $a$ , an organized orbital index comprising a multiplicity index  $p$ , an angular momentum quantum number  $l$ , and a magnetic quantum number  $m$ .

For K valley in  $t\text{MoTe}_2$  and  $t\text{WSe}_2$ , the  $\tilde{\mathbf{G}}_l$  vectors for each layer are selected to exhibit  $C_{3z}$  symmetry with respect to the high-symmetry  $\mathbf{K}_l$  point of the corresponding monolayer (see Fig. 7) and are truncated based on the twist angle, with smaller angles requiring higher harmonics for accurate projection. We would like to emphasize that we

cannot include many  $\tilde{\mathbf{G}}_l$  indefinitely, since at some point they will connect the two valleys. We want to avoid the unnecessary double counting from two valleys. This transforms the atom basis into an atomic plane wave basis and enables an efficient representation of the low-energy physics in moiré superlattices. So the Kohn-Sham Bloch state  $|\Psi_\mu(\mathbf{k})\rangle$ , which is the eigenstate of the Kohn-Sham Hamiltonian, can be written as linear combination of the atomic plane wave basis:

$$|\Psi_\mu(\mathbf{k})\rangle = \sum_{l\tilde{\mathbf{G}}_{l\alpha}} c_{l\tilde{\mathbf{G}}_{l\alpha}}^\mu(\mathbf{k}) |\psi_{l,\tilde{\mathbf{G}}_{l\alpha}}(\mathbf{k})\rangle, \quad (\text{B2})$$

where  $c_{l\tilde{\mathbf{G}}_{l\alpha}}^\mu(\mathbf{k})$  is an expansion coefficient. For the simplicity of the notation, we will use  $n$  to label  $\tilde{\mathbf{G}}_l$ , *i.e.*,  $\tilde{\mathbf{G}}_{ln}$  is the value of the  $n$ -th  $\tilde{\mathbf{G}}_l$ , which for example, leads to

$$c_{ln\alpha}^\mu(\mathbf{k}) = c_{l\tilde{\mathbf{G}}_{ln\alpha}}^\mu(\mathbf{k}). \quad (\text{B3})$$

Substituting it into Kohn-Sham equation, we obtain:

$$\sum_{ln\alpha} H_{l'm\beta,ln\alpha}^{\text{TAPW}}(\mathbf{k}) c_{ln\alpha}^\mu(\mathbf{k}) = \sum_{ln\alpha} \epsilon_\mu(\mathbf{k}) S_{l'm\beta,ln\alpha}^{\text{TAPW}}(\mathbf{k}) c_{ln\alpha}^\mu(\mathbf{k}), \quad (\text{B4})$$

where

$$\begin{aligned} H_{l'm\beta,ln\alpha}^{\text{TAPW}}(\mathbf{k}) &= \langle \psi_{l'm\beta}(\mathbf{k}) | \hat{H} | \psi_{ln\alpha}(\mathbf{k}) \rangle, \\ S_{l'm\beta,ln\alpha}^{\text{TAPW}}(\mathbf{k}) &= \langle \psi_{l'm\beta}(\mathbf{k}) | \psi_{ln\alpha}(\mathbf{k}) \rangle, \end{aligned} \quad (\text{B5})$$

are the Hamiltonian matrix element and the overlap matrix element, respectively. Utilizing Eq. (B1), we can obtain

$$\begin{aligned} \langle \psi_{ln\alpha}(\mathbf{k}) | \hat{H} | \psi_{l'm\beta}(\mathbf{k}) \rangle &= \frac{1}{N_m N_a} \sum_{\text{IJ}, ij} e^{-i(\mathbf{k} + \tilde{\mathbf{G}}_{ln})(\mathbf{R}_I + \tau_{l\alpha})} t(\mathbf{R}_I - \mathbf{R}_J + \tau_{l\alpha} - \tau_{l'\beta}) e^{i(\mathbf{k} + \tilde{\mathbf{G}}_{l'm})(\mathbf{R}_J + \tau_{l'\beta})} \\ &= \frac{1}{N_m N_a} \sum_{\text{IJ}, ij} e^{-i\tilde{\mathbf{G}}_{ln}\tau_{l\alpha}} e^{-i\mathbf{k}(\mathbf{R}_I - \mathbf{R}_J + \tau_{l\alpha} - \tau_{l'\beta})} t(\mathbf{R}_I - \mathbf{R}_J + \tau_{l\alpha} - \tau_{l'\beta}) e^{i\tilde{\mathbf{G}}_{l'm}\tau_{l'\beta}} \\ &= \frac{1}{N_m N_a} \sum_{\text{I}, ij} e^{-i\tilde{\mathbf{G}}_{ln}\tau_{l\alpha}} e^{-i\mathbf{k}\bar{\tau}_{l\alpha, l'\beta}} t(\bar{\tau}_{l\alpha, l'\beta}) e^{i\tilde{\mathbf{G}}_{l'm}\tau_{l'\beta}} \\ &= \sum_{ij} \left( \frac{e^{-i\tilde{\mathbf{G}}_{ln}\tau_{l\alpha}}}{\sqrt{N_a}} \right) \cdot [e^{-i\mathbf{k}\bar{\tau}_{l\alpha, l'\beta}} t(\bar{\tau}_{l\alpha, l'\beta})] \cdot \left( \frac{e^{i\tilde{\mathbf{G}}_{l'm}\tau_{l'\beta}}}{\sqrt{N_a}} \right) \\ &= \sum_{ij} X_{li\alpha, ln\alpha}^\dagger H_{li\alpha, l'j\beta}(\mathbf{k}) X_{l'j\beta, l'm\beta}, \end{aligned} \quad (\text{B6})$$

where  $X_{li\alpha, ln\alpha} = e^{i\tilde{\mathbf{G}}_{ln}\tau_{l\alpha}}/\sqrt{N_a}$ ,  $H_{li\alpha, l'j\beta}(\mathbf{k}) = e^{-i\mathbf{k}\bar{\tau}_{l\alpha, l'\beta}} t(\bar{\tau}_{l\alpha, l'\beta})$ , and  $\bar{\tau}_{l\alpha, l'j\beta}$  means the nearest displacement between orbital  $(l, i, \alpha)$  and  $(l', j, \beta)$ ,  $t(\bar{\tau}_{l\alpha, l'j\beta})$  is the real space hopping between nearest orbital  $(l, i, \alpha)$  and  $(l', j, \beta)$  directly get from OpenMX's output Hamiltonian. Similarly, for the overlap matrix element, we have

$$\langle \psi_{l'm\beta}(\mathbf{k}) | \psi_{ln\alpha}(\mathbf{k}) \rangle = \sum_{ij} X_{li\alpha, ln\alpha}^\dagger S_{li\alpha, l'j\beta}(\mathbf{k}) X_{l'j\beta, l'm\beta}, \quad (\text{B7})$$

with  $S_{li\alpha, l'j\beta}(\mathbf{k}) = e^{-i\mathbf{k}\bar{\tau}_{l\alpha, l'j\beta}} s(\bar{\tau}_{l\alpha, l'j\beta})$ , and  $s(\bar{\tau}_{l\alpha, l'j\beta})$  is the overlap between nearest orbital  $(l, i, \alpha)$  and  $(l', j, \beta)$  directly get from OpenMX's output overlap matrix. Now, we can write down the Hamiltonian and overlap matrix in a more compact form,

$$\begin{aligned} H^{\text{TAPW}}(\mathbf{k}) &= X^\dagger H(\mathbf{k}) X, \\ S^{\text{TAPW}}(\mathbf{k}) &= X^\dagger S(\mathbf{k}) X, \end{aligned} \quad (\text{B8})$$

where  $H(\mathbf{k})$  and  $S(\mathbf{k})$  are exactly the full tight-binding and overlap matrices, and  $X$  is the plane wave projector. This projection yields a TAPW basis Hamiltonian that retains key features of the original DFT Hamiltonian while enabling substantial computational efficiency.

To simplify the generalized eigenvalue problem, we apply Löwdin orthogonalization to the overlap matrix, this involves defining a normalized Hamiltonian by incorporating the inverse square root of the overlap matrix:

$$H_{\text{DFT}}(\mathbf{k}) = (S^{\text{TAPW}}(\mathbf{k}))^{-1/2} H^{\text{TAPW}}(\mathbf{k}) (S^{\text{TAPW}}(\mathbf{k}))^{-1/2}. \quad (\text{B9})$$

This orthogonalization process yields an orthonormal set of basis functions:

$$|\tilde{\psi}_{l n \alpha}(\mathbf{k})\rangle = \sum_{l' m \beta} (S^{\text{TAPW}})^{-1/2}_{l n \alpha, l' m \beta} |\psi_{l' m \beta}(\mathbf{k})\rangle \quad (\text{B10})$$

This orthogonal basis ensures that the overlap matrix becomes the identity matrix,  $\langle \tilde{\psi}_{l n \alpha}(\mathbf{k}) | \tilde{\psi}_{l' m \beta}(\mathbf{k}) \rangle = \delta_{l n \alpha, l' m \beta}$ , transforming the generalized eigenvalue problem into a standard one.

## 2. Symmetrization of the Hamiltonian

Numerical artifacts in OpenMX DFT calculations, particularly those arising from the use of conventional regular grids for Fast Fourier Transforms (FFT) and numerical integrations, can disrupt the intrinsic symmetries of the Hamiltonian[134, 135]. In our case, the intrinsic  $C_{3z}$  symmetry of the atomic structure in  $t\text{MoTe}_2$  may not be perfectly preserved due to these numerical issues. Increasing the cutoff energy (e.g., to 400-500 Ryd) can mitigate this issue by enhancing the resolution of the grid but requires a high computational cost. To balance efficiency and accuracy, we adopt an alternative strategy: performing DFT calculations with a moderate cutoff and manually restore the desired symmetries in the Hamiltonian.

To restore the broken  $C_{3z}$  symmetry, we construct a symmetrized Hamiltonian by averaging over all  $C_{3z}$  symmetry operations.

$$\tilde{H}(\mathbf{k}) = \frac{1}{3} [H(\mathbf{k}) + D(C_{3z})H(C_{3z}^{-1}\mathbf{k})D(C_{3z})^\dagger + D(C_{3z}^2)H(C_{3z}^{-2}\mathbf{k})D(C_{3z}^2)^\dagger]. \quad (\text{B11})$$

For a certain valley like K valley,  $C_{3z}$  act on basis (B1) as

$$\begin{aligned} C_{3z} |\psi_{l n \alpha}(\mathbf{k})\rangle &= \frac{1}{\sqrt{N_m N_a}} \sum_{\mathbf{I}, i} e^{i(\mathbf{k} + \tilde{\mathbf{G}}_{ln})(\mathbf{R}_I + \tau_{li\alpha})} C_{3z} |\phi_\alpha(\mathbf{R}_I + \tau_{li\alpha})\rangle \\ &= \frac{1}{\sqrt{N_m N_a}} \sum_{\mathbf{I}, i} e^{iC_{3z}(\mathbf{k} + \tilde{\mathbf{G}}_{ln} - \mathbf{K}_l + \mathbf{K}_l)(\mathbf{R}_I + \tau_{li\alpha})} \sum_{m'} D_{m', m}^j(C_{3z}) |\phi_{\alpha'}(\mathbf{R}_I + \tau_{li\alpha})\rangle \\ &= \frac{1}{\sqrt{N_m N_a}} \sum_{\mathbf{I}, i} e^{i[C_{3z}(\tilde{\mathbf{G}}_{ln} - \mathbf{K}_l) + \mathbf{K}_l] \tau_{li\alpha}} e^{i[C_{3z}(\mathbf{k} + \mathbf{K}_l) - \mathbf{K}_l](\mathbf{R}_I + \tau_{li\alpha})} \sum_{m'} D_{m', m}^j(C_{3z}) |\phi_{\alpha'}(\mathbf{R}_I + \tau_{li\alpha})\rangle \quad (\text{B12}) \\ &= \frac{1}{\sqrt{N_m N_a}} \sum_{\mathbf{I}, i} \sum_{n'} D_{n', n}^l(C_{3z}) e^{i\tilde{\mathbf{G}}_{ln'} \tau_{li\alpha}} e^{i[C_{3z}(\mathbf{k} + \mathbf{K}_l) - \mathbf{K}_l](\mathbf{R}_I + \tau_{li\alpha})} \sum_{m'} D_{m', m}^j(C_{3z}) |\phi_{\alpha'}(\mathbf{R}_I + \tau_{li\alpha})\rangle \\ &= \sum_{n', m'} D_{n', n}^l(C_{3z}) D_{m', m}^j(C_{3z}) |\psi_{l n' \alpha'}(C_{3z}(\mathbf{k} + \mathbf{K}_l) - \mathbf{K}_l)\rangle, \end{aligned}$$

where  $D_{n', n}^l(C_{3z}) = \delta_{\tilde{\mathbf{G}}_{ln'}, C_{3z}(\tilde{\mathbf{G}}_{ln} - \mathbf{K}_l) + \mathbf{K}_l}$ ,  $\tilde{\mathbf{G}}_l$  represents  $\tilde{\mathbf{G}}$  vectors in the  $l$ -th layer,  $D_{m', m}^j(C_{3z})$  represents Wigner D-matrix for  $C_{3z}$  rotation,  $j$  is the total angular momentum quantum number of orbital  $\alpha$ . The summation over  $\alpha'$  indicates that the sum is taken only over the magnetic quantum number  $m'$  within, while the other components  $\alpha'$  remain fixed. By enforcing this symmetrization, we ensure that the physical symmetry of the system is preserved, which is crucial for accurate band structure calculations.

As illustrated in Fig. 8, the symmetrized Hamiltonian accurately captures the essential features of the moiré band structures for both  $t\text{MoTe}_2$  and  $t\text{WSe}_2$  across various twist angles.

## Appendix C: Building Analytical Models without Fitting

In this section, we present a general method to derive continuum models directly from DFT calculation *without fitting*, applicable to both homostructures and heterostructures across any number of layers in any valley. The method generates two model types: (i) a numerically precise model suitable for further numerical calculations and (ii) an analytical model focused on low-energy physics, sacrificing precision in higher-(absolute) energy bands to facilitate analytical study. In the following discussion, we concentrate on a single valley.

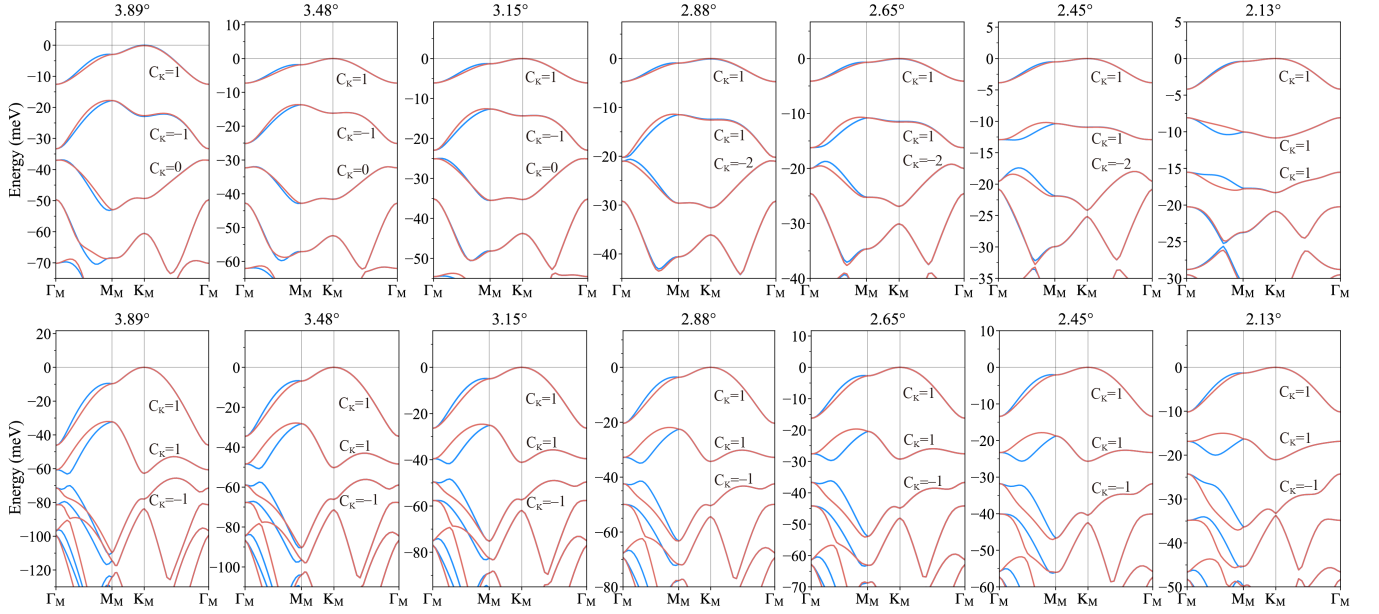


FIG. 8. **Band structures of  $t\text{MoTe}_2$  and  $t\text{WSe}_2$  calculated with the TAPW method.** Results are shown for twist angles from  $3.89^\circ$  to  $2.13^\circ$  with symmetrized Hamiltonians. For  $t\text{MoTe}_2$  (upper panels),  $\tilde{\mathbf{G}}$  lattices up to the 7th harmonic for angles from  $3.89^\circ$  to  $3.15^\circ$ , and up to the 8th harmonic from  $2.88^\circ$  to  $2.13^\circ$ . For  $t\text{WSe}_2$  (lower panels),  $\tilde{\mathbf{G}}$  lattice up to the 7th harmonic from  $3.89^\circ$  to  $3.48^\circ$ , and up to the 8th harmonic from  $3.15^\circ$  to  $2.13^\circ$ . Blue lines represent K-valley bands, while red lines represent K'-valley bands.

### 1. Continuum Model Basis Construction

Within a given valley, the different layers of a twisted system can host distinct sub-valleys, which determine the electrons' momenta, or more precisely, the eigenvalues of the moiré translation operator. For example, in  $t\text{MoTe}_2$ , the twist angle between layers shifts the monolayer K points within the K valley, effectively generating separate sub-valleys corresponding to each layer. However, in the  $\Gamma$  valley, both layers share a common sub-valley since the  $\Gamma$  point remains invariant under rotations, meaning layer information must be encoded differently (than in the momentum shift) here.

To define the basis of the continuum model, we use  $\psi_{\mathbf{r},v,a_v}^\dagger$ , where  $\mathbf{r}$  represents the 2D continuum position,  $v = \text{K}_1, \text{K}_2, \Gamma \dots$  is the sub-valley index denoting the valley that we investigate,  $a_v$  encompasses all additional indices relevant to sub-valley  $v$ . For example, in the K valley of  $t\text{MoTe}_2$ ,  $a_v$  comprises only the orbital index, such as the  $d_{x^2-y^2} + id_{xy}$  orbital, since the sub-valleys  $\text{K}_1$  and  $\text{K}_2$  already correspond to different layer, allowing layer differentiation via  $v$ . In contrast, in the  $\Gamma$  valley, where sub-valleys are indistinguishable,  $a_v$  must include both orbital and layer indices. Thus, in the K valley,  $a_v$  pertains solely to the orbital index, while in the  $\Gamma$  valley, it also incorporates layer information. Additionally, in homobilayer structures, the orbital range of  $a_v$  is identical across sub-valleys within any given valley, allowing simplification of the notation to  $a$ . However, for heterobilayer structures, the orbital values represented by  $a_v$  can differ between sub-valleys, necessitating the retention of  $a_v$  to accurately capture the distinct orbital characteristics of each sub-valley. Furthermore, if the spin-valley coupling is not sufficiently strong,  $a_v$  can also include spin degrees of freedom.

Suppose the moiré lattice translation operator is  $T_{\mathbf{R}_M}$ , and then continuum basis  $\psi_{\mathbf{r},v,a_v}^\dagger$  transforms as

$$T_{\mathbf{R}_M} \psi_{\mathbf{r},v,a_v}^\dagger T_{\mathbf{R}_M}^{-1} = e^{-i\mathbf{R}_M \cdot (\mathbf{K}_0 + \mathbf{q}_v)} \psi_{\mathbf{r} + \mathbf{R}_M, v, a_v}^\dagger, \quad (\text{C1})$$

where  $\mathbf{K}_0$  is the monolayer momentum that corresponding to the  $\Gamma_M$  in the moiré Brillouin zone, and  $\mathbf{q}_v$  labels the deviation from  $\mathbf{K}_0$  to the sub-valley  $v$ , with  $\mathbf{K}_0 + \mathbf{q}_v = v$ . It is important to note that we do not distinguish between two sub-valleys if they differ by moiré reciprocal lattice vectors, as such differences result in identical phases under moiré lattice translations.

With the defined  $\mathbf{q}_v$ , we can naturally express the Fourier transformation of the continuum basis  $\psi_{\mathbf{r},v,a_v}^\dagger$  into

momentum space, which is given by

$$\psi_{\mathbf{k}-\mathbf{G}_M-\mathbf{q}_v, v, a_v}^\dagger = \frac{1}{\sqrt{\mathcal{A}}} \int d^2r e^{i\mathbf{r}\cdot(\mathbf{k}-\mathbf{G}_M-\mathbf{q}_v)} \psi_{\mathbf{r}, v, a_v}^\dagger, \quad (\text{C2})$$

where  $\mathbf{k}$  is the momentum in the moiré Brillouin zone,  $\mathbf{G}_M$  is the moiré reciprocal lattice vector,  $\mathcal{A}$  is the total area of the sample, and we do not include  $\mathbf{K}_0$  in the Fourier transformation. In this way, the basis has the following transformation property under moiré lattice translations:

$$T_{\mathbf{R}_M} \psi_{\mathbf{k}-\mathbf{G}_M-\mathbf{q}_v, v, a_v}^\dagger T_{\mathbf{R}_M}^{-1} = e^{-i\mathbf{R}_M\cdot(\mathbf{k}-\mathbf{G}_M+\mathbf{K}_0)} \psi_{\mathbf{k}-\mathbf{G}_M-\mathbf{q}_v, v, a_v}^\dagger. \quad (\text{C3})$$

By defining

$$\mathbf{Q} = \mathbf{G}_M + \mathbf{q}_v, \quad (\text{C4})$$

we obtain  $\psi_{\mathbf{k}, \mathbf{Q}, a_{\mathbf{Q}}}^\dagger$ , which serves as the basis of the continuum model, as  $\mathbf{Q}$  is one-to-one mapped to the pair  $(\mathbf{G}_M, \mathbf{q}_v)$ , where

$$a_{\mathbf{Q}} = a_v \text{ iff } \mathbf{Q} \in \{\mathbf{b}_{M_1}\mathbb{Z} + \mathbf{b}_{M_2}\mathbb{Z} + \mathbf{q}_v\}, \quad (\text{C5})$$

where  $\mathbf{b}_{M_1}$  and  $\mathbf{b}_{M_2}$  are two primitive reciprocal lattice vectors, and  $\mathbb{Z}$  denotes the integer set. We now define the main reason for us to define the concept of sub-valleys, instead of using only the layer index. Taking the  $\Gamma$  valley in  $t\text{MoTe}_2$  as an example, the two layers would have the same  $\mathbf{Q}$ , and thus it is impossible to use  $\mathbf{Q}$  to cover both  $\mathbf{G}_M$  and layer index.  $\mathbf{Q}$  can only cover both  $\mathbf{G}_M$  and the sub-valleys.

## 2. Projection of DFT Hamiltonian onto the Continuum Basis

The next step is constructing  $\psi_{\mathbf{k}, \mathbf{Q}, a_{\mathbf{Q}}}^\dagger$  (see Eqs. (C2) and (C4)) from the DFT calculations. Firstly, note that the TAPW basis can be expressed as  $c_{\mathbf{k}+\tilde{\mathbf{G}}_M, \alpha_{\mathbf{Q}}}^\dagger$ , where  $\alpha_{\mathbf{Q}}$  is the multiplicity index of orbital and layer, similarly as  $a_{\mathbf{Q}}$  in Eq. (C5), only in K valley of homobilayer system index  $\alpha_{\mathbf{Q}}$  can be simplified as  $\alpha$ , which is the same notation we used in App. [B], as layer information is naturally composed in  $\mathbf{q}_v$ . Second, to align  $\mathbf{Q} = \mathbf{G}_M + \mathbf{q}_v$  with the plane waves used in the TAPW calculations, we select  $\mathbf{G}_M = \mathbf{K}_0 - \tilde{\mathbf{G}}_l$ , ensuring a one-to-one correspondence between  $\mathbf{Q}$  in the continuum model and  $\tilde{\mathbf{G}}_l$  chosen in TAPW. We refer to this continuum model projected onto these selected  $\mathbf{Q}$  points as the ‘‘full model’’. Consequently, the DFT basis can be simplified as  $c_{\mathbf{k}+\mathbf{K}_0, \mathbf{Q}, \alpha_{\mathbf{Q}}}^\dagger \equiv c_{\mathbf{k}+\mathbf{K}_0+\mathbf{q}_{v_{\mathbf{Q}}}-\mathbf{Q}, \alpha_{\mathbf{Q}}}^\dagger$ , where we used Eqs. (C4) and (C5), where  $v_{\mathbf{Q}}$  denotes the sub-valley containing  $\mathbf{Q}$ . Thus,  $H_{\text{DFT}}$  around a particular valley can be expressed as:

$$H_{\text{DFT}} = \sum_{\mathbf{k}} \sum_{\mathbf{Q}_1 \mathbf{Q}_2} \sum_{\alpha_{\mathbf{Q}_1} \alpha'_{\mathbf{Q}_2}} c_{\mathbf{k}+\mathbf{K}_0, \mathbf{Q}_1, \alpha_{\mathbf{Q}_1}}^\dagger [H_{\text{DFT}}(\mathbf{k})]_{\mathbf{Q}_1 \alpha_{\mathbf{Q}_1}, \mathbf{Q}_2 \alpha'_{\mathbf{Q}_2}} c_{\mathbf{k}+\mathbf{K}_0, \mathbf{Q}_2, \alpha'_{\mathbf{Q}_2}}, \quad (\text{C6})$$

We want to emphasize that the key difference between  $\psi_{\mathbf{k}, \mathbf{Q}, a_{\mathbf{Q}}}^\dagger$  in Eq. (C2) and  $c_{\mathbf{k}+\mathbf{K}_0, \mathbf{Q}, \alpha_{\mathbf{Q}}}^\dagger$  lies in the restriction on the index  $a_{\mathbf{Q}}$ , since we normally want  $a_{\mathbf{Q}}$  to take much less values of  $\alpha_{\mathbf{Q}}$ . For example, in the K valley of  $t\text{MoTe}_2$  (for which  $a_{\mathbf{Q}}$  and  $\alpha_{\mathbf{Q}}$  can be simplified as  $a$  and  $\alpha$  as discussed above),  $\alpha$  spans  $A = 71$  orbitals with spin- $\uparrow$  in one monolayer unit cell due to the Mo- $s3p2d2$  and Te- $s3p2d2f1$  basis sets, whereas  $a$  is limited to only a subset of these orbitals (e.g., the  $d_{z^2}$  orbital or Mo, or combinations like  $d_{x^2-y^2} + id_{xy}$  of Mo, among others). While for the  $\Gamma$  valley, the inclusion of layer index doubles the range of both  $a$  and  $\alpha$ , expanding  $\alpha$  to  $2 \times 71 = 142$ . In the following, we will explain how  $a_{\mathbf{Q}}$  is determined.

The DFT Hamiltonian in Eq. (C6) contains a lot of high-energy degrees of freedom that are irrelevant to the low-energy physics of interest. To simplify Eq. (C6), we recall that the low-energy physics happens among the low-energy states of monolayer Hamiltonians—we always choose the low-energy states of monolayer Hamiltonians as the basis of the continuum model. In other words, the most dominant energy scale in the continuum model is the kinetic energy directly inherited from the monolayer Hamiltonians, which do not couple different  $\mathbf{Q}$ 's for a fixed  $\mathbf{k}$ . Therefore, to isolate the low-energy states, let us consider the  $\mathbf{Q}$  diagonal block of  $H_{\text{DFT}}(\mathbf{k})$ , labeled as  $D_{\mathbf{Q}}(\mathbf{k})$ , which reads:

$$[D_{\mathbf{Q}}(\mathbf{k})]_{\alpha_{\mathbf{Q}} \alpha'_{\mathbf{Q}}} = [H_{\text{DFT}}(\mathbf{k})]_{\mathbf{Q} \alpha_{\mathbf{Q}}, \mathbf{Q} \alpha'_{\mathbf{Q}}}. \quad (\text{C7})$$

Diagonalizing  $D_Q(\mathbf{k})$  yields eigenvalues  $\lambda_n^{\mathbf{k},Q}$  and eigenvectors  $U_n^{\mathbf{k},Q}$ :

$$D_Q(\mathbf{k})U_n^{\mathbf{k},Q} = \lambda_n^{\mathbf{k},Q}U_n^{\mathbf{k},Q} , \quad (\text{C8})$$

where  $n = 1, \dots, N_{\alpha_Q}$  and  $N_{\alpha_Q}$  is the number of distinct  $\alpha_Q$  values. We select a subset of eigenvalues,  $\lambda_{\text{low}}^{\mathbf{k},Q}$ , that meet the following criteria:

1. They are the closest to the Fermi energy among all  $\lambda_n^{\mathbf{k},Q}$ .
2. They are separated from the remaining eigenvalues by a significant gap that is much larger than the spread of the selected  $\lambda_{\text{low}}^{\mathbf{k},Q}$  values.

The count of  $\lambda_{\text{low}}^{\mathbf{k},Q}$  is denoted as  $N_{a_Q}$ . We focus on the wavefunctions corresponding to  $a_Q$ . The corresponding eigenvectors are denoted as  $U_{\text{low}}^{\mathbf{k},Q}$ , with dimensions  $N_{\alpha_Q} \times N_{a_Q}$ . The remaining eigenvalues and eigenvectors are labeled  $\lambda_{\text{high}}^{\mathbf{k},Q}$  and  $U_{\text{high}}^{\mathbf{k},Q}$  with dimension  $N_{\alpha_Q} \times (N_{\alpha_Q} - N_{a_Q})$ , capture the high-energy states.

It is important to note that  $U_{\text{low}}^{\mathbf{k},Q}$  may not exhibit the desired physical symmetry representations due to arbitrary phase factors introduced during numerical diagonalization. To recover the correct symmetry, we apply a unitary transformation  $V^{\mathbf{k},Q}$  to restore symmetry:

$$U_{\text{low}}^{\mathbf{k},Q} \rightarrow V^{\mathbf{k},Q}U_{\text{low}}^{\mathbf{k},Q} . \quad (\text{C9})$$

which is to fix the gauge. For example, we can fix the gauge by choosing a fixed orbital and then making sure its phase in the eigenvectors to be zero. Then, the continuum basis can be constructed from the DFT basis as

$$\psi_{\mathbf{k},Q,a_Q}^\dagger = \sum_{\alpha_Q} c_{\mathbf{k}+K_0,Q,\alpha_Q}^\dagger \left[ U_{\text{low}}^{\mathbf{k},Q} \right]_{\alpha_Q,a_Q} . \quad (\text{C10})$$

This construction preserves the moiré translation properties specified in Eq. (C3), since  $c_{\mathbf{k}+K_0,Q,\alpha_Q}^\dagger$  carries momentum  $\mathbf{k} + K_0 + q_{v_Q} - Q$ .

With the continuum basis established, the next step is to obtain Hamiltonian by directly projecting  $H_{\text{DFT}}(\mathbf{k})$  onto  $U_{a_Q}^{\mathbf{k},Q}$ . To do so, we define a matrix  $U_0(\mathbf{k})$  for the space spanned by  $U_{a_Q}^{\mathbf{k},Q}$ , which reads

$$U_0(\mathbf{k}) = \bigoplus_Q U_{\text{low}}^{\mathbf{k},Q} . \quad (\text{C11})$$

The projected Hamiltonian is then given by:

$$h_{00}(\mathbf{k}) = U_0^\dagger(\mathbf{k})H_{\text{DFT}}(\mathbf{k})U_0(\mathbf{k}) . \quad (\text{C12})$$

In general,  $h_{00}(\mathbf{k})$  may not fully capture low-energy band structure as it only includes the effects within the low-energy subspace and neglects the coupling to the high-energy states. Although these couplings are small, they are essential for accurately describing the physical details of the low-energy states. To account for this, we perform second-order perturbation as follows. Define  $U_1(\mathbf{k})$  as the orthogonal completion of  $U_0(\mathbf{k})$ , such that,

$$U_0(\mathbf{k})U_0^\dagger(\mathbf{k}) + U_1(\mathbf{k})U_1^\dagger(\mathbf{k}) = 1, \quad U_1^\dagger(\mathbf{k})U_0(\mathbf{k}) = 0 . \quad (\text{C13})$$

Explicitly, we can construct  $U_1(\mathbf{k})$  as:

$$U_1(\mathbf{k}) = \bigoplus_Q U_{\text{high}}^{\mathbf{k},Q} , \quad (\text{C14})$$

representing the high-energy Hilbert space of  $\lambda_{\text{high}}^{\mathbf{k},Q}$  (relative to the Fermi energy). The corresponding Hamiltonian reads:

$$h_{11}(\mathbf{k}) = U_1^\dagger(\mathbf{k})H_{\text{DFT}}(\mathbf{k})U_1(\mathbf{k}) , \quad (\text{C15})$$

and the transitions matrix between the low- $\lambda$  and high- $\lambda$  modes is:

$$h_{01}(\mathbf{k}) = U_0^\dagger(\mathbf{k})H_{\text{DFT}}(\mathbf{k})U_1(\mathbf{k}) , \quad (\text{C16})$$

along with its Hermitian conjugate. Then, the corrected DFT Hamiltonian for the continuum basis reads:

$$h_{\text{DFT}}(\mathbf{k}) = h_{00}(\mathbf{k}) + h_{01}(\mathbf{k}) \frac{1}{\bar{\lambda}_{\mathbf{k}} - h_{11}(\mathbf{k})} h_{01}^\dagger(\mathbf{k}) , \quad (\text{C17})$$

where  $\bar{\lambda}_{\mathbf{k}}$  is chosen as the mean value of the eigenvalues of  $h_{00}(\mathbf{k})$ . The mean value is just one choice—one can choose other values within the range of the eigenvalues of  $h_{00}(\mathbf{k})$  if they can provide more accuracy. We use the mean value because it serves as a central reference energy around which we perform the perturbative expansion. With this setup, we derive a model with the continuum basis directly from DFT calculation

$$H_{\text{DFT}} = \sum_{\mathbf{k}} \sum_{\mathbf{Q}_1 \mathbf{Q}_2} \sum_{a_{\mathbf{Q}_1} a'_{\mathbf{Q}_2}} \psi_{\mathbf{k}, \mathbf{Q}_1, a_{\mathbf{Q}_1}}^\dagger [h_{\text{DFT}}(\mathbf{k})]_{\mathbf{Q}_1 a_{\mathbf{Q}_1}, \mathbf{Q}_2 a'_{\mathbf{Q}_2}} \psi_{\mathbf{k}, \mathbf{Q}_2, a'_{\mathbf{Q}_2}} , \quad (\text{C18})$$

where  $\psi_{\mathbf{k}, \mathbf{Q}_1, a_{\mathbf{Q}_1}}^\dagger$  is constructed in Eq. (C10) and  $h_{\text{DFT}}(\mathbf{k})$  is in Eq. (C17).

In principle, one can directly use  $H_{\text{DFT}}$  together with an interaction term to perform any many-body calculation, as long as the interaction term is normal-ordered to avoid the double counting due to the interaction effect included in the DFT calculation. However, direct use of  $H_{\text{DFT}}$  has limitations. Specifically, the DFT-calculated Hamiltonian  $h_{\text{DFT}}(\mathbf{k})$  is defined on a discrete momentum mesh, which restricts flexibility for continuous momentum-space applications. To resolve this issue, we will construct a continuum model that is (nearly) numerically accurate on any momentum mesh in the next subsection.

### 3. Continuum Model Construction

This section introduces a general method to construct a continuum model that enables both accurate numerical calculations and analytical understanding of the low-energy properties of moiré materials. The key advantage of this approach is that it does not require any fitting, instead deriving directly from DFT results.

Recall that the continuum model in the real space have the following general form

$$H_{\text{cont}} = \sum_{m_x, m_y, n_x, n_y \in \mathbb{N}} \sum_{vv'} \sum_{a_v a'_{v'}} \int d^2r (i^m \partial_x^{m_x} \partial_y^{m_y} \psi_{\mathbf{r}, v, a_v}^\dagger) t_{v a_v, v' a'_{v'}}^{m_x m_y n_x n_y}(\mathbf{r}) (-i)^n \partial_x^{n_x} \partial_y^{n_y} \psi_{\mathbf{r}, v', a'_{v'}} , \quad (\text{C19})$$

here,  $m = m_x + m_y$ ,  $n = n_x + n_y$ , and we do not need to explicitly include derivative's on  $t$ 's since acting derivatives on a potential still gives us potentials. Note that Eq. (C19) is equivalent to Eq. (7) in the main text, and the relation will be discussed in and below Eq. (C27). Since we require the model to be moiré lattice transitionally invariant,  $t_{v a_v, v' a'_{v'}}^{m_x m_y n_x n_y}(\mathbf{r})$  has the following general form

$$t_{v a_v, v' a'_{v'}}^{m_x m_y n_x n_y}(\mathbf{r}) = \sum_{\mathbf{G}_M} t_{v a_v, v' a'_{v'}, \mathbf{G}_M}^{m_x m_y n_x n_y} e^{-i(\mathbf{q}_v - \mathbf{q}_{v'} + \mathbf{G}_M) \cdot \mathbf{r}} , \quad (\text{C20})$$

where we have used Eq. (C1), this form permits efficient numerical construction of the Hamiltonian in momentum space. As a result, we can rewrite the Hamiltonian as:

$$H_{\text{cont}} = \sum_{m_x, m_y, n_x, n_y \in \mathbb{N}} \sum_{vv'} \sum_{a_v a'_{v'}} \sum_{\mathbf{G}_M} t_{v a_v, v' a'_{v'}, \mathbf{G}_M}^{m_x m_y n_x n_y} \int d^2r (i^m \partial_x^{m_x} \partial_y^{m_y} \psi_{\mathbf{r}, v, a_v}^\dagger) \times e^{-i(\mathbf{q}_v - \mathbf{q}_{v'} + \mathbf{G}_M) \cdot \mathbf{r}} (-i)^n \partial_x^{n_x} \partial_y^{n_y} \psi_{\mathbf{r}, v', a'_{v'}} . \quad (\text{C21})$$

For numerical implementation, it is efficient to perform the construction of the Hamiltonian in the momentum space.

Using Eq. (C2), we can obtain

$$\begin{aligned}
H_{cont} &= \sum_{m_x, m_y, n_x, n_y \in \mathbb{N}} \sum_{v v'} \sum_{a_v a_{v'}} \sum_{\mathbf{G}_M} t_{v a_v, v' a_{v'}, \mathbf{G}_M}^{m_x m_y n_x n_y} \sum_{\mathbf{k}} \sum_{\mathbf{G}_{M,1} \mathbf{G}_{M,2}} (\mathbf{k} - \mathbf{G}_{M,1} - \mathbf{q}_v)_x^{m_x} (\mathbf{k} - \mathbf{G}_{M,1} - \mathbf{q}_v)_y^{m_y} \\
&\quad \times \psi_{\mathbf{k} - \mathbf{G}_{M,1} - \mathbf{q}_v, a_v}^\dagger \delta_{\mathbf{G}_{M,1} + \mathbf{q}_v, \mathbf{G}_{M,2} + \mathbf{q}_{v'} - \mathbf{q}_v + \mathbf{G}_M} (\mathbf{k} - \mathbf{G}_{M,2} - \mathbf{q}_{v'})_x^{n_x} (\mathbf{k} - \mathbf{G}_{M,2} - \mathbf{q}_{v'})_y^{n_y} \psi_{\mathbf{k} - \mathbf{G}_{M,2} - \mathbf{q}_{v'}, a_{v'}} \\
&= \sum_{m_x, m_y, n_x, n_y \in \mathbb{N}} \sum_{Q Q'} \sum_{a_Q a_{Q'}} \sum_{\mathbf{G}_M} t_{v a_Q, v' a_{Q'}, \mathbf{G}_M}^{m_x m_y n_x n_y} \sum_{\mathbf{k}} (\mathbf{k} - Q)_x^{m_x} (\mathbf{k} - Q)_y^{m_y} \\
&\quad \times \psi_{\mathbf{k}, Q, a_Q}^\dagger \delta_{Q, Q' + \mathbf{q}_{v_Q} - \mathbf{q}_{v_{Q'}} + \mathbf{G}_M} (\mathbf{k} - Q')_x^{n_x} (\mathbf{k} - Q')_y^{n_y} \psi_{\mathbf{k}, Q', a_{Q'}} \\
&= \sum_{m_x, m_y, n_x, n_y \in \mathbb{N}} \sum_{v_1 v_2} \sum_{\mathbf{G}_M} \sum_{a_{v_1} a_{v_2}} t_{v_1 a_{v_1}, v_2 a_{v_2}, \mathbf{G}_M}^{m_x m_y n_x n_y} \sum_{\mathbf{k}} \sum_{Q Q'} \sum_{a_Q a_{Q'}} \psi_{\mathbf{k}, Q, a_Q}^\dagger \psi_{\mathbf{k}, Q', a_{Q'}} \\
&\quad \times \delta_{v_Q a_Q, v_1 a_{v_1}} \delta_{v_{Q'} a_{Q'}, v_2 a_{v_2}} (\mathbf{k} - Q)_x^{m_x} (\mathbf{k} - Q)_y^{m_y} \delta_{Q, Q' + \mathbf{q}_{v_1} - \mathbf{q}_{v_2} + \mathbf{G}_M} (\mathbf{k} - Q')_x^{n_x} (\mathbf{k} - Q')_y^{n_y} \\
&= \sum_{m_x, m_y, n_x, n_y \in \mathbb{N}} \sum_{v_1 v_2} \sum_{\mathbf{G}_M} \sum_{a_{v_1} a_{v_2}} t_{v_1 a_{v_1}, v_2 a_{v_2}, \mathbf{G}_M}^{m_x m_y n_x n_y} \sum_{\mathbf{k}} \sum_{Q Q'} \sum_{a_Q a_{Q'}} \psi_{\mathbf{k}, Q, a_Q}^\dagger \psi_{\mathbf{k}, Q', a_{Q'}} \\
&\quad \times \left[ X_{v_1 a_{v_1}, v_2 a_{v_2}, \mathbf{q}_{v_1} - \mathbf{q}_{v_2} + \mathbf{G}_M}^{m_x m_y n_x n_y}(\mathbf{k}) \right]_{Q a_Q, Q' a_{Q'}} , \tag{C22}
\end{aligned}$$

where

$$\left[ X_{v_1 a_{v_1}, v_2 a_{v_2}, \mathbf{p}}^{m_x m_y n_x n_y}(\mathbf{k}) \right]_{Q a_Q, Q' a_{Q'}} = \delta_{v_Q a_Q, v_1 a_{v_1}} \delta_{v_{Q'} a_{Q'}, v_2 a_{v_2}} (\mathbf{k} - Q)_x^{m_x} (\mathbf{k} - Q)_y^{m_y} \delta_{Q, Q' + \mathbf{p}} (\mathbf{k} - Q')_x^{n_x} (\mathbf{k} - Q')_y^{n_y} . \tag{C23}$$

Then, under the belief that the continuum model should be able to precisely capture  $h_{\text{DFT}}(\mathbf{k})$  in Eq. (C17), we would have

$$h_{\text{DFT}}(\mathbf{k}) = \sum_{m_x, m_y, n_x, n_y \in \mathbb{N}} \sum_{v_1 v_2} \sum_{\mathbf{G}_M} \sum_{a_{v_1} a_{v_2}} t_{v_1 a_{v_1}, v_2 a_{v_2}, \mathbf{G}_M}^{m_x m_y n_x n_y} X_{v_1 a_{v_1}, v_2 a_{v_2}, \mathbf{q}_{v_1} - \mathbf{q}_{v_2} + \mathbf{G}_M}^{m_x m_y n_x n_y}(\mathbf{k}) . \tag{C24}$$

Our goal is to determine the *linearly independent* values of  $t_{v_1 a_{v_1}, v_2 a_{v_2}, \mathbf{G}_M}^{m_x m_y n_x n_y}$  from  $h_{\text{DFT}}(\mathbf{k})$ . Before doing so, we will first show that  $X_{v_1 a_{v_1}, v_2 a_{v_2}, \mathbf{p}}^{m_x m_y n_x n_y}(\mathbf{k})$  ( $\mathbf{q}_{v_1} - \mathbf{q}_{v_2} + \mathbf{G}_M$  is written as  $\mathbf{p}$  for simplicity) terms are orthogonal for different  $(v_1 a_{v_1}, v_2 a_{v_2}, \mathbf{G}_M)$  but not completely linearly independent for  $(m_x, m_y, n_x, n_y)$ . To see so, first note that

$$\begin{aligned}
&\text{Tr} \left\{ \left[ X_{\bar{v}_1 \bar{a}_{\bar{v}_1}, \bar{v}_2 \bar{a}'_{\bar{v}_2}, \bar{\mathbf{p}}}^{\bar{m}_x \bar{m}_y \bar{n}_x \bar{n}_y}(\mathbf{k}) \right]^\dagger X_{v_1 a_{v_1}, v_2 a'_{v_2}, \mathbf{p}}^{m_x m_y n_x n_y}(\mathbf{k}) \right\} \\
&= \sum_{Q a_Q, Q' a_{Q'}} \left[ X_{\bar{v}_1 \bar{a}_{\bar{v}_1}, \bar{v}_2 \bar{a}'_{\bar{v}_2}, \bar{\mathbf{p}}}^{\bar{m}_x \bar{m}_y \bar{n}_x \bar{n}_y}(\mathbf{k}) \right]_{Q a_Q, Q' a_{Q'}}^* \left[ X_{v_1 a_{v_1}, v_2 a'_{v_2}, \mathbf{p}}^{m_x m_y n_x n_y}(\mathbf{k}) \right]_{Q a_Q, Q' a_{Q'}} \\
&= \sum_{Q a_Q, Q' a_{Q'}} \delta_{v_Q a_Q, v_1 a_{v_1}} \delta_{v_{Q'} a_{Q'}, \bar{v}_1 \bar{a}_{\bar{v}_1}} \delta_{v_{Q'} a_{Q'}, v_2 a'_{v_2}} \delta_{v_{Q'} a_{Q'}, \bar{v}_2 \bar{a}'_{\bar{v}_2}} \delta_{Q, Q' + \mathbf{p}} \delta_{Q, Q' + \bar{\mathbf{p}}} (\mathbf{k} - Q)_x^{m_x} (\mathbf{k} - Q)_y^{m_y} (\mathbf{k} - Q)_x^{\bar{m}_x} (\mathbf{k} - Q)_y^{\bar{m}_y} \\
&\quad \times (\mathbf{k} - Q')_x^{n_x} (\mathbf{k} - Q')_y^{n_y} (\mathbf{k} - Q')_x^{\bar{n}_x} (\mathbf{k} - Q')_y^{\bar{n}_y} \\
&= \delta_{v_1 a_{v_1}, \bar{v}_1 \bar{a}_{\bar{v}_1}} \delta_{v_2 a'_{v_2}, \bar{v}_2 \bar{a}'_{\bar{v}_2}} \delta_{\mathbf{p}, \bar{\mathbf{p}}} \sum_{Q a_Q, Q' a_{Q'}} \delta_{v_Q a_Q, v_1 a_{v_1}} \delta_{v_{Q'} a_{Q'}, v_2 a'_{v_2}} \delta_{Q, Q' + \mathbf{p}} (\mathbf{k} - Q)_x^{m_x} (\mathbf{k} - Q)_y^{m_y} (-Q)_x^{\bar{m}_x} (-Q)_y^{\bar{m}_y} \\
&\quad \times (\mathbf{k} - Q')_x^{n_x} (\mathbf{k} - Q')_y^{n_y} (\mathbf{k} - Q')_x^{\bar{n}_x} (\mathbf{k} - Q')_y^{\bar{n}_y} \\
&= 0 \text{ for } (v_1 a_{v_1}, v_2 a'_{v_2}, \mathbf{p}) \neq (\bar{v}_1 \bar{a}_{\bar{v}_1}, \bar{v}_2 \bar{a}'_{\bar{v}_2}, \bar{\mathbf{p}}), \tag{C25}
\end{aligned}$$

meaning that  $X_{\bar{v}_1 \bar{a}_{\bar{v}_1}, \bar{v}_2 \bar{a}'_{\bar{v}_2}, \bar{\mathbf{p}}}^{\bar{m}_x \bar{m}_y \bar{n}_x \bar{n}_y}(\mathbf{k})$  and  $X_{v_1 a_{v_1}, v_2 a'_{v_2}, \mathbf{p}}^{m_x m_y n_x n_y}(\mathbf{k})$  are orthogonal for  $(v_1 a_{v_1}, v_2 a'_{v_2}, \mathbf{p}) \neq (\bar{v}_1 \bar{a}_{\bar{v}_1}, \bar{v}_2 \bar{a}'_{\bar{v}_2}, \bar{\mathbf{p}})$ . However,



for the same  $(v_1 a_{v_1}, v_2 a'_{v_2}, \mathbf{p})$ , we have

$$\begin{aligned}
& \sum_{m_x m_y n_x n_y \in \mathbb{N}} t_{m_x m_y n_x n_y} X_{v_1 a_{v_1}, v_2 a'_{v_2}, \mathbf{p}}^{m_x m_y n_x n_y}(\mathbf{k}) = 0 \\
& \Leftrightarrow \sum_{m_x m_y n_x n_y \in \mathbb{N}} t_{m_x m_y n_x n_y} \delta_{v_Q a_Q, v_1 a_{v_1}} \delta_{v'_{Q'} a'_{Q'}, v_2 a'_{v_2}} (\mathbf{k} - \mathbf{Q})_x^{m_x} (\mathbf{k} - \mathbf{Q})_y^{m_y} \delta_{\mathbf{Q}, \mathbf{Q}' + \mathbf{p}} (\mathbf{k} - \mathbf{Q}')_x^{n_x} (\mathbf{k} - \mathbf{Q}')_y^{n_y} = 0 \\
& \quad \text{for all } \mathbf{k}, \mathbf{Q}, a_Q, \mathbf{Q}', a'_{Q'} \\
& \Leftrightarrow \sum_{m_x m_y n_x n_y \in \mathbb{N}} t_{m_x m_y n_x n_y} q_x^{m_x} q_y^{m_y} (\mathbf{q} - \mathbf{p})_x^{n_x} (\mathbf{q} - \mathbf{p})_y^{n_y} = 0 \text{ for all } \mathbf{q} \in \mathbb{R}^2 \\
& \Leftrightarrow \sum_{m_x m_y n_x n_y \in \mathbb{N}} t_{m_x m_y n_x n_y} Q_x^{m_x} Q_y^{m_y} \sum_{l_x=0}^{n_x} \sum_{l_y=0}^{n_y} Q_x^{n_x-l_x} P_x^{l_x} C_{n_x}^{l_x} Q_y^{n_y-l_y} P_y^{l_y} C_{n_y}^{l_y} = 0 \text{ for all } \mathbf{q} \in \mathbb{R}^2 \\
& \Leftrightarrow \sum_{m_x m_y n_x n_y l_x l_y \in \mathbb{N}} C_{n_x+l_x}^{l_x} (-p_x)^{l_x} C_{n_y+l_y}^{l_y} (-p_y)^{l_y} t_{m_x, m_y, n_x+l_x, n_y+l_y} q_x^{m_x} q_y^{m_y} q_x^{n_x} q_y^{n_y} = 0 \text{ for all } \mathbf{q} \in \mathbb{R}^2 \\
& \Leftrightarrow \sum_{M_x M_y \in \mathbb{N}} \left[ \sum_{0 \leq n_x \leq M_x} \sum_{0 \leq n_y \leq M_y} \sum_{l_x l_y \in \mathbb{N}} C_{n_x+l_x}^{l_x} (-p_x)^{l_x} C_{n_y+l_y}^{l_y} (-p_y)^{l_y} t_{M_x-n_x, M_y-n_y, n_x+l_x, n_y+l_y} \right] q_x^{M_x} q_y^{M_y} = 0 \text{ for all } \mathbf{q} \in \mathbb{R}^2 \\
& \Leftrightarrow \sum_{0 \leq n_x \leq M_x} \sum_{0 \leq n_y \leq M_y} \sum_{l_x l_y \in \mathbb{N}} C_{n_x+l_x}^{l_x} (-p_x)^{l_x} C_{n_y+l_y}^{l_y} (-p_y)^{l_y} t_{M_x-n_x, M_y-n_y, n_x+l_x, n_y+l_y} = 0 \text{ for all } M_x \in \mathbb{N}, M_y \in \mathbb{N},
\end{aligned} \tag{C26}$$

where  $C_m^n$  is the binomial  $m$  choose  $n$ , and we use  $q_x^{M_x} q_y^{M_y}$  are linearly independent for different powers  $M_x$  and  $M_y$  (they are just multipole expansions) for the last step. It means that as long as  $t_{m_x m_y n_x n_y}$  satisfies the last equation, the coefficients are constrained such that there is only one independent parameter among all  $t_{m_x m_y n_x n_y}$ 's for fixed  $m_x + n_x = M_x$  and  $m_y + n_y = M_y$ . In order to avoid this redundancy, we re-wrtie the continuum expression of  $h_{\text{DFT}}(\mathbf{k})$  in Eq. (C24) as

$$\begin{aligned}
[h_{\text{DFT}}(\mathbf{k})]_{Q a_Q, \mathbf{Q}' a'_{Q'}} &= \sum_{m_x, m_y, n_x, n_y \in \mathbb{N}} \sum_{v_1 v_2} \sum_{\mathbf{G}_M} \sum_{a_{v_1} a'_{v_2}} t_{v_1 a_{v_1}, v_2 a'_{v_2}, \mathbf{G}_M}^{m_x m_y n_x n_y} \delta_{v_Q a_Q, v_1 a_{v_1}} \delta_{v'_{Q'} a'_{Q'}, v_2 a'_{v_2}} (\mathbf{k} - \mathbf{Q})_x^{m_x} (\mathbf{k} - \mathbf{Q})_y^{m_y} \\
& \quad \times \delta_{\mathbf{Q}, \mathbf{Q}' + \mathbf{q}_{v_1} - \mathbf{q}_{v_2} + \mathbf{G}_M} (\mathbf{k} - \mathbf{Q}')_x^{n_x} (\mathbf{k} - \mathbf{Q}')_y^{n_y} \\
&= \sum_{m_x, m_y, n_x, n_y \in \mathbb{N}} \sum_{v_1 v_2} \sum_{\mathbf{G}_M} \sum_{a_{v_1} a'_{v_2}} t_{v_1 a_{v_1}, v_2 a'_{v_2}, \mathbf{G}_M}^{m_x m_y n_x n_y} \delta_{v_Q a_Q, v_1 a_{v_1}} \delta_{v'_{Q'} a'_{Q'}, v_2 a'_{v_2}} (\mathbf{k} - \mathbf{Q})_x^{m_x} (\mathbf{k} - \mathbf{Q})_y^{m_y} \\
& \quad \times \delta_{\mathbf{Q}, \mathbf{Q}' + \mathbf{q}_{v_1} - \mathbf{q}_{v_2} + \mathbf{G}_M} (\mathbf{k} - \mathbf{Q} - (\mathbf{q}_{v_1} - \mathbf{q}_{v_2} + \mathbf{G}_M))_x^{n_x} (\mathbf{k} - \mathbf{Q} - (\mathbf{q}_{v_1} - \mathbf{q}_{v_2} + \mathbf{G}_M))_y^{n_y} \\
&= \sum_{M_x, M_y \in \mathbb{N}} \sum_{v_1 v_2} \sum_{\mathbf{G}_M} \sum_{a_{v_1} a'_{v_2}} r_{v_1 a_{v_1}, v_2 a'_{v_2}, \mathbf{G}_M}^{M_x M_y} \delta_{v_Q a_Q, v_1 a_{v_1}} \delta_{v'_{Q'} a'_{Q'}, v_2 a'_{v_2}} (\mathbf{k} - \mathbf{Q})_x^{M_x} (\mathbf{k} - \mathbf{Q})_y^{M_y} \\
& \quad \times \delta_{\mathbf{Q}, \mathbf{Q}' + \mathbf{q}_{v_1} - \mathbf{q}_{v_2} + \mathbf{G}_M} \\
&= \sum_{M_x, M_y \in \mathbb{N}} \sum_{v_1 v_2} \sum_{\mathbf{G}_M} \sum_{a_{v_1} a'_{v_2}} r_{v_1 a_{v_1}, v_2 a'_{v_2}, \mathbf{G}_M}^{M_x M_y} [Y_{v_1 a_{v_1}, v_2 a'_{v_2}, \mathbf{q}_{v_1} - \mathbf{q}_{v_2} + \mathbf{G}_M}^{M_x M_y}(\mathbf{k})]_{Q a_Q, \mathbf{Q}' a'_{Q'}} ,
\end{aligned} \tag{C27}$$

where

$$r_{v_1 a_{v_1}, v_2 a'_{v_2}, \mathbf{G}_M}^{M_x M_y} = \sum_{0 \leq n_x \leq M_x} \sum_{0 \leq n_y \leq M_y} \sum_{l_x l_y \in \mathbb{N}} C_{n_x+l_x}^{l_x} (-p_x)^{l_x} C_{n_y+l_y}^{l_y} (-p_y)^{l_y} t_{v_1 a_{v_1}, v_2 a'_{v_2}, \mathbf{G}_M}^{M_x-n_x, M_y-n_y, n_x+l_x, n_y+l_y} \Big|_{\mathbf{p}=\mathbf{q}_{v_1} - \mathbf{q}_{v_2} + \mathbf{G}_M}, \tag{C28}$$

is derived in the same way as Eq. (C26), and

$$[Y_{v_1 a_{v_1}, v_2 a'_{v_2}, \mathbf{p}}^{M_x M_y}(\mathbf{k})]_{Q a_Q, \mathbf{Q}' a'_{Q'}} = \delta_{v_Q a_Q, v_1 a_{v_1}} \delta_{v'_{Q'} a'_{Q'}, v_2 a'_{v_2}} (\mathbf{k} - \mathbf{Q})_x^{M_x} (\mathbf{k} - \mathbf{Q})_y^{M_y} \delta_{\mathbf{Q}, \mathbf{Q}' + \mathbf{p}}, \tag{C29}$$

Our goal is therefore to determine  $r_{v_1 a_{v_1}, v_2 a'_{v_2}, \mathbf{G}_M}^{M_x M_y}$ 's, which are the *linearly independent* values of  $t_{v_1 a_{v_1}, v_2 a'_{v_2}, \mathbf{G}_M}^{m_x m_y n_x n_y}$ 's.

We now show that it is possible to determine the coefficients just from  $h_{\text{DFT}}(\mathbf{k}_0)$  at a fixed  $\mathbf{k}_0$ . The cornerstone of this is the fact that the set of  $Y_{v_1 a_{v_1}, v_2 a'_{v_2}, \mathbf{p}}^{M_x M_y}(\mathbf{k}_0)$ 's are linearly independent. First,  $Y_{v_1 a_{v_1}, v_2 a'_{v_2}, \mathbf{p}}^{M_x M_y}(\mathbf{k}_0)$  are orthogonal for different  $(v_1 a_{v_1}, v_2 a'_{v_2}, \mathbf{G}_M)$  just as Eq. (C25). Second, for the same  $(v_1 a_{v_1}, v_2 a'_{v_2}, \mathbf{G}_M)$ , we have

$$\begin{aligned}
& \sum_{M_x M_y \in \mathbb{N}} r_{M_x M_y} Y_{v_1 a_{v_1}, v_2 a'_{v_2}, \mathbf{p}}^{M_x M_y}(\mathbf{k}_0) = 0 \\
& \Leftrightarrow \sum_{M_x M_y \in \mathbb{N}} r_{M_x M_y} \delta_{v_Q a_Q, v_1 a_{v_1}} \delta_{v'_{Q'} a'_{Q'}, v_2 a'_{v_2}} (\mathbf{k}_0 - \mathbf{Q})_x^{M_x} (\mathbf{k}_0 - \mathbf{Q})_y^{M_y} \delta_{\mathbf{Q}, \mathbf{Q}' + \mathbf{p}} = 0 \text{ for all } \mathbf{k}, \mathbf{Q}, a_Q, \mathbf{Q}', a'_{Q'} \\
& \Leftrightarrow \sum_{M_x M_y \in \mathbb{N}} r_{M_x M_y} (k_{0,x} - Q_x)^{M_x} (k_{0,y} - Q_y)^{M_y} = 0 \text{ for all } \mathbf{Q} \in \{\mathbf{G}_M\} + \mathbf{q}_{v_1} \\
& \Leftrightarrow r_{M_x M_y} = 0 \text{ for all } M_x M_y \in \mathbb{N},
\end{aligned} \tag{C30}$$

where the last step can be proven by induction as follows.

$$\sum_{M_x=0,1,\dots,L_x} \sum_{M_y=0,1,\dots,L_y} r_{M_x M_y} (k_{0,x} - Q_x)^{M_x} (k_{0,y} - Q_y)^{M_y} \text{ for all } \mathbf{Q} \in \{\mathbf{G}_M\} + \mathbf{q}_{v_1} \Leftrightarrow r_{M_x M_y} = 0 \text{ for all } M_x M_y \in \mathbb{N}, \tag{C31}$$

trivially holds for  $L_x = L_y = 0$ . If Eq. (C31) holds for certain  $(L_x, L_y)$ , then it should also hold for  $(L_x + 1, L_y)$  since the extra  $(k_{0,x} - Q_x)^{L_x+1} (k_{0,y} - Q_y)^{L_y}$  can have larger absolute values than the other terms (which has less  $Q_x$  powers) by as much as we want, since we can always choose  $(k_{0,y} - Q_y) \neq 0$  and increase  $Q_x$ . Similarly, if Eq. (C31) holds for certain  $(L_x, L_y)$ , then it should also hold for  $(L_x, L_y + 1)$ . Therefore, the last step of Eq. (C30) is proven. As a result, we have shown that the set of  $Y_{v_1 a_{v_1}, v_2 a'_{v_2}, \mathbf{p}}^{M_x M_y}(\mathbf{k}_0)$ 's are linearly independent for a fixed  $\mathbf{k}_0$ , allowing us to determine  $r_{v_1 a_{v_1}, v_2 a'_{v_2}, \mathbf{G}_M}^{M_x M_y}$  from  $h_{\text{DFT}}(\mathbf{k}_0)$  in principle.

The above discussion assumes an infinite lattice of  $\mathbf{G}_M$ . In practice, we only have finite  $\mathbf{G}_M$ 's, and yet we only need to include a finite number of  $M_x$  and  $M_y$  to capture the low-energy physics. Therefore, we are still allowed to determine the meaningful  $r_{v_1 a_{v_1}, v_2 a'_{v_2}, \mathbf{G}_M}^{M_x M_y}$  from  $h_{\text{DFT}}(\mathbf{k}_0)$ , as long as the needed  $M_x$  and  $M_y$  is not too large compared to the cutoff of  $\mathbf{G}_M$ . Specifically, we choose a range of  $(M_x, M_y, v_1 a_{v_1}, v_2 a'_{v_2}, \mathbf{G}_M)$  of interest, which give us a set of  $Y_{v_1 a_{v_1}, v_2 a'_{v_2}, \mathbf{q}_{v_1} - \mathbf{q}_{v_2} + \mathbf{G}_M}^{M_x M_y}(\mathbf{k}_0)$ . We need to orthonormalize those  $Y_{v_1 a_{v_1}, v_2 a'_{v_2}, \mathbf{q}_{v_1} - \mathbf{q}_{v_2} + \mathbf{G}_M}^{M_x M_y}(\mathbf{k}_0)$ 's, e.g., by Gram-Schmidt process, and obtain a set of new  $\tilde{Y}_{v_1 a_{v_1}, v_2 a'_{v_2}, \mathbf{p}}^{M_x M_y}(\mathbf{k}_0)$  that are related to  $Y_{v_1 a_{v_1}, v_2 a'_{v_2}, \mathbf{q}_{v_1} - \mathbf{q}_{v_2} + \mathbf{G}_M}^{M_x M_y}(\mathbf{k}_0)$  by

$$\tilde{Y}_{v_1 a_{v_1}, v_2 a'_{v_2}, \mathbf{q}_{v_1} - \mathbf{q}_{v_2} + \mathbf{G}_M}^{M_x M_y}(\mathbf{k}_0) = \sum_{\tilde{M}_x \tilde{M}_y} Y_{v_1 a_{v_1}, v_2 a'_{v_2}, \mathbf{q}_{v_1} - \mathbf{q}_{v_2} + \mathbf{G}_M}^{\tilde{M}_x \tilde{M}_y}(\mathbf{k}_0) z_{\tilde{M}_x \tilde{M}_y, M_x M_y}^{v_1 a_{v_1}, v_2 a'_{v_2}, \mathbf{G}_M}, \tag{C32}$$

and that satisfy

$$\text{Tr} \left\{ \left[ \tilde{Y}_{v_1 a_{v_1}, v_2 a'_{v_2}, \mathbf{q}_{v_1} - \mathbf{q}_{v_2} + \mathbf{G}_M}^{M_x M_y}(\mathbf{k}_0) \right]^\dagger \tilde{Y}_{v_1 a_{v_1}, v_2 a'_{v_2}, \mathbf{q}_{v_1} - \mathbf{q}_{v_2} + \mathbf{G}_M}^{M'_x M'_y}(\mathbf{k}_0) \right\} = \delta_{M_x M_y, M'_x M'_y}. \tag{C33}$$

Here we don't need to orthonormalize  $(v_1 a_{v_1}, v_2 a'_{v_2}, \mathbf{p})$  indices because they are already orthogonal. Then, we can obtain

$$\tilde{r}_{v_1 a_{v_1}, v_2 a'_{v_2}, \mathbf{p}}^{M_x M_y} = \text{Tr} \{ \tilde{Y}_{v_1 a_{v_1}, v_2 a'_{v_2}, \mathbf{q}_{v_1} - \mathbf{q}_{v_2} + \mathbf{G}_M}^{M_x M_y}(\mathbf{k}_0) h_{\text{DFT}}(\mathbf{k}_0) \}, \tag{C34}$$

resulting in

$$r_{v_1 a_{v_1}, v_2 a'_{v_2}, \mathbf{p}}^{M_x M_y} = \sum_{\tilde{M}_x \tilde{M}_y} z_{M_x M_y, \tilde{M}_x \tilde{M}_y}^{v_1 a_{v_1}, v_2 a'_{v_2}, \mathbf{G}_M} \tilde{r}_{v_1 a_{v_1}, v_2 a'_{v_2}, \mathbf{q}_{v_1} - \mathbf{q}_{v_2} + \mathbf{G}_M}^{\tilde{M}_x \tilde{M}_y}. \tag{C35}$$

With  $r_{v_1 a_{v_1}, v_2 a'_{v_2}, \mathbf{G}_M}^{M_x M_y}$ , we have a continuum model

$$h_{\text{cont}}(\mathbf{k}) = \sum_{M_x, M_y} \sum_{v_1 v_2} \sum_{\mathbf{G}_M} \sum_{a_{v_1} a'_{v_2}} r_{v_1 a_{v_1}, v_2 a'_{v_2}, \mathbf{G}_M}^{M_x M_y} Y_{v_1 a_{v_1}, v_2 a'_{v_2}, \mathbf{q}_{v_1} - \mathbf{q}_{v_2} + \mathbf{G}_M}^{M_x M_y}(\mathbf{k}), \tag{C36}$$

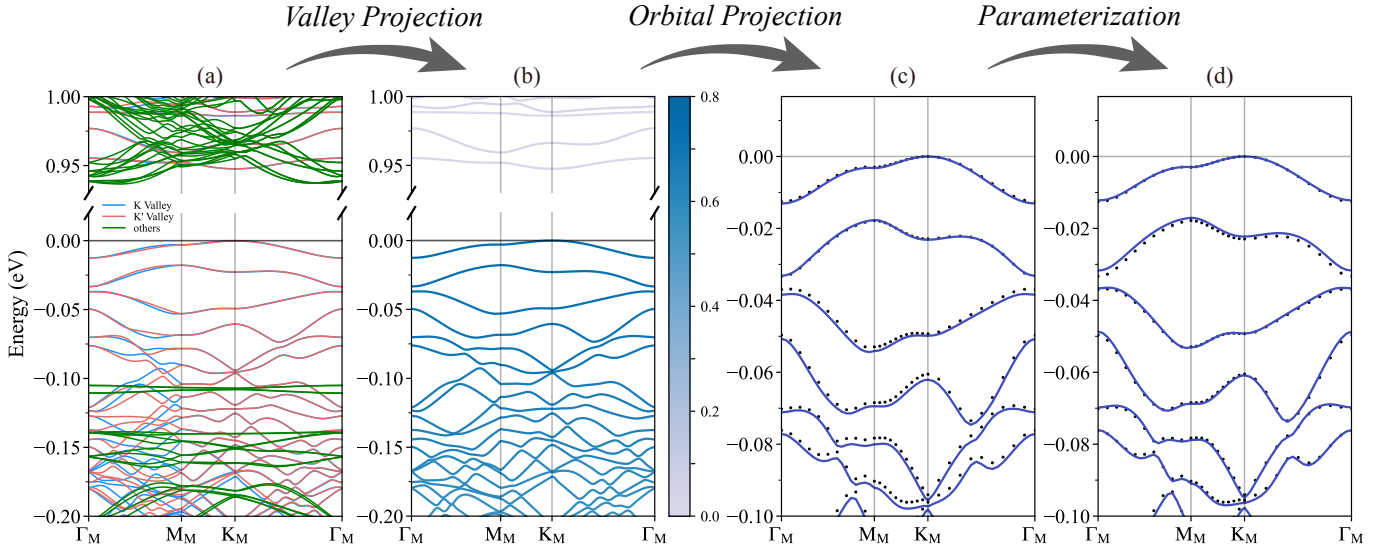


FIG. 9. **DFT to Full Model.** (a) Band structure of the full Hamiltonian for 3.89° tMoTe<sub>2</sub> computed using OpenMX. Blue lines denote the K valley, red lines represent the K' valley bands, and green lines correspond to the bands of other valleys, including the  $\Gamma$  valley. (b) Valley-projected band structure obtained via the Truncated Atomic Plane Wave (TAPW) method, exclusively displaying the K valley. The color intensity indicates the contribution of Mo's  $d_{xy}$  and  $d_{x^2+y^2}$  orbitals to each band. (c) Orbital projection focusing solely on Mo's  $d_{xy}$  and  $d_{x^2+y^2}$  orbitals. (d) Band structure derived from the full continuum model. In subfigures (c) and (d), the black dotted lines correspond to the DFT results for comparison.

where  $(M_x, M_y, v_1 a_{v_1}, v_2 a'_{v_2}, \mathbf{G}_M)$  is summed only over a range of interested values in contrast to all values in Eq. (C27). We may speed up the determination of  $r_{v_1 a_{v_1}, v_2 a'_{v_2}, \mathbf{G}_M}^{M_x M_y}$  by summarizing  $Y_{v_1 a_{v_1}, v_2 a'_{v_2}, \mathbf{q}_{v_1} - \mathbf{q}_{v_2} + \mathbf{G}_M}^{M_x M_y}(\mathbf{k})$  based on hermiticity and symmetries. We emphasize that the construction of Eq. (C36) requires no fitting, and thus the more terms (labelled by  $(M_x, M_y, v_1 a_{v_1}, v_2 a'_{v_2}, \mathbf{G}_M)$ ) included, the more accurate model we have since there is no overfitting issue here. In practice, we can include a large number of terms to keep Eq. (C36) very precise, which can be easily used in numerical calculations. Of course, one can use more than one  $\mathbf{k}_0$  point in the procedure—using a direct sum of  $h_{\text{DFT}}(\mathbf{k})$  at more than one  $\mathbf{k}_0$  in the replacement of  $h_{\text{DFT}}(\mathbf{k}_0)$ .

However, for many analytical applications, it may be desirable to retain only a limited set of  $\mathbf{Q}$  points that capture the essential low-energy behavior while ignoring higher-energy contributions. This can be achieved by projecting out the outer-shell  $\mathbf{Q}$  points from  $h_{\text{DFT}}(\mathbf{k})$  in Eq. (C17) by perturbation theory. The resulting reduced Hamiltonian  $h_{\text{DFT}}^{\text{eff}}(\mathbf{k})$ , lives on a much smaller  $\mathbf{Q}$  points. By applying the same construction procedure to  $h_{\text{DFT}}^{\text{reduced}}(\mathbf{k})$ , we derive an effective continuum model Hamiltonian  $h_{\text{cont}}^{\text{reduced}}(\mathbf{k})$  that captures the low-energy physics (it will be only precise for much fewer bands) with a much smaller number of terms. This simplified model enables analytical exploration of low-energy behaviors while retaining fidelity to the original DFT calculations.

In the following section, we apply this general method to AA-stacked tMoTe<sub>2</sub>, demonstrating the versatility and accuracy of this continuum model construction method.

#### Appendix D: Constructing continuum model of AA-stacked tMoTe<sub>2</sub> and tWSe<sub>2</sub>

In this section, we apply the general method introduced in App. [C] to construct continuum models for AA-stacked tMoTe<sub>2</sub> and tWSe<sub>2</sub> in the K valley. Due to the similarities between tMoTe<sub>2</sub> and tWSe<sub>2</sub>, we will primarily discuss the procedure using tMoTe<sub>2</sub> as an example while presenting results applicable to both materials. In AA-stacked bilayer tMoTe<sub>2</sub>, the low-energy moiré bands originate from the highest valence bands around the  $K$  and  $-K$  valleys in both layers. We focus on the continuum model of the  $K$  valley in this section because the  $\pm K$  valleys are related by time-reversal symmetry, and the  $\Gamma$ -valley bands lie well below the charge neutrality point.

We construct two types of continuum models: the first is based on the full  $\mathbf{Q}$  lattice used in the DFT Hamiltonian, and the second is a simplified model on a reduced  $\mathbf{Q}$  lattice with fewer terms.

## 1. Procedure for Constructing the Continuum Model

Below, we outline the steps for constructing a continuum model from  $H_{\text{DFT}}$  on both the full and reduced  $\mathbf{Q}$  lattices.

### 1. Obtain an Effective Hamiltonian in the Low-Energy Subspace Using Second-order Perturbation

For the  $K$  valley of  $t\text{MoTe}_2$ , the sub-valley index is equivalent to the layer index, as the two layers possess distinct  $K_l$ . Consequently, the basis of the DFT Hamiltonian,  $c_{\mathbf{k}+\mathbf{K}_0, \mathbf{Q}, \alpha \mathbf{Q}}^\dagger \equiv c_{\mathbf{k}+\mathbf{K}_0+\mathbf{q}_{v\mathbf{Q}}-\mathbf{Q}, \alpha \mathbf{Q}}^\dagger$ , simplifies to  $c_{\mathbf{k}+\mathbf{K}_l-\mathbf{Q}, \alpha}^\dagger$ , where  $l\mathbf{Q}$  is denoted as  $l$  for simplicity. The full continuum model basis is thus represented as  $\psi_{\mathbf{k}, \mathbf{Q}, a}^\dagger$ , where  $\alpha$  encompasses the 71 orbitals (Mo- $s3p2d2$  and Te- $s3p2d2f1$ ) with spin- $\uparrow$  in one monolayer unit cell. However, we are interested only in the low-energy states closest to the Fermi energy at each  $\mathbf{Q}$  site that form the low-energy moiré bands. We denote the number of  $\mathbf{Q}$  sites as  $N_{\mathbf{Q}}$ .

To isolate these states, we diagonalize each  $\mathbf{Q}$ -block of  $H_{\text{DFT}}$  and identify the low-energy states, labeled as  $U_{\text{low}}^{\mathbf{k}, \mathbf{Q}}$ , which are predominantly composed of  $d_{x^2+y^2, \uparrow} + id_{xy, \uparrow}$  orbitals from Mo atoms. As shown in Fig. 10, for each  $\mathbf{k}$  and  $\mathbf{Q}$ , there is usually one eigenvalue  $\lambda_n^{\mathbf{k}, \mathbf{Q}}$  near the Fermi level. We denote the corresponding low-energy eigenvector as  $U_{\text{low}}^{\mathbf{k}, \mathbf{Q}}$ . With the remaining branches approximately about 1 eV away from the Fermi energy, we focus solely on the low-energy branch for constructing the low-energy basis:

$$\psi_{\mathbf{k}, \mathbf{Q}}^\dagger = \sum_{\alpha \mathbf{Q}} c_{\mathbf{k}+\mathbf{K}_l-\mathbf{Q}, \alpha \mathbf{Q}}^\dagger \left[ U_{\text{low}}^{\mathbf{k}, \mathbf{Q}} \right]_{\alpha \mathbf{Q}}, \quad (\text{D1})$$

The remaining high-energy states are labeled as  $U_{\text{high}}^{\mathbf{k}, \mathbf{Q}}$ . Given that the phases of  $U^{\mathbf{k}, \mathbf{Q}}$  vary randomly across the  $\mathbf{Q}$  sites, we fix the gauge by ensuring the  $d_{x^2+y^2, \uparrow}$  component of  $U_{\text{low}}^{\mathbf{k}, \mathbf{Q}}$  is real and non-positive.

We then partition the Hilbert space into low-energy and high-energy subspaces with corresponding projection matrices  $U_0(\mathbf{k})$  and  $U_1(\mathbf{k})$ :

$$\begin{aligned} U_0(\mathbf{k}) &= \bigoplus_{\mathbf{Q}} U_{\text{low}}^{\mathbf{k}, \mathbf{Q}}, \\ U_1(\mathbf{k}) &= \bigoplus_{\mathbf{Q}} U_{\text{high}}^{\mathbf{k}, \mathbf{Q}}. \end{aligned} \quad (\text{D2})$$

Using  $U(\mathbf{k}) = (U_0(\mathbf{k}), U_1(\mathbf{k}))$ , we transform the DFT Hamiltonian and write it in blocks of four submatrices,

$$\begin{aligned} U^\dagger(\mathbf{k}) H_{\text{DFT}}(\mathbf{k}) U(\mathbf{k}) &= \begin{pmatrix} U_0^\dagger(\mathbf{k}) H_{\text{DFT}}(\mathbf{k}) U_0(\mathbf{k}) & U_0^\dagger(\mathbf{k}) H_{\text{DFT}}(\mathbf{k}) U_1(\mathbf{k}) \\ U_1^\dagger(\mathbf{k}) H_{\text{DFT}}(\mathbf{k}) U_0(\mathbf{k}) & U_1^\dagger(\mathbf{k}) H_{\text{DFT}}(\mathbf{k}) U_1(\mathbf{k}) \end{pmatrix} \\ &= \begin{pmatrix} h_{00}(\mathbf{k}) & h_{01}(\mathbf{k}) \\ h_{10}(\mathbf{k}) & h_{11}(\mathbf{k}) \end{pmatrix}, \end{aligned} \quad (\text{D3})$$

and the Schrödinger equation becomes

$$\begin{pmatrix} h_{00}(\mathbf{k}) & h_{01}(\mathbf{k}) \\ h_{10}(\mathbf{k}) & h_{11}(\mathbf{k}) \end{pmatrix} \begin{pmatrix} \Psi^L(\mathbf{k}) \\ \Psi^H(\mathbf{k}) \end{pmatrix} = \varepsilon \begin{pmatrix} \Psi^L(\mathbf{k}) \\ \Psi^H(\mathbf{k}) \end{pmatrix}. \quad (\text{D4})$$

This matrix equation segregates the eigenvector  $\Psi(\mathbf{k})$  into low-energy  $\Psi^L(\mathbf{k})$  and high-energy  $\Psi^H(\mathbf{k})$  components. The corresponding matrix equation for  $\Psi(\mathbf{k})$  thus separates into two coupled equations for the low-energy and high-energy subspaces:

$$h_{00}(\mathbf{k}) \Psi^L(\mathbf{k}) + h_{01}(\mathbf{k}) \Psi^H(\mathbf{k}) = \varepsilon \Psi^L(\mathbf{k}), \quad (\text{D5})$$

$$h_{10}(\mathbf{k}) \Psi^L(\mathbf{k}) + h_{11}(\mathbf{k}) \Psi^H(\mathbf{k}) = \varepsilon \Psi^H(\mathbf{k}). \quad (\text{D6})$$

We focus on solving  $\Psi^H(\mathbf{k})$  from the high-energy equation Eq. (D6) and substituting it into the low-energy equation Eq. (D5) to derive an effective Hamiltonian for the low-energy subspace:

$$\left[ h_{00}(\mathbf{k}) + h_{01}(\mathbf{k}) \frac{1}{\varepsilon - h_{11}(\mathbf{k})} h_{10}(\mathbf{k}) \right] \Psi^L(\mathbf{k}) = \varepsilon \Psi^L(\mathbf{k}) \quad (\text{D7})$$

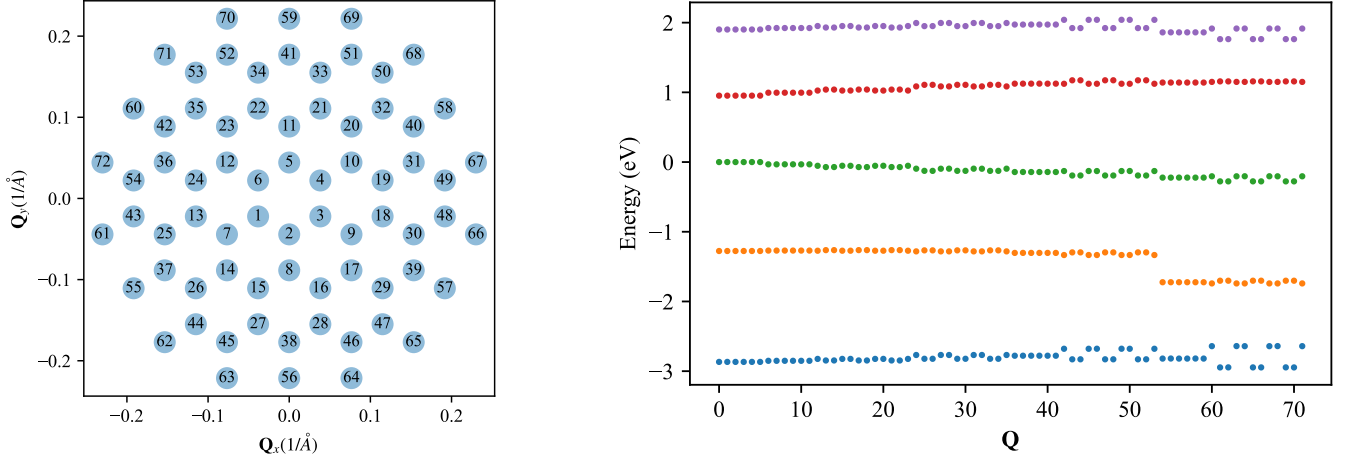


FIG. 10. **Visualization of the  $Q$ -lattice and its corresponding energy spectrum for the  $2.13^\circ$   $t\text{MoTe}_2$ .** (a) The  $Q$ -lattice chosen for the full model at  $2.13^\circ$ . The lattice is selected up to the 8th harmonic, with each number representing a specific  $Q$ -site. (b) Eigenvalues of each  $A \times A$  diagonal block of  $H_{\text{DFT}}(\mathbf{k}_0)$ . The horizontal axis represents the  $Q$ -label index, corresponding to the numbered indices shown in panel (a). The vertical axis shows the energy spectrum obtained by diagonalizing the  $Q$ -blocks from  $D_Q(\mathbf{k}_0)$ . Here,  $\mathbf{k}_0$  is chosen at the  $\Gamma_M$  point in the moiré Brillouin zone. We focus on the low-energy states near the Fermi level.

Thus, we define the effective low-energy Hamiltonian as:

$$h_{\text{DFT}}(\mathbf{k}, \varepsilon) = h_{00}(\mathbf{k}) + h_{01}(\mathbf{k}) \frac{1}{\varepsilon - h_{11}(\mathbf{k})} h_{10}(\mathbf{k}) . \quad (\text{D8})$$

To make this Hamiltonian independent of energy, we approximate  $\varepsilon$  by the mean eigenvalue  $\bar{\lambda}(\mathbf{k})$  of  $h_{00}(\mathbf{k})$ . Using the basis transformation Eq. (D1), we express the low-energy effective Hamiltonian in terms of this basis as:

$$H_{\text{DFT}}^{\text{low-energy}} = \sum_{\mathbf{k}} \sum_{QQ'} \psi_{\mathbf{k},Q}^\dagger h_{\text{DFT}}(\mathbf{k}) \psi_{\mathbf{k},Q'} . \quad (\text{D9})$$

This Hamiltonian  $H_{\text{DFT}}^{\text{low-energy}}$  now provides a description of the low-energy subspace that is computationally manageable and captures the key physical characteristics necessary for analyzing the moiré system.

## 2. Construct an Effective Hamiltonian on a Reduced $Q$ Sublattice Using Second-order Perturbation

We can already construct the continuum model for  $H_{\text{DFT}}^{\text{low-energy}}$ . To construct a smaller model, we may want to further reduce the dimension of  $h_{\text{DFT}}(\mathbf{k})$  and simplify the analytical model, we divide the  $Q$  lattice into two parts:  $Q_{\text{inside}}$ , which represents the region we focus on, and  $Q_{\text{outside}}$ . Using Second-order Perturbation again, we project  $h_{\text{DFT}}(\mathbf{k})$  onto the smaller sublattice, i.e.,  $Q_{\text{inside}}$ .

We represent  $h_{\text{DFT}}(\mathbf{k})$  in terms of four submatrices arranged in blocks

$$h_{\text{DFT}}(\mathbf{k}) = \begin{pmatrix} h'_{00}(\mathbf{k}) & h'_{01}(\mathbf{k}) \\ h'_{10}(\mathbf{k}) & h'_{11}(\mathbf{k}) \end{pmatrix} , \quad (\text{D10})$$

where  $h'_{00}(\mathbf{k})$  and  $h'_{11}(\mathbf{k})$  are defined on the  $Q_{\text{inside}}$  and  $Q_{\text{outside}}$  lattice, respectively. Using a similar approach as step 1, we derive the effective Hamiltonian for the smaller  $Q$  sublattice:

$$h_{\text{DFT}}^{\text{reduced}}(\mathbf{k}) = h'_{00}(\mathbf{k}) + h'_{01}(\mathbf{k}) \frac{1}{\varepsilon_{\text{out}} - h'_{11}(\mathbf{k})} h'_{10}(\mathbf{k}) , \quad (\text{D11})$$

with  $\varepsilon_{\text{out}}$  chosen as the maximum eigenvalue of  $h'_{00}(\mathbf{k})$  as we only want to focus on the top few energy bands near the Fermi level. This setup provides a simplified yet effective Hamiltonian that governs the low-energy dynamics within the selected sublattice:

$$H_{\text{DFT}}^{\text{reduced}} = \sum_{\mathbf{k}} \sum_{QQ' \in Q_{\text{inside}}} \psi_{\mathbf{k},Q}^\dagger h_{\text{DFT}}^{\text{reduced}}(\mathbf{k}) \psi_{\mathbf{k},Q'} . \quad (\text{D12})$$

### 3. Calculate the Coefficients of Linearly Independent Terms in the General Continuum Model

We assume that a general continuum model can effectively describe the Hamiltonian in the low-energy subspace, whether  $H_{\text{DFT}}^{\text{low-energy}}$  or  $H_{\text{DFT}}^{\text{reduced}}$ . We first express the continuum model in real space:

$$\begin{aligned}
H_{\text{cont}} &= \sum_{m_x, m_y, n_x, n_y \in \mathbb{N}} \sum_{l'} \int d^2r \left( i^m \partial_x^{m_x} \partial_y^{m_y} \psi_{\mathbf{r}, \mathbf{K}_l}^\dagger \right) \tilde{t}_{l, l'}^{m_x m_y n_x n_y}(\mathbf{r}) (-i)^n \partial_x^{n_x} \partial_y^{n_y} \psi_{\mathbf{r}, \mathbf{K}_{l'}} \\
&= \sum_{M_x, M_y \in \mathbb{N}} \sum_{l'} \int d^2r \left( i^m \partial_x^{M_x} \partial_y^{M_y} \psi_{\mathbf{r}, \mathbf{K}_l}^\dagger \right) t_{l, l'}^{M_x M_y}(\mathbf{r}) \psi_{\mathbf{r}, \mathbf{K}_{l'}} \\
&= \sum_{M_z, M_{z^*} \in \mathbb{N}} \sum_{l'} \int d^2r \left( i^m \partial_z^{M_z} \partial_{z^*}^{M_{z^*}} \psi_{\mathbf{r}, \mathbf{K}_l}^\dagger \right) t_{l, l'}^{M_z M_{z^*}}(\mathbf{r}) \psi_{\mathbf{r}, \mathbf{K}_{l'}} ,
\end{aligned} \tag{D13}$$

where  $M_x, M_y$  are indices of the partial derivatives in real space.  $\psi_{\mathbf{r}, \mathbf{K}_l}^\dagger$  and  $t_{\mathbf{K}_l, \mathbf{K}_{l'}}^{M_z M_{z^*}}$  is simplified as  $\psi_{\mathbf{k}, \mathbf{K}_l}^\dagger$  and  $t_{l, l'}^{M_z M_{z^*}}$  as discussed in App. [C]. We use integration by parts and  $M_{x,y} = m_{x,y} + n_{x,y}$  in the second line to make sure these terms are linearly independent as proved by Eq. (C25)-Eq. (C27). Different from Eq. (C19), in the third line, we replace  $\partial_{x,y}$  with  $\partial_{z,z^*}$  defined by

$$\partial_z = \partial_x + i\partial_y, \quad \partial_{z^*} = \partial_x - i\partial_y. \tag{D14}$$

as  $t\text{MoTe}_2$  has  $C_{3z}$  symmetry. According to Eq. (C2) and Eq. (C20) required by moiré translation symmetry, the Fourier transformation of  $\psi_{\mathbf{r}, \mathbf{K}_l}(\mathbf{r})$  and  $t_{l, l'}^{M_z M_{z^*}}(\mathbf{r})$  reads,

$$\begin{aligned}
\psi_{\mathbf{r}, \mathbf{K}_l}^\dagger(\mathbf{r}) &= \sum_{\mathbf{k}, \mathbf{G}_M} e^{-i(\mathbf{k} - \mathbf{G}_M - \mathbf{q}_l) \cdot \mathbf{r}} \psi_{\mathbf{k}, \mathbf{G}_M + \mathbf{q}_l}^\dagger, \\
t_{l, l'}^{M_z M_{z^*}}(\mathbf{r}) &= \sum_{\mathbf{G}_M} e^{-i(\mathbf{K}_l - \mathbf{K}_{l'} + \mathbf{G}_M) \cdot \mathbf{r}} t_{l, l', \mathbf{K}_l - \mathbf{K}_{l'} + \mathbf{G}_M}^{M_z M_{z^*}}.
\end{aligned} \tag{D15}$$

Thus, we can obtain the  $H_{\text{cont}}$  in the momentum space,

$$\begin{aligned}
H_{\text{cont}} &= \sum_{\mathbf{k}} \sum_{\mathbf{Q}, \mathbf{Q}'} \psi_{\mathbf{k}, \mathbf{Q}}^\dagger \psi_{\mathbf{k}, \mathbf{Q}'} h_{\text{cont}}^{\mathbf{Q}, \mathbf{Q}'}(\mathbf{k}) \\
h_{\text{cont}}^{\mathbf{Q}, \mathbf{Q}'}(\mathbf{k}) &= \sum_{M_z, M_{z^*} \in \mathbb{N}} \sum_{l'} \sum_{\mathbf{G}_M} t_{l, l', \mathbf{G}_M}^{M_z M_{z^*}} \left[ Y_{l, l', \mathbf{K}_l - \mathbf{K}_{l'} + \mathbf{G}_M}^{M_z M_{z^*}}(\mathbf{k}) \right]_{\mathbf{Q}, \mathbf{Q}'},
\end{aligned} \tag{D16}$$

where

$$\left[ Y_{l, l', \mathbf{p}}^{M_z M_{z^*}}(\mathbf{k}) \right]_{\mathbf{Q}, \mathbf{Q}'} = \delta_{l_{\mathbf{Q}}, l} \delta_{l_{\mathbf{Q}'}, l'} (\mathbf{k} - \mathbf{Q})_z^{M_z} (\mathbf{k} - \mathbf{Q})_{z^*}^{M_{z^*}} \delta_{\mathbf{Q}, \mathbf{Q}' + \mathbf{p}}, \tag{D17}$$

where  $(\mathbf{k} - \mathbf{Q})_z^{M_z} = [(\mathbf{k} - \mathbf{Q})_x + i(\mathbf{k} - \mathbf{Q})_y]^{M_z}$ ,  $(\mathbf{k} - \mathbf{Q})_{z^*}^{M_{z^*}} = [(\mathbf{k} - \mathbf{Q})_x - i(\mathbf{k} - \mathbf{Q})_y]^{M_{z^*}}$ ,  $\mathbf{p} = \mathbf{K}_l - \mathbf{K}_{l'} + \mathbf{G}_M$ , and  $l_{\mathbf{Q}} = b$  if  $\mathbf{Q} \in$  bottom layer; otherwise,  $l_{\mathbf{Q}} = t$ . Compared with Eq. (C36), and following the analogous derivations analogous to Eq. (C32)-Eq. (C35), we can obtain:

$$r_{l, l', \mathbf{G}_M}^{M_x M_y} = \sum_{M_z, M_{z^*} \in \mathbb{N}} \sum_{i=0}^{M_z} \sum_{j=0}^{M_{z^*}} t_{l, l', \mathbf{G}_M}^{M_z M_{z^*}} i^{M_z + M_{z^*} - i - j} C_{M_z}^i C_{M_{z^*}}^j \frac{Y_{l, l', \mathbf{p}}^{i+j, M_z + M_{z^*} - i - j}(\mathbf{k}_0) [Y_{l, l', \mathbf{p}}^{M_x M_y}(\mathbf{k}_0)]^\dagger}{\text{Tr}\{Y_{l, l', \mathbf{p}}^{M_x M_y}(\mathbf{k}_0) [Y_{l, l', \mathbf{p}}^{M_x M_y}(\mathbf{k}_0)]^\dagger\}}, \tag{D18}$$

the coefficients  $t_{l, l', \mathbf{G}_M}^{M_z M_{z^*}}$  are determined by orthogonalizing the terms in  $h_{\text{cont}}(\mathbf{k}_0)$  at a fixed reference  $\mathbf{k}_0$ , typically chosen at the  $\Gamma_M$  point in the moiré Brillouin zone.

To calculate these coefficients, we perform the Gram-Schmidt orthogonalization process and extract the coefficients from  $h_{\text{DFT}}(\mathbf{k}_0)$  or  $h_{\text{DFT}}^{\text{reduced}}(\mathbf{k}_0)$  using Eq. (C32)-Eq. (C35). Multiple  $\mathbf{k}$ -points can be utilized to enhance accuracy.

In the general continuum model, we categorize the terms as follows:

- **Kinetic Terms:**  $t_{l, l', \mathbf{G}_M}^{M_z M_{z^*}} |_{l=l', \mathbf{G}_M=0} = \hbar^2 / (2m_l^{M_z M_{z^*}})$ .
- **Intralayer Potential Terms:**  $t_{l, l', \mathbf{G}_M}^{M_z M_{z^*}} |_{l=l', \mathbf{G}_M \neq 0} = V_{l, \mathbf{G}_M}^{M_z M_{z^*}}$ .

- **Interlayer Coupling Terms:**  $t_{ll',\mathbf{G}_M}^{M_z M_z^*} |_{l \neq l'} = w_{ll',\mathbf{K}_l - \mathbf{K}_{l'} + \mathbf{G}_M}^{M_z M_z^*}$  .

Thus, the continuum Hamiltonian becomes:

$$h_{cont}(\mathbf{k}) = \sum_{M_z M_z^*} \sum_l \left[ \frac{\hbar^2}{2m_l^{M_z M_z^*}} Y_{ll,0}^{M_z M_z^*}(\mathbf{k}) + \sum_{\mathbf{G}_M} V_{l,\mathbf{G}_M}^{M_z M_z^*} Y_{ll,\mathbf{G}_M}^{M_z M_z^*}(\mathbf{k}) + \sum_{\mathbf{G}_M} w_{\bar{l},\mathbf{p}}^{M_z M_z^*} Y_{\bar{l},\mathbf{p}}^{M_z M_z^*}(\mathbf{k}) \right], \quad (\text{D19})$$

where  $\bar{l}$  denotes the layer opposite to  $l$ . In principle,  $H_{cont}$  is equivalent to the effective Hamiltonian with infinite  $\mathbf{G}_M$  and  $M_z, M_z^*$  terms. However, we introduce cutoffs on these parameters to obtain an analytical model that accurately describes the low-energy moiré bands.

## 2. Symmetry Constraints

The symmetry operations  $C_{3z}$  and  $C_{2y}\mathcal{T}$  enforce additional constraints on the basis functions involved in the Hamiltonian expansion, restricting their form according to the symmetries of the system. For the  $C_{3z}$  and  $C_{2y}\mathcal{T}$  symmetry, we have:

$$D[C_{3z}]_{\mathbf{Q},\mathbf{Q}'} = e^{i\frac{2}{3}\pi} \delta_{\mathbf{Q},C_{3z}\mathbf{Q}'}, D[C_{2y}\mathcal{T}]_{\mathbf{Q},\mathbf{Q}'} = \delta_{\mathbf{Q},\sigma_3\mathbf{Q}'}, \quad (\text{D20})$$

Under the  $C_{3z}$  and  $C_{2y}\mathcal{T}$  operation, the basis functions transform as

$$D[C_{3z}] Y_{ll',\mathbf{p}}^{M_z M_z^*}(C_{3z}^{-1}\mathbf{k}) D[C_{3z}]^{-1} = e^{-i\frac{2}{3}\pi(M_z - M_z^*)} Y_{ll',C_{3z}\mathbf{p}}^{M_z M_z^*}(\mathbf{k}), \quad (\text{D21})$$

$$D[C_{2y}\mathcal{T}] [Y_{ll',\mathbf{p}}^{M_z M_z^*}(\sigma_3\mathbf{k})]^* D[C_{2y}\mathcal{T}]^{-1} = Y_{\bar{l},\sigma_3\mathbf{p}}^{M_z M_z^*}(\mathbf{k}). \quad (\text{D22})$$

The Hermitian conjugate of the basis functions is given by

$$[Y_{ll',\mathbf{p}}^{M_z M_z^*}(\mathbf{k})]^\dagger = Y_{l\bar{l},-\mathbf{p}}^{M_z^* M_z}(\mathbf{k}). \quad (\text{D23})$$

	$C_{3z}$	$C_{2y}\mathcal{T}$	$\dagger$
$m$	$M_z - M_z^* = 0 \pmod{3}$	$m_l^{M_z M_z^*} = m_{\bar{l}}^{M_z M_z^*}$	$m_l^{M_z M_z^*} = m_{\bar{l}}^{M_z^* M_z}$
$V$	$V_{l,\mathbf{G}_M}^{M_z M_z^*} = e^{i\frac{2}{3}\pi(M_z - M_z^*)} V_{l,C_{3z}\mathbf{G}_M}^{M_z M_z^*}$	$V_{l,\mathbf{G}_M}^{M_z M_z^*} = V_{\bar{l},\sigma_3\mathbf{G}_M}^{M_z M_z^*}$	$V_{l,\mathbf{G}_M}^{M_z M_z^*} = V_{l,-\mathbf{G}_M}^{M_z^* M_z}$
$w$	$w_{\bar{l},\mathbf{p}}^{M_z M_z^*} = e^{i\frac{2}{3}\pi(M_z - M_z^*)} w_{ll,C_{3z}\mathbf{p}}^{M_z M_z^*}$	$w_{ll,\mathbf{p}}^{M_z M_z^*} = w_{\bar{l},\sigma_3\mathbf{p}}^{M_z M_z^*}$	$w_{\bar{l},\mathbf{p}}^{M_z M_z^*} = w_{ll,-\mathbf{p}}^{M_z^* M_z}$

TABLE I. Symmetry conditions for the model parameters under  $C_{3z}$  and  $C_{2y}\mathcal{T}$  symmetry operations and Hermitian conjugate.

Harmonic	1	2	3	4	5	6
Intra	$\mathbf{b}_{M_1}$	$\mathbf{b}_{M_1} + \mathbf{b}_{M_2}$	$2\mathbf{b}_{M_1}$	$2\mathbf{b}_{M_1} + \mathbf{b}_{M_2}$	$3\mathbf{b}_{M_1}$	$2\mathbf{b}_{M_1} + 2\mathbf{b}_{M_2}$
Inter	$\mathbf{q}_1$	$-2\mathbf{q}_1$	$\mathbf{q}_1 + \mathbf{b}_{M_2}$	$2\mathbf{b}_{M_2} + \mathbf{q}_3$	$4\mathbf{q}_1$	$\mathbf{q}_1 + 2\mathbf{b}_{M_2}$

TABLE II. Intra- and inter-layer harmonics mapping for  $t\text{MoTe}_2$  and  $t\text{WSe}_2$  systems. Each harmonic selects a single  $\mathbf{p}$  vector, with other terms related by symmetry constraints (Tab. I). The vectors  $\mathbf{b}_{M_1}$ ,  $\mathbf{b}_{M_2}$ ,  $\mathbf{q}_1$ ,  $\mathbf{q}_2$ , and  $\mathbf{q}_3$  are illustrated in Fig. 7.

## 3. Results and Validation

Following Steps 1 and 3, we have developed a continuum model for the full  $\mathbf{Q}$  lattice used in DFT calculations. As illustrated in Figs. 11 to 13(a), we compare the moiré bands calculated by DFT with those from our continuum

model. This model accurately describes the top valence bands of  $t\text{MoTe}_2$  for twist angles below  $3.89^\circ$ . Additionally, we compute the overlap  $\rho_n(\mathbf{k})$  between the wavefunctions from DFT,  $\psi_{n,\mathbf{k}}^{\text{DFT}}$ , and those from the continuum model,  $\psi_{n,\mathbf{k}}^{\text{cont}}$ , defined as:

$$\rho_n(\mathbf{k}) = \psi_{n,\mathbf{k}}^{\text{cont},\dagger} U_0^\dagger(\mathbf{k}) \psi_{n,\mathbf{k}}^{\text{DFT}}, \quad (\text{D24})$$

where  $n$  denotes the energy band index. As shown in Figs. 11 to 13(a), the minimum overlap probability for the top four bands exceeds 95%, excluding regions where bands touch.

Furthermore, we constructed a continuum model on a reduced  $\mathbf{Q}$  lattice by limiting the kinetic terms to  $O(\mathbf{k}^2)$ , following Steps 2 to 3. As depicted in Figs. 11 to 13(b), this simplification reduces the number of terms at the expense of accuracy for the third and lower valence bands.

The final Hamiltonian can be simplified by utilizing the symmetry constraints shown in Tab. I, which allow us to retain only the minimal number of independent terms. For each harmonic, a single  $\mathbf{p}$  is chosen, while the coefficients for other terms of the same degree are related by the symmetry conditions outlined in the table. The specific  $\mathbf{p}$  selected for each harmonic, both intra- and inter-layer, is detailed in Tab. II. Furthermore, for the  $t\text{MoTe}_2$  and  $t\text{WSe}_2$  systems, the parameters used in the full and reduced models are provided in Tabs. III to XX.



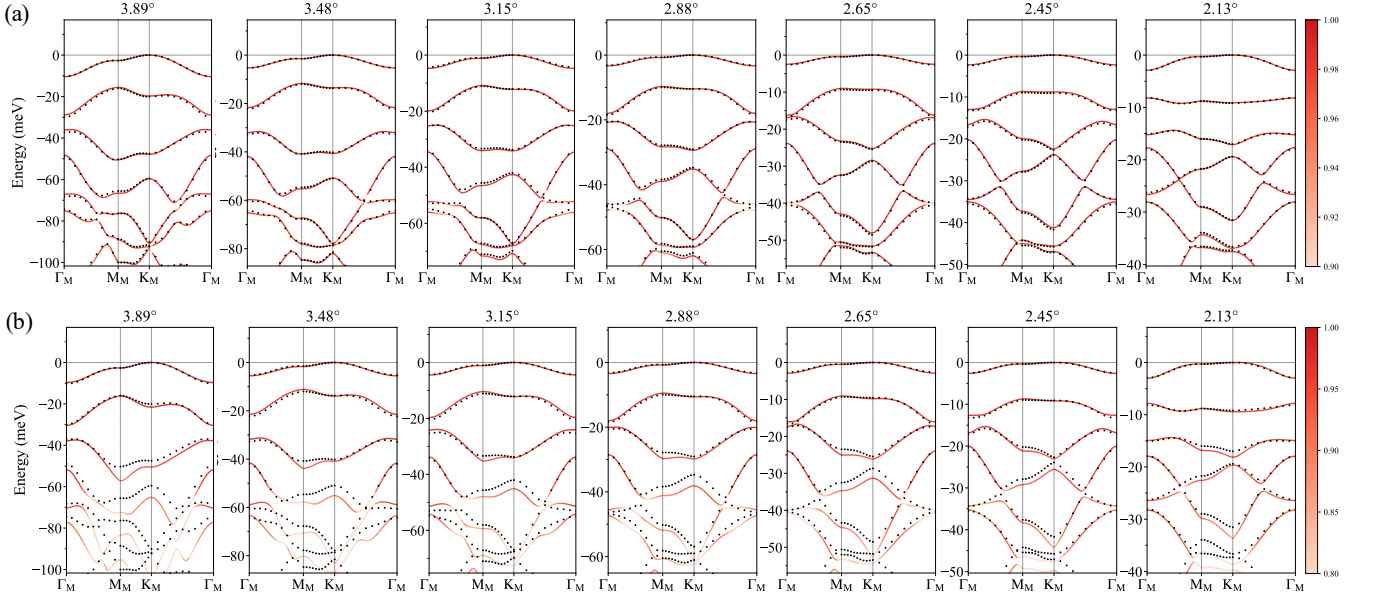


FIG. 11. **Comparison of DFT with quick basis selection and continuum model results for  $t\text{MoTe}_2$ .** (a): Full model. (b): Reduced model. Black dots represent DFT calculations, while red lines indicate continuum model bands. The gradient from dark to light in the red lines illustrates the overlap probability between the model and DFT wavefunctions for each corresponding band. For angles from  $2.13^\circ$  to  $3.15^\circ$ , we choose  $Q$  lattice up to the 8th harmonic, while for angles of  $3.48^\circ$  and  $3.89^\circ$ , we choose  $Q$  lattice up to the 7th harmonic.

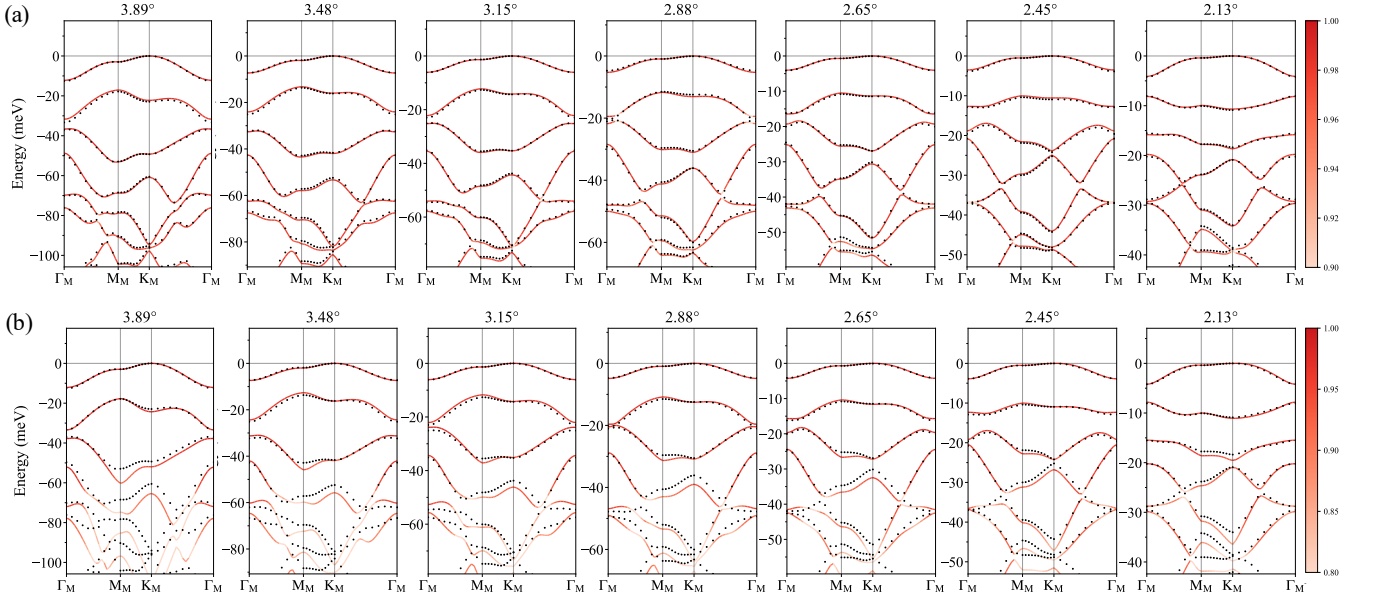


FIG. 12. **Comparison of DFT with standard basis selection and continuum model results for  $t\text{MoTe}_2$ .** (a): Full model. (b): Reduced model. Black dots represent DFT calculations, while red lines indicate continuum model bands. The gradient from dark to light in the red lines illustrates the overlap probability between the model and DFT wavefunctions for each corresponding band. For angles from  $2.13^\circ$  to  $3.15^\circ$ , we choose  $Q$  lattice up to the 8th harmonic, while for angles of  $3.48^\circ$  and  $3.89^\circ$ , we choose  $Q$  lattice up to the 7th harmonic.

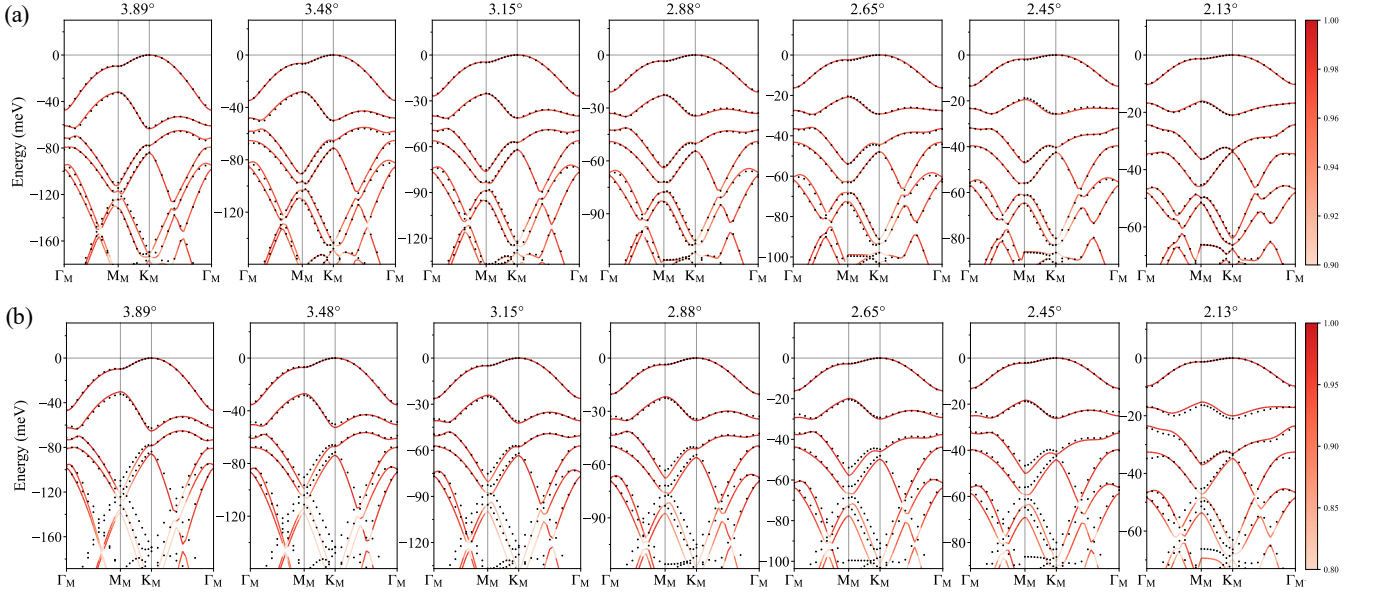


FIG. 13. Comparison of DFT with quick basis selection and continuum model results for  $tWSe_2$ . (a): Full model. (b): Reduced model. Black dots represent DFT calculations, while red lines indicate continuum model bands. The gradient from dark to light in the red lines illustrates the overlap probability between the model and DFT wavefunctions for each corresponding band. For angles from  $2.13^\circ$  to  $3.15^\circ$ , we choose  $Q$  lattice up to the 8th harmonic, while for angles from  $3.15^\circ$  to  $3.89^\circ$ , we choose  $Q$  lattice up to the 7th harmonic.

TABLE III: Kinetic term parameters ( $m_e$ ) for the full model of  $tMoTe_2$  based on DFT with quick basis selection

Parameter	$3.89^\circ$	$3.48^\circ$	$3.15^\circ$	$2.88^\circ$	$2.65^\circ$	$2.45^\circ$	$2.13^\circ$
$m^{(1,1)}$	-0.6593	-0.6537	-0.6366	-0.6406	-0.6646	-0.6640	-0.6513
$m^{(3,0)}$	1.4008	1.2052	1.3362	1.3431	1.4354	1.5619	1.4736
$m^{(2,2)}$	0.0739	0.0658	0.0616	0.0631	0.0787	0.0805	0.0705
$m^{(4,1)}$	-0.1355	-0.0880	-0.1167	-0.1153	-0.1525	-0.2344	-0.1917
$m^{(3,3)}$	-0.0116	-0.0070	-0.0073	-0.0074	-0.0141	-0.0179	-0.0116
$m^{(6,0)}$	-7.4620	-0.1239	0.7990	0.5579	0.7328	1.0873	0.4931
$m^{(5,2)}$	0.0280	0.0137	0.0212	0.0196	0.0456	0.0000	0.0000
$m^{(4,4)}$	0.0031	0.0010	0.0014	0.0013	0.0054	0.0000	0.0000
$m^{(7,1)}$	0.1055	0.0056	-0.0884	-0.0472	-0.0871	0.0000	0.0000
$m^{(6,3)}$	-0.0149	-0.0063	-0.0099	-0.0081	0.0000	0.0000	0.0000
$m^{(9,0)}$	-3.0218	0.1219	1.8229	-16.8653	0.0000	0.0000	0.0000
$m^{(5,5)}$	-0.0018	-0.0003	-0.0006	-0.0006	0.0000	0.0000	0.0000
$m^{(8,2)}$	-0.0217	-0.0011	0.0396	0.0158	0.0000	0.0000	0.0000

TABLE IV: Intralayer potential term parameters (meV) for the full model of  $tMoTe_2$  based on DFT with quick basis selection

Parameter	$3.89^\circ$	$3.48^\circ$	$3.15^\circ$	$2.88^\circ$	$2.65^\circ$	$2.45^\circ$	$2.13^\circ$
$V_{b,b_{M_1}}^{0,0}$	-0.0038	-0.0153	-0.0229	-0.0177	-0.0156	-0.0170	-0.0251
	-3.9103i	+4.2608i	-3.7636i	+3.4576i	-3.0791i	-2.6988i	-1.8658i

TABLE IV: Intralayer potential term parameters (meV) for the full model of  $t\text{MoTe}_2$  based on DFT with quick basis selection (continued)

Parameter	3.89°	3.48°	3.15°	2.88°	2.65°	2.45°	2.13°
$V_{b,b_{M_1}}^{1,0}$	-1.9224 -8.8822i	-0.8617 +4.8011i	-1.1931 -10.1349i	0.0506 +1.4581i	-1.1722 -10.6454i	-1.1432 -10.6991i	-1.1401 -10.5061i
$V_{b,b_{M_1}}^{0,1}$	-0.8895 -5.2475i	-2.0266 +10.4007i	0.0894 -2.4862i	-1.1905 +10.4842i	0.0309 -0.5232i	0.0200 +0.2835i	-0.0857 +1.6318i
$V_{b,b_{M_1}}^{2,0}$	3.9339 -31.2143i	0.7975 -43.9430i	0.9248 -37.3171i	-1.5565 -44.4795i	1.1120 -41.5515i	1.2088 -42.7443i	2.0513 -43.7408i
$V_{b,b_{M_1}}^{1,1}$	-4.2521 +16.1930i	-4.8541 -18.8353i	0.1025 +19.0470i	-0.6967 -20.6775i	-1.5309 +21.8434i	-2.2280 +22.8194i	-3.3843 +24.3039i
$V_{b,b_{M_1}}^{0,2}$	1.2764 +36.1156i	3.8105 +37.7526i	-1.9716 +42.3784i	0.9337 +39.8775i	-1.1922 +45.5950i	-0.7637 +46.0822i	0.5324 +45.0861i
$V_{b,b_{M_1}}^{3,0}$	6.1458 -0.0998i	0.8080 -29.8730i	4.6664 -3.0046i	-3.3064 -22.6237i	3.5331 -3.3016i	2.6259 -3.5641i	-0.1372 -4.0415i
$V_{b,b_{M_1}}^{2,1}$	20.4314 +25.1906i	6.3482 -118.4927i	11.5889 +38.0486i	-6.4793 -81.6020i	18.1359 +58.9734i	22.3722 +68.4880i	33.3750 +84.5297i
$V_{b,b_{M_1}}^{1,2}$	4.3963 +106.3676i	25.8807 -38.0924i	-7.5480 +86.9510i	14.4575 -48.9941i	-4.5543 +74.7428i	-1.7986 +67.5533i	6.8826 +51.7421i
$V_{b,b_{M_1}}^{0,3}$	0.9148 +24.7819i	7.7312 +0.6002i	-3.7373 +21.9524i	4.2524 +3.1002i	-2.5903 +22.6319i	-1.8045 +22.2944i	0.4479 +20.8424i
$V_{b,b_{M_1}}^{4,0}$	-9.8985 -30.4122i	-3.4071 +13.8173i	-12.1542 -21.6114i	7.2962 +17.9328i	-10.9243 -26.9518i	-8.5384 -29.6940i	1.2549 -35.6212i
$V_{b,b_{M_1}}^{3,1}$	-51.4957 +153.4492i	-3.7794 +328.5877i	-20.3925 +202.4114i	50.6504 +305.8023i	-35.3822 +270.9938i	-46.9862 +308.5394i	-85.9207 +391.1650i
$V_{b,b_{M_1}}^{2,2}$	24.8783 -155.8761i	24.2107 +200.7365i	20.2844 -169.6732i	21.4592 +207.9921i	19.4717 -250.5087i	12.5277 -300.8471i	-22.7435 -426.7805i
$V_{b,b_{M_1}}^{1,3}$	-5.8288 -251.0753i	-69.5402 -199.2444i	52.8908 -278.4752i	-25.9008 -236.0957i	42.9811 -324.9832i	29.7284 -337.6156i	-21.3059 -333.5971i
$V_{b,b_{M_1}}^{0,4}$	-1.7984 -9.7372i	-15.8062 +38.4722i	5.6717 -14.7323i	-12.1507 +24.3353i	9.2614 -20.8743i	11.7160 -23.9975i	18.4391 -32.2906i
$V_{b,b_{M_1}+b_{M_2}}^{0,0}$	-0.2220 -0.0350i	-0.2107 -0.0237i	-0.1493 +0.0182i	-0.1240 -0.0503i	-0.0957 +0.0706i	-0.0699 +0.0697i	-0.0409 +0.0679i
$V_{b,b_{M_1}+b_{M_2}}^{1,0}$	0.6074 -0.1193i	0.6261 -0.4976i	0.2080 -0.4738i	0.4283 -0.4904i	-0.2143 -0.6687i	-0.2970 -0.6897i	-0.3831 -0.6816i
$V_{b,b_{M_1}+b_{M_2}}^{0,1}$	0.8170 +0.6835i	0.1051 +0.4278i	0.6238 +0.6584i	-0.0416 +0.5963i	0.2734 +0.3638i	0.1883 +0.3048i	0.0551 +0.1942i
$V_{b,b_{M_1}+b_{M_2}}^{2,0}$	-1.0833 +1.0870i	0.2174 -0.6530i	-0.4740 +0.5046i	-0.2169 +0.0653i	0.9552 -0.1341i	1.3488 -0.4270i	1.9156 -0.8187i
$V_{b,b_{M_1}+b_{M_2}}^{1,1}$	0.4694 +1.7513i	1.8734 -0.7162i	2.1676 +1.0241i	2.4946 -0.5553i	2.5605 +0.2589i	2.4918 +0.2045i	2.0953 +0.1590i
$V_{b,b_{M_1}+b_{M_2}}^{0,2}$	-0.2833 +0.4096i	0.1523 -0.7130i	-0.5690 -0.3496i	0.3121 -0.1860i	0.1174 +0.1842i	0.3550 +0.3065i	0.8907 +0.4333i
$V_{b,b_{M_1}+b_{M_2}}^{3,0}$	-2.8244 -0.7362i	-3.6698 +4.8861i	-0.3000 +0.6165i	-1.6796 +3.1128i	0.8304 +1.1524i	1.1345 +1.2800i	1.2941 +1.2626i
$V_{b,b_{M_1}+b_{M_2}}^{2,1}$	-4.2301 +1.7518i	-4.1646 +4.4647i	-2.1032 +3.3460i	-1.4869 +5.7691i	-3.4734 +2.0627i	-5.8787 +0.4988i	-13.5871 -4.4866i
$V_{b,b_{M_1}+b_{M_2}}^{1,2}$	-2.6295 -8.0183i	-4.0483 -2.2408i	-2.0803 -7.1170i	-2.3570 -2.9130i	-0.8100 -4.9011i	-0.2591 -4.9152i	1.7830 -5.2951i

TABLE IV: Intralayer potential term parameters (meV) for the full model of  $t\text{MoTe}_2$  based on DFT with quick basis selection (continued)

Parameter	3.89°	3.48°	3.15°	2.88°	2.65°	2.45°	2.13°
$V_{b,b_{M_1}+b_{M_2}}^{0,3}$	-3.4035 -5.5441i	-3.3970 -0.6341i	-2.0437 -3.3621i	0.3591 -0.9353i	-1.4185 -3.1063i	-1.3974 -3.3715i	-1.5673 -3.9465i
$V_{b,b_{M_1}+b_{M_2}}^{4,0}$	3.0011 +1.4985i	8.0895 -3.4034i	2.0194 -3.5421i	3.5029 -1.5920i	3.5688 -8.3205i	5.0422 -11.2344i	10.0006 -18.7272i
$V_{b,b_{M_1}+b_{M_2}}^{3,1}$	13.1595 -7.2793i	1.0325 -6.7680i	7.3072 -3.2806i	1.5984 -20.5032i	-2.6264 +6.1431i	-4.5129 +14.5742i	-2.7657 +40.0878i
$V_{b,b_{M_1}+b_{M_2}}^{2,2}$	8.0439 -4.2590i	15.5749 +3.0004i	-0.9566 -4.0138i	4.3452 +2.5053i	14.4270 -1.3341i	29.8600 -0.8430i	76.1246 -0.9219i
$V_{b,b_{M_1}+b_{M_2}}^{1,3}$	4.0730 +10.0208i	6.5622 +8.5032i	5.6399 +16.7504i	1.7749 -0.4694i	-3.8396 +27.3207i	-10.2515 +38.8199i	-30.5441 +74.2310i
$V_{b,b_{M_1}+b_{M_2}}^{0,4}$	5.6448 +4.7690i	6.2469 +0.4883i	2.7159 +2.7285i	2.6158 +5.8391i	4.1750 +0.3148i	4.7006 -1.1253i	5.3105 -5.5274i
$V_{b,2b_{M_1}}^{0,0}$	0.1506 -0.3547i	0.1595 +0.6508i	0.1100 -0.8208i	0.1087 +1.0594i	0.0961 -1.2804i	0.0772 -1.4752i	0.0617 -1.7275i
$V_{b,2b_{M_1}}^{1,0}$	0.4688 -0.7772i	-0.3506 +2.3815i	0.1175 -1.9383i	-0.2300 +3.1226i	-0.1131 -3.0272i	-0.1827 -3.5033i	-0.3749 -4.3053i
$V_{b,2b_{M_1}}^{0,1}$	-0.1319 -1.3848i	0.3188 +1.5684i	-0.2174 -2.7576i	0.0125 +2.4910i	-0.1768 -3.3532i	-0.1280 -3.4548i	-0.1638 -3.2391i
$V_{b,2b_{M_1}}^{2,0}$	1.2696 -4.3737i	-1.0498 -1.3998i	0.5785 -7.6600i	-0.3591 -5.6424i	0.4703 -12.5861i	0.2108 -14.8057i	0.3838 -18.5465i
$V_{b,2b_{M_1}}^{1,1}$	-3.6105 -3.3676i	-5.1584 +4.4742i	-3.3611 -2.7506i	-3.7503 +2.2386i	-4.0285 -1.5210i	-4.3088 -0.6778i	-5.2587 +1.5458i
$V_{b,2b_{M_1}}^{0,2}$	-1.1856 +0.0670i	1.0575 +7.6897i	-0.5742 +3.4937i	0.5011 +10.1855i	-0.3393 +8.0127i	-0.2412 +10.3783i	-0.0443 +14.6238i
$V_{b,2b_{M_1}}^{3,0}$	1.3497 +1.8860i	2.5181 -14.7597i	1.0049 -2.8970i	-2.7982 -19.5761i	1.1672 -5.1635i	0.9543 -6.5202i	-0.5106 -9.7046i
$V_{b,2b_{M_1}}^{2,1}$	-4.0854 +8.1364i	1.6527 -53.2210i	-0.6814 +9.0710i	-3.3493 -69.6706i	7.0560 +21.3411i	12.2225 +28.6774i	27.5689 +44.4714i
$V_{b,2b_{M_1}}^{1,2}$	-1.3030 +30.1712i	0.4116 -14.6325i	-3.0195 +56.3135i	2.2817 -14.7658i	-3.1639 +81.5790i	-1.6165 +91.6122i	8.0011 +104.8782i
$V_{b,2b_{M_1}}^{0,3}$	2.0620 +8.3122i	3.6061 -1.2849i	-1.7291 +15.9079i	1.1843 +3.9338i	-3.7119 +22.5733i	-4.3835 +24.8436i	-4.2215 +27.0095i
$V_{b,2b_{M_1}}^{4,0}$	1.3830 -7.3022i	-0.1924 +6.1086i	0.6463 -8.1507i	4.0707 +9.2420i	1.4560 -12.2065i	2.5584 -13.4659i	8.8152 -13.5341i
$V_{b,2b_{M_1}}^{3,1}$	-9.9312 +14.1928i	-2.5795 +63.5305i	-8.4300 +49.1585i	19.5100 +106.1657i	-21.1396 +91.3933i	-28.5697 +115.3089i	-56.2425 +168.0963i
$V_{b,2b_{M_1}}^{2,2}$	19.2584 -21.4877i	21.7938 +44.5751i	19.4840 -41.5357i	21.4612 +63.3757i	19.3014 -89.8556i	13.2190 -121.3801i	-22.1592 -201.9485i
$V_{b,2b_{M_1}}^{1,3}$	0.7652 -32.6395i	-21.3105 -33.5546i	15.4503 -76.8530i	-13.3676 -69.1326i	22.7241 -137.2271i	22.0956 -167.6892i	2.7614 -220.9637i
$V_{b,2b_{M_1}}^{0,4}$	-0.4540 -2.6677i	-0.6741 +11.7955i	2.5507 -6.9242i	0.8985 +10.4238i	5.9158 -11.0939i	8.0433 -12.5184i	13.0293 -13.8241i
$V_{b,2b_{M_1}+b_{M_2}}^{0,0}$	0.0000 +0.0000i	-0.0663 -0.0112i	-0.0814 +0.0364i	-0.0716 -0.0570i	-0.0660 +0.0690i	-0.0513 +0.0746i	-0.0386 +0.0587i
$V_{b,2b_{M_1}+b_{M_2}}^{1,0}$	0.0000 +0.0000i	0.0197 -0.0671i	0.2970 +0.0998i	0.2204 -0.3307i	0.0970 -0.0199i	-0.0075 -0.1047i	-0.2201 -0.2853i

TABLE IV: Intralayer potential term parameters (meV) for the full model of  $t\text{MoTe}_2$  based on DFT with quick basis selection (continued)

Parameter	3.89°	3.48°	3.15°	2.88°	2.65°	2.45°	2.13°
$V_{b,2b_{M_1}+b_{M_2}}^{0,1}$	0.0000 +0.0000i	0.1139 +0.0006i	0.2462 +0.3229i	0.2128 -0.0707i	0.1705 +0.3001i	0.1251 +0.2615i	0.0281 +0.1140i
$V_{b,2b_{M_1}+b_{M_2}}^{2,0}$	0.0000 +0.0000i	1.3328 -2.0709i	-0.5772 +1.1615i	0.0803 -0.4305i	0.0914 +1.4644i	0.5510 +1.4487i	1.4883 +1.3369i
$V_{b,2b_{M_1}+b_{M_2}}^{1,1}$	0.0000 +0.0000i	0.2197 -3.4192i	0.9809 +1.7234i	0.5952 -1.3029i	2.3698 +1.5805i	3.1338 +1.6875i	4.7670 +2.1548i
$V_{b,2b_{M_1}+b_{M_2}}^{0,2}$	0.0000 +0.0000i	-0.7593 -1.1050i	0.3915 +0.2566i	-0.4135 -0.8918i	0.5684 +0.0321i	0.7016 +0.0805i	1.0572 +0.3893i
$V_{b,2b_{M_1}+b_{M_2}}^{3,0}$	0.0000 +0.0000i	-6.1065 +5.4102i	0.1977 -1.8525i	-0.8829 +3.6151i	0.5596 -2.1396i	0.5903 -2.3755i	0.0135 -3.0002i
$V_{b,2b_{M_1}+b_{M_2}}^{2,1}$	0.0000 +0.0000i	-2.7464 +17.3292i	-5.6241 -4.0922i	-1.6893 +8.0825i	-9.6651 -6.8837i	-12.4397 -8.3738i	-19.2513 -12.6071i
$V_{b,2b_{M_1}+b_{M_2}}^{1,2}$	0.0000 +0.0000i	2.7628 +6.8434i	-6.2070 -6.3490i	-2.5601 +0.4563i	-11.7890 -6.3738i	-15.3356 -6.8491i	-22.7981 -8.8907i
$V_{b,2b_{M_1}+b_{M_2}}^{0,3}$	0.0000 +0.0000i	0.0273 +0.3669i	-1.4963 -1.4928i	-0.2845 -0.2935i	-1.6485 -1.2574i	-1.7579 -1.2174i	-1.8571 -1.2768i
$V_{b,2b_{M_1}+b_{M_2}}^{4,0}$	0.0000 +0.0000i	6.4962 -2.0806i	-1.7834 +2.2339i	0.6336 -2.6675i	-2.3217 +1.2148i	-2.5212 +0.1989i	-2.3100 -2.8117i
$V_{b,2b_{M_1}+b_{M_2}}^{3,1}$	0.0000 +0.0000i	12.0405 -18.1751i	8.1512 +4.2503i	2.2385 -10.6355i	8.6878 +9.3458i	9.4049 +13.8817i	13.6892 +27.0472i
$V_{b,2b_{M_1}+b_{M_2}}^{2,2}$	0.0000 +0.0000i	-4.5033 -17.9452i	13.2088 +3.8928i	3.7110 -1.7180i	28.9316 +9.1711i	40.3804 +12.6726i	70.5816 +23.3065i
$V_{b,2b_{M_1}+b_{M_2}}^{1,3}$	0.0000 +0.0000i	0.0000 +0.0000i	8.0061 +2.7647i	5.8632 +4.8158i	13.7672 +3.2105i	17.5398 +4.7693i	23.9652 +13.0692i
$V_{b,3b_{M_1}}^{0,0}$	0.0000 +0.0000i	0.0000 +0.0000i	0.0000 +0.0000i	0.0000 +0.0000i	0.0694 -0.2297i	0.0627 -0.3144i	0.0766 -0.5174i
$V_{b,3b_{M_1}}^{1,0}$	0.0000 +0.0000i	0.0000 +0.0000i	0.0000 +0.0000i	0.0000 +0.0000i	0.2603 -0.5514i	0.1617 -0.7447i	-0.1425 -1.1959i
$V_{b,3b_{M_1}}^{0,1}$	0.0000 +0.0000i	0.0000 +0.0000i	0.0000 +0.0000i	0.0000 +0.0000i	0.0464 -0.8658i	-0.0071 -1.1746i	-0.1718 -1.7185i
$V_{b,3b_{M_1}}^{2,0}$	0.0000 +0.0000i	0.0000 +0.0000i	0.0000 +0.0000i	0.0000 +0.0000i	1.5840 -1.8668i	2.1600 -2.9951i	3.7831 -6.0078i
$V_{b,3b_{M_1}}^{1,1}$	0.0000 +0.0000i	0.0000 +0.0000i	0.0000 +0.0000i	0.0000 +0.0000i	-1.9364 -0.6630i	-1.3509 -0.6106i	-0.1664 -0.4852i
$V_{b,3b_{M_1}}^{0,2}$	0.0000 +0.0000i	0.0000 +0.0000i	0.0000 +0.0000i	0.0000 +0.0000i	-0.9868 +0.1723i	-0.8017 +0.9246i	-0.4829 +3.1981i
$V_{b,3b_{M_1}}^{3,0}$	0.0000 +0.0000i	0.0000 +0.0000i	0.0000 +0.0000i	0.0000 +0.0000i	-2.5405 -0.0518i	-4.8151 +1.0997i	-9.8008 +3.8556i
$V_{b,3b_{M_1}}^{2,1}$	0.0000 +0.0000i	0.0000 +0.0000i	0.0000 +0.0000i	0.0000 +0.0000i	-7.9054 -4.3792i	-12.4327 -3.3972i	-19.3756 +3.4575i
$V_{b,3b_{M_1}}^{1,2}$	0.0000 +0.0000i	0.0000 +0.0000i	0.0000 +0.0000i	0.0000 +0.0000i	-1.8390 +7.7748i	-3.4539 +10.0744i	-6.1538 +14.9782i
$V_{b,3b_{M_1}}^{0,3}$	0.0000 +0.0000i	0.0000 +0.0000i	0.0000 +0.0000i	0.0000 +0.0000i	1.6111 +3.3921i	1.6858 +4.0501i	2.1182 +4.6142i
$V_{b,3b_{M_1}}^{4,0}$	0.0000 +0.0000i	0.0000 +0.0000i	0.0000 +0.0000i	0.0000 +0.0000i	4.6762 -7.7960i	6.7166 -12.1563i	12.4062 -22.0001i

TABLE IV: Intralayer potential term parameters (meV) for the full model of  $t\text{MoTe}_2$  based on DFT with quick basis selection (continued)

Parameter	3.89°	3.48°	3.15°	2.88°	2.65°	2.45°	2.13°
$V_{b,3b_{M_1}}^{3,1}$	0.0000 +0.0000i	0.0000 +0.0000i	0.0000 +0.0000i	0.0000 +0.0000i	-0.2869 +16.9462i	6.2053 +21.9163i	14.8079 +32.4771i
$V_{b,3b_{M_1}}^{2,2}$	0.0000 +0.0000i	0.0000 +0.0000i	0.0000 +0.0000i	0.0000 +0.0000i	19.4974 +11.0891i	28.0817 +12.4500i	43.5997 +8.0928i

TABLE V: Interlayer potential term parameters (meV) for the full model of  $t\text{MoTe}_2$  based on DFT with quick basis selection

Parameter	3.89°	3.48°	3.15°	2.88°	2.65°	2.45°	2.13°
$w_{bt,\mathbf{q}_1}^{0,0}$	-1.4859 +0.4139i	-1.7468 -0.0760i	-1.2903 +0.2975i	-1.4904 +0.0092i	-1.1591 +0.2210i	-1.0955 +0.1904i	-0.9901 +0.1414i
$w_{bt,\mathbf{q}_1}^{1,0}$	3.2918 -2.0525i	3.5455 +8.1102i	4.1767 -1.9454i	4.3257 +6.8691i	4.6972 -2.0180i	4.8638 -1.9961i	5.1894 -1.9259i
$w_{bt,\mathbf{q}_1}^{2,0}$	38.9164 -3.6037i	37.5726 +1.7483i	40.6076 -1.7984i	39.1207 +0.8536i	42.3461 -0.8450i	43.0546 -0.4813i	44.1041 +0.1205i
$w_{bt,\mathbf{q}_1}^{1,1}$	3.2951 -3.6016i	8.7480 -2.3152i	1.5579 -2.0723i	5.2278 -4.4488i	1.7887 -2.2264i	1.7602 -2.2807i	1.5218 -2.3184i
$w_{bt,\mathbf{q}_1}^{3,0}$	-12.2950 +9.6872i	-21.4501 +13.6503i	-16.3108 +7.9524i	-22.7329 +14.4772i	-21.2502 +5.7739i	-23.2894 +4.7097i	-26.9499 +2.6459i
$w_{bt,\mathbf{q}_1}^{2,1}$	-30.6028 +12.3370i	-43.6718 -55.2743i	-46.7290 +11.7340i	-57.7625 -43.9844i	-58.6792 +16.7599i	-63.5998 +18.6761i	-73.7787 +22.1133i
$w_{bt,\mathbf{q}_1}^{4,0}$	27.7311 -18.8552i	36.2954 +20.9406i	42.0112 -22.6876i	48.2057 +22.5623i	53.4292 -21.7174i	57.5906 -20.2418i	63.9670 -15.6066i
$w_{bt,\mathbf{q}_1}^{3,1}$	-157.0302 +1.1366i	-165.4563 +8.0618i	-159.7197 -18.1101i	-165.0848 +27.0206i	-170.6481 -36.3355i	-176.7534 -46.2578i	-185.4180 -68.9807i
$w_{bt,\mathbf{q}_1}^{2,2}$	-47.7002 -3.6899i	-60.7220 +2.8002i	-38.2969 -21.9927i	-46.5713 +21.1198i	-53.7677 -18.5559i	-60.4477 -14.1427i	-70.2329 -0.9745i
$w_{bt,-2\mathbf{q}_1}^{0,0}$	0.4465 +0.1950i	0.2576 -0.3226i	0.3883 +0.2205i	0.2262 -0.3175i	0.3844 +0.2210i	0.3774 +0.2124i	0.3687 +0.1928i
$w_{bt,-2\mathbf{q}_1}^{1,0}$	0.7265 +0.9881i	0.2903 -1.1468i	0.7839 +1.0269i	0.6748 -1.3857i	0.8633 +1.0761i	0.9086 +1.0805i	1.0231 +1.0673i
$w_{bt,-2\mathbf{q}_1}^{2,0}$	1.7920 +1.0970i	-1.9938 -1.8840i	2.4625 +0.6025i	-0.3698 -0.7312i	3.7906 +0.1265i	4.4846 -0.0570i	5.8699 -0.3224i
$w_{bt,-2\mathbf{q}_1}^{1,1}$	-3.2722 +1.0013i	-0.2319 +1.1076i	-2.2533 +0.6426i	0.4648 +0.6095i	-2.8039 +0.8832i	-3.0388 +1.1339i	-3.4473 +1.8159i
$w_{bt,-2\mathbf{q}_1}^{3,0}$	2.1002 +4.8290i	-4.7865 -6.0138i	-0.8738 +5.0540i	-1.3865 -5.8311i	0.4214 +5.1838i	0.9178 +5.0577i	1.8469 +4.4847i
$w_{bt,-2\mathbf{q}_1}^{2,1}$	-12.7651 -7.7966i	-2.2768 +10.3226i	-7.7420 -10.1974i	-4.5319 +12.4385i	-5.3837 -15.4497i	-4.2516 -18.0501i	-2.3353 -22.9338i
$w_{bt,-2\mathbf{q}_1}^{4,0}$	-1.4618 +4.9543i	0.8817 -8.4170i	-0.9978 +0.2581i	1.5664 -1.1819i	4.4201 +2.1898i	7.5620 +3.2128i	15.2501 +5.9364i
$w_{bt,-2\mathbf{q}_1}^{3,1}$	-2.6824 -15.5655i	3.6688 +23.5364i	0.6458 -4.5366i	0.9391 +5.4879i	-0.3221 -6.7880i	-3.1867 -8.5427i	-15.3629 -14.3102i
$w_{bt,-2\mathbf{q}_1}^{2,2}$	2.7456 -0.0876i	3.0547 +4.2918i	-2.8395 -6.0784i	-0.5206 +12.0721i	2.0086 -20.8630i	5.1372 -32.7528i	12.5575 -66.3946i

TABLE V: Interlayer potential term parameters (meV) for the full model of  $t\text{MoTe}_2$  based on DFT with quick basis selection (continued)

Parameter	3.89°	3.48°	3.15°	2.88°	2.65°	2.45°	2.13°
$w_{bt, \mathbf{q}_1 + \mathbf{b}_{M_2}}^{0,0}$	-0.4506 +0.1263i	-0.6573 -0.1970i	-0.6836 +0.1989i	-0.7651 -0.2103i	-0.8214 +0.2123i	-0.8593 +0.2092i	-0.8999 +0.1905i
$w_{bt, \mathbf{q}_1 + \mathbf{b}_{M_2}}^{1,0}$	0.7039 -0.0526i	-0.5314 +1.3091i	0.9747 -0.1547i	-0.5236 +1.7111i	1.0894 -0.2572i	1.1406 -0.3025i	1.2526 -0.3861i
$w_{bt, \mathbf{q}_1 + \mathbf{b}_{M_2}}^{0,1}$	-0.4143 -0.7180i	0.7885 +0.1394i	-0.5405 -1.4761i	1.0307 +0.2085i	-0.4885 -1.8743i	-0.4472 -1.9837i	-0.3517 -2.0937i
$w_{bt, \mathbf{q}_1 + \mathbf{b}_{M_2}}^{2,0}$	3.2616 -1.3407i	3.0845 -0.9830i	5.8578 -1.4056i	4.7957 -0.4722i	8.0857 -1.5324i	8.9178 -1.4939i	10.1163 -1.2550i
$w_{bt, \mathbf{q}_1 + \mathbf{b}_{M_2}}^{1,1}$	0.6942 -1.7528i	1.5991 +2.7105i	1.2324 -1.8183i	1.7431 +1.9510i	2.1701 -2.0004i	2.5523 -1.9779i	3.2729 -1.6877i
$w_{bt, \mathbf{q}_1 + \mathbf{b}_{M_2}}^{0,2}$	1.6102 +0.9956i	5.7500 +1.8649i	3.9029 +0.4658i	7.0735 +1.5149i	5.5543 +0.4415i	6.1887 +0.4105i	7.1492 +0.3221i
$w_{bt, \mathbf{q}_1 + \mathbf{b}_{M_2}}^{3,0}$	-1.0944 -0.8065i	-4.0023 +0.5618i	-0.2713 -0.9636i	-2.5659 +0.1052i	-2.4714 -1.1367i	-3.8036 -1.3619i	-6.8049 -1.8890i
$w_{bt, \mathbf{q}_1 + \mathbf{b}_{M_2}}^{2,1}$	-2.1485 +10.8379i	9.0423 -0.8346i	-7.9015 +14.3507i	2.8667 -5.1612i	-8.5864 +20.5066i	-8.6264 +22.9790i	-9.1310 +26.6119i
$w_{bt, \mathbf{q}_1 + \mathbf{b}_{M_2}}^{1,2}$	7.3507 -1.9969i	-2.6823 -16.2702i	3.6646 +3.5145i	-8.2637 -17.6094i	1.6132 +6.8259i	0.0431 +8.6849i	-4.2793 +13.2149i
$w_{bt, \mathbf{q}_1 + \mathbf{b}_{M_2}}^{0,3}$	-2.5548 -0.1526i	-2.4764 +0.5608i	-2.2220 +0.3428i	-1.2994 +0.9697i	-2.8190 -0.5376i	-3.0174 -0.9865i	-3.3252 -1.8657i
$w_{bt, \mathbf{q}_1 + \mathbf{b}_{M_2}}^{4,0}$	2.3458 -0.5263i	0.3923 +7.0118i	4.7411 -2.6185i	0.4687 +5.6159i	6.9658 -2.1946i	7.4776 -0.8381i	7.3698 +4.5125i
$w_{bt, \mathbf{q}_1 + \mathbf{b}_{M_2}}^{3,1}$	-9.7880 -0.4832i	-14.4378 -11.2291i	-18.5212 +4.7395i	-19.6977 +4.0041i	-29.4397 -2.3533i	-34.2437 -8.4491i	-41.9236 -25.9117i
$w_{bt, \mathbf{q}_1 + \mathbf{b}_{M_2}}^{2,2}$	-24.0939 -4.9508i	-40.8189 +7.8517i	-25.3635 -14.8522i	-36.3196 +17.3278i	-47.2134 -19.0923i	-58.0280 -19.9902i	-77.1318 -21.9127i
$w_{bt, \mathbf{q}_1 + \mathbf{b}_{M_2}}^{1,3}$	-7.7287 +7.3378i	-22.0899 +3.8100i	-15.1823 -1.1054i	-24.2948 -1.9093i	-23.5484 -8.0077i	-26.7661 -13.4621i	-30.0440 -30.0352i
$w_{bt, \mathbf{q}_1 + \mathbf{b}_{M_2}}^{0,4}$	0.1229 -4.2498i	3.6992 +1.1846i	-0.1586 -5.4428i	6.0380 +2.7557i	1.0778 -5.2475i	1.6367 -4.3221i	2.5558 -1.0988i
$w_{bt, 2\mathbf{b}_{M_2} + \mathbf{q}_3}^{0,0}$	0.0000 +0.0000i	0.1257 +0.0065i	0.1235 +0.0126i	0.1453 -0.0392i	0.1639 +0.0747i	0.1758 +0.0968i	0.1962 +0.1301i
$w_{bt, 2\mathbf{b}_{M_2} + \mathbf{q}_3}^{1,0}$	0.0000 +0.0000i	0.2160 -0.0904i	-0.0215 +0.2439i	0.2317 +0.0379i	-0.0810 +0.2630i	-0.1103 +0.2754i	-0.1585 +0.3099i
$w_{bt, 2\mathbf{b}_{M_2} + \mathbf{q}_3}^{0,1}$	0.0000 +0.0000i	0.0081 -0.2273i	0.2665 -0.0128i	-0.0453 -0.2356i	0.2375 -0.0504i	0.2362 -0.0718i	0.2530 -0.1322i
$w_{bt, 2\mathbf{b}_{M_2} + \mathbf{q}_3}^{2,0}$	0.0000 +0.0000i	-0.7930 +0.7042i	-0.5909 -0.4649i	0.4771 +0.5590i	-0.5917 -1.2693i	-0.6480 -1.7129i	-0.8848 -2.6434i
$w_{bt, 2\mathbf{b}_{M_2} + \mathbf{q}_3}^{1,1}$	0.0000 +0.0000i	-0.3287 +0.0587i	0.1038 -0.1855i	0.3399 -1.7112i	-0.9428 -0.8412i	-1.5518 -1.1093i	-2.8143 -1.5114i
$w_{bt, 2\mathbf{b}_{M_2} + \mathbf{q}_3}^{0,2}$	0.0000 +0.0000i	-0.6823 +0.0387i	-0.5939 -0.5908i	-1.3603 -0.0286i	-0.7416 -0.9521i	-0.8123 -1.0706i	-0.9436 -1.2069i
$w_{bt, 2\mathbf{b}_{M_2} + \mathbf{q}_3}^{3,0}$	0.0000 +0.0000i	-0.0672 +1.0459i	-2.0632 +1.4330i	-4.9396 -1.1360i	-3.7810 +4.2184i	-4.6092 +5.9676i	-5.8600 +9.8251i
$w_{bt, 2\mathbf{b}_{M_2} + \mathbf{q}_3}^{2,1}$	0.0000 +0.0000i	3.0337 -3.4518i	-1.4464 -3.9754i	-7.3529 +3.4810i	1.6224 +3.6500i	3.9284 +8.7507i	9.4520 +20.8501i

TABLE V: Interlayer potential term parameters (meV) for the full model of  $t\text{MoTe}_2$  based on DFT with quick basis selection (continued)

Parameter	3.89°	3.48°	3.15°	2.88°	2.65°	2.45°	2.13°
$w_{bt,2\mathbf{b}_{M_2}+\mathbf{q}_3}^{1,2}$	0.0000 +0.0000i	-0.8294 +4.7325i	0.4986 +6.5112i	3.1424 +16.5676i	9.8656 +7.9193i	15.8141 +7.9783i	29.6675 +6.9882i
$w_{bt,2\mathbf{b}_{M_2}+\mathbf{q}_3}^{0,3}$	0.0000 +0.0000i	0.0183 -0.5573i	-0.0898 -0.1778i	2.2343 -1.0167i	0.5220 -1.1109i	0.8534 -1.8865i	1.3128 -3.7202i
$w_{bt,2\mathbf{b}_{M_2}+\mathbf{q}_3}^{4,0}$	0.0000 +0.0000i	0.6546 -0.4191i	4.1318 +1.5767i	4.3020 +4.8312i	8.9742 +0.5124i	12.1192 -1.0352i	18.7694 -7.3409i
$w_{bt,2\mathbf{b}_{M_2}+\mathbf{q}_3}^{3,1}$	0.0000 +0.0000i	-2.7491 -8.6566i	3.1618 +0.1248i	16.9528 -13.7282i	2.3911 -9.9261i	0.9460 -16.4952i	-3.0910 -30.6813i
$w_{bt,2\mathbf{b}_{M_2}+\mathbf{q}_3}^{2,2}$	0.0000 +0.0000i	6.6956 +7.1903i	10.8944 -10.2260i	18.2375 -16.2011i	-2.2439 -35.0042i	-14.4296 -53.1653i	-52.5035 -102.8732i
$w_{bt,2\mathbf{b}_{M_2}+\mathbf{q}_3}^{1,3}$	0.0000 +0.0000i	0.4521 -1.7309i	-2.8205 +1.5922i	-14.2658 -15.0177i	-15.9115 +18.3799i	-25.3700 +32.4280i	-48.7622 +73.1020i
$w_{bt,4\mathbf{q}_1}^{0,0}$	0.0000 +0.0000i	0.0000 +0.0000i	0.0000 +0.0000i	0.0000 +0.0000i	-0.0504 +0.0103i	-0.0610 +0.0158i	-0.0776 +0.0240i
$w_{bt,4\mathbf{q}_1}^{1,0}$	0.0000 +0.0000i	0.0000 +0.0000i	0.0000 +0.0000i	0.0000 +0.0000i	0.0092 -0.0469i	0.0425 -0.0542i	0.1091 -0.0725i
$w_{bt,4\mathbf{q}_1}^{2,0}$	0.0000 +0.0000i	0.0000 +0.0000i	0.0000 +0.0000i	0.0000 +0.0000i	0.6890 -0.1134i	1.0838 -0.2621i	1.7928 -0.6421i
$w_{bt,4\mathbf{q}_1}^{1,1}$	0.0000 +0.0000i	0.0000 +0.0000i	0.0000 +0.0000i	0.0000 +0.0000i	0.5063 -0.3963i	0.4684 -0.3012i	0.2388 +0.0243i
$w_{bt,4\mathbf{q}_1}^{3,0}$	0.0000 +0.0000i	0.0000 +0.0000i	0.0000 +0.0000i	0.0000 +0.0000i	-0.0910 +0.2194i	-0.6370 +0.4362i	-2.5286 +0.8760i
$w_{bt,4\mathbf{q}_1}^{2,1}$	0.0000 +0.0000i	0.0000 +0.0000i	0.0000 +0.0000i	0.0000 +0.0000i	0.0049 +0.5779i	0.0727 +1.1292i	0.6820 +2.6965i
$w_{bt,4\mathbf{q}_1}^{4,0}$	0.0000 +0.0000i	0.0000 +0.0000i	0.0000 +0.0000i	0.0000 +0.0000i	-0.2536 -0.1678i	-0.2972 +0.2576i	-0.6333 +2.6401i
$w_{bt,4\mathbf{q}_1}^{3,1}$	0.0000 +0.0000i	0.0000 +0.0000i	0.0000 +0.0000i	0.0000 +0.0000i	-6.7489 +0.3922i	-10.1463 -1.0346i	-17.4674 -7.3242i
$w_{bt,4\mathbf{q}_1}^{2,2}$	0.0000 +0.0000i	0.0000 +0.0000i	0.0000 +0.0000i	0.0000 +0.0000i	-7.2489 +1.0602i	-9.7566 -1.3110i	-14.3304 -9.7717i
$w_{bt,\mathbf{q}_1+2\mathbf{b}_{M_2}}^{0,0}$	0.0000 +0.0000i	0.0000 +0.0000i	0.0000 +0.0000i	0.0000 +0.0000i	-0.1448 +0.0267i	-0.1981 +0.0453i	-0.2921 +0.0718i
$w_{bt,\mathbf{q}_1+2\mathbf{b}_{M_2}}^{1,0}$	0.0000 +0.0000i	0.0000 +0.0000i	0.0000 +0.0000i	0.0000 +0.0000i	0.3902 +0.0613i	0.4334 +0.0473i	0.5154 -0.0053i
$w_{bt,\mathbf{q}_1+2\mathbf{b}_{M_2}}^{0,1}$	0.0000 +0.0000i	0.0000 +0.0000i	0.0000 +0.0000i	0.0000 +0.0000i	-0.1921 -0.1262i	-0.2336 -0.2507i	-0.3092 -0.4579i
$w_{bt,\mathbf{q}_1+2\mathbf{b}_{M_2}}^{2,0}$	0.0000 +0.0000i	0.0000 +0.0000i	0.0000 +0.0000i	0.0000 +0.0000i	1.7833 -0.6421i	2.3030 -0.9038i	3.1379 -1.2689i
$w_{bt,\mathbf{q}_1+2\mathbf{b}_{M_2}}^{1,1}$	0.0000 +0.0000i	0.0000 +0.0000i	0.0000 +0.0000i	0.0000 +0.0000i	-0.6417 -0.0806i	-0.2065 -0.1760i	1.0023 -0.1372i
$w_{bt,\mathbf{q}_1+2\mathbf{b}_{M_2}}^{0,2}$	0.0000 +0.0000i	0.0000 +0.0000i	0.0000 +0.0000i	0.0000 +0.0000i	0.4202 +0.0835i	0.6137 +0.0425i	1.0711 -0.1346i
$w_{bt,\mathbf{q}_1+2\mathbf{b}_{M_2}}^{3,0}$	0.0000 +0.0000i	0.0000 +0.0000i	0.0000 +0.0000i	0.0000 +0.0000i	1.1056 -3.4688i	0.4592 -3.7794i	-1.2346 -4.7061i
$w_{bt,\mathbf{q}_1+2\mathbf{b}_{M_2}}^{2,1}$	0.0000 +0.0000i	0.0000 +0.0000i	0.0000 +0.0000i	0.0000 +0.0000i	-0.7401 +6.5375i	-0.3843 +7.5599i	0.9607 +7.0165i



TABLE V: Interlayer potential term parameters (meV) for the full model of  $t\text{MoTe}_2$  based on DFT with quick basis selection (continued)

Parameter	3.89°	3.48°	3.15°	2.88°	2.65°	2.45°	2.13°
$w_{bt, \mathbf{q}_1 + 2\mathbf{b}_{M_2}}^{1,2}$	0.0000 +0.0000i	0.0000 +0.0000i	0.0000 +0.0000i	0.0000 +0.0000i	-0.9515 -5.4310i	-2.4155 -4.2166i	-7.9847 -1.3062i
$w_{bt, \mathbf{q}_1 + 2\mathbf{b}_{M_2}}^{0,3}$	0.0000 +0.0000i	0.0000 +0.0000i	0.0000 +0.0000i	0.0000 +0.0000i	0.2557 +1.0803i	0.3891 +1.0425i	0.4879 +1.0382i
$w_{bt, \mathbf{q}_1 + 2\mathbf{b}_{M_2}}^{4,0}$	0.0000 +0.0000i	0.0000 +0.0000i	0.0000 +0.0000i	0.0000 +0.0000i	-3.7752 +0.1700i	-4.3731 +0.8765i	-6.9001 +4.0615i
$w_{bt, \mathbf{q}_1 + 2\mathbf{b}_{M_2}}^{3,1}$	0.0000 +0.0000i	0.0000 +0.0000i	0.0000 +0.0000i	0.0000 +0.0000i	-1.1983 +7.1221i	-2.8833 +6.5701i	-7.3128 +4.4594i
$w_{bt, \mathbf{q}_1 + 2\mathbf{b}_{M_2}}^{2,2}$	0.0000 +0.0000i	0.0000 +0.0000i	0.0000 +0.0000i	0.0000 +0.0000i	-14.5291 +7.0074i	-18.0649 +10.4083i	-21.9038 +26.8069i
$w_{bt, \mathbf{q}_1 + 2\mathbf{b}_{M_2}}^{1,3}$	0.0000 +0.0000i	0.0000 +0.0000i	0.0000 +0.0000i	0.0000 +0.0000i	7.4563 -3.9199i	8.0949 -8.1135i	12.5453 -20.1044i

TABLE VI: Kinetic term parameters ( $m_e$ ) for the reduced model of  $t\text{MoTe}_2$  based on DFT with quick basis selection

Parameter	3.89°	3.48°	3.15°	2.88°	2.65°	2.45°	2.13°
$m^{(1,1)}$	-0.6739	-0.6846	-0.6820	-0.6660	-0.6601	-0.6640	-0.6513

TABLE VII: Intralayer potential term parameters (meV) for the reduced model of  $t\text{MoTe}_2$  based on DFT with quick basis selection

Parameter	3.89°	3.48°	3.15°	2.88°	2.65°	2.45°	2.13°
$V_{b, \mathbf{b}_{M_1}}^{0,0}$	-0.1474 -3.7990i	0.1810 +4.0256i	0.2450 -3.5442i	0.2352 +3.2592i	0.2312 -2.9032i	0.2302 -2.5452i	0.2303 -1.7489i
$V_{b, \mathbf{b}_{M_1}}^{1,0}$	-0.6450 -9.6915i	-2.5276 -3.2638i	-3.7990 -12.6673i	-1.4631 -4.7335i	-3.5411 -12.9294i	-3.3860 -12.8630i	-3.1002 -12.3481i
$V_{b, \mathbf{b}_{M_1}}^{0,1}$	-0.8922 -2.5289i	-4.2681 +12.7805i	-1.6634 +4.1358i	-3.6963 +12.8945i	-1.2223 +5.2018i	-0.9589 +5.5725i	-0.5841 +5.9847i
$V_{b, \mathbf{b}_{M_1}}^{2,0}$	14.2448 -31.6143i	0.0000 +0.0000i	0.0000 +0.0000i	0.0000 +0.0000i	0.0000 +0.0000i	0.0000 +0.0000i	0.0000 +0.0000i
$V_{b, \mathbf{b}_{M_1}}^{1,1}$	9.1970 +9.8042i	0.0000 +0.0000i	0.0000 +0.0000i	0.0000 +0.0000i	0.0000 +0.0000i	0.0000 +0.0000i	0.0000 +0.0000i
$V_{b, \mathbf{b}_{M_1}}^{0,2}$	2.5861 +34.6600i	0.0000 +0.0000i	0.0000 +0.0000i	0.0000 +0.0000i	0.0000 +0.0000i	0.0000 +0.0000i	0.0000 +0.0000i
$V_{b, \mathbf{b}_{M_1}}^{3,0}$	-27.9727 +8.9876i	0.0000 +0.0000i	0.0000 +0.0000i	0.0000 +0.0000i	0.0000 +0.0000i	0.0000 +0.0000i	0.0000 +0.0000i
$V_{b, \mathbf{b}_{M_1}}^{2,1}$	-78.6727 +74.8538i	0.0000 +0.0000i	0.0000 +0.0000i	0.0000 +0.0000i	0.0000 +0.0000i	0.0000 +0.0000i	0.0000 +0.0000i
$V_{b, \mathbf{b}_{M_1} + \mathbf{b}_{M_2}}^{0,0}$	0.0000 +0.0000i	-0.3491 -0.0498i	-0.3048 +0.0659i	-0.3071 -0.1152i	-0.2976 +0.1504i	-0.2807 +0.1638i	-0.2373 +0.1771i
$V_{b, \mathbf{b}_{M_1} + \mathbf{b}_{M_2}}^{1,0}$	0.0000 +0.0000i	1.0559 -0.0820i	0.3239 -0.2559i	1.1389 +0.1447i	-0.0382 -0.9202i	-0.1885 -1.1541i	-0.4531 -1.5087i
$V_{b, \mathbf{b}_{M_1} + \mathbf{b}_{M_2}}^{0,1}$	0.0000 +0.0000i	0.2441 +0.1518i	1.1287 +0.0676i	0.1386 +0.6179i	1.1831 -0.3189i	1.2747 -0.4415i	1.4520 -0.6166i

TABLE VII: Intralayer potential term parameters (meV) for the reduced model of  $t\text{MoTe}_2$  based on DFT with quick basis selection (continued)

Parameter	3.89°	3.48°	3.15°	2.88°	2.65°	2.45°	2.13°
$V_{b,2b_{M_1}}^{0,0}$	0.0000 +0.0000i	0.2984 +0.6746i	0.2392 -0.8461i	0.2300 +1.0886i	0.2024 -1.3096i	0.1645 -1.5046i	0.0972 -1.7472i
$V_{b,2b_{M_1}}^{1,0}$	0.0000 +0.0000i	-1.2971 +0.4366i	-0.7427 -3.4558i	-0.8665 +0.4128i	-1.0442 -4.8429i	-1.1822 -5.3805i	-1.4466 -6.1922i
$V_{b,2b_{M_1}}^{0,1}$	0.0000 +0.0000i	-0.5406 +3.0826i	-0.9209 -0.5155i	-0.9021 +4.1871i	-0.7092 -0.2800i	-0.4874 -0.1212i	-0.0272 +0.3074i
$V_{b,2b_{M_1}+b_{M_2}}^{0,0}$	0.0000 +0.0000i	0.0000 +0.0000i	0.0000 +0.0000i	0.0000 +0.0000i	0.0000 +0.0000i	-0.0585 +0.0898i	-0.0547 +0.0404i
$V_{b,2b_{M_1}+b_{M_2}}^{1,0}$	0.0000 +0.0000i	0.0000 +0.0000i	0.0000 +0.0000i	0.0000 +0.0000i	0.0000 +0.0000i	-0.2635 +0.1400i	-0.7803 +0.0470i
$V_{b,3b_{M_1}}^{0,0}$	0.0000 +0.0000i	0.0000 +0.0000i	0.0000 +0.0000i	0.0000 +0.0000i	0.0000 +0.0000i	0.0000 +0.0000i	0.0214 -0.8566i

 TABLE VIII: Interlayer potential term parameters (meV) for the reduced model of  $t\text{MoTe}_2$  based on DFT with quick basis selection

Parameter	3.89°	3.48°	3.15°	2.88°	2.65°	2.45°	2.13°
$w_{bt,\mathbf{q}_1}^{0,0}$	-1.3657 +0.4220i	-1.3448 -0.0242i	-1.1629 +0.2215i	-1.2461 +0.0360i	-1.0881 +0.1496i	-1.0445 +0.1200i	-0.9656 +0.0732i
$w_{bt,\mathbf{q}_1}^{1,0}$	3.8263 -2.7138i	2.8453 +2.3748i	3.3342 -2.2203i	3.6800 +2.0142i	3.9795 -1.8407i	4.2076 -1.6913i	4.6311 -1.6070i
$w_{bt,\mathbf{q}_1}^{2,0}$	35.3944 -4.3459i	0.0000 +0.0000i	0.0000 +0.0000i	0.0000 +0.0000i	0.0000 +0.0000i	0.0000 +0.0000i	0.0000 +0.0000i
$w_{bt,\mathbf{q}_1}^{1,1}$	-9.8408 -4.9173i	0.0000 +0.0000i	0.0000 +0.0000i	0.0000 +0.0000i	0.0000 +0.0000i	0.0000 +0.0000i	0.0000 +0.0000i
$w_{bt,\mathbf{q}_1}^{3,0}$	-22.3412 -5.4535i	0.0000 +0.0000i	0.0000 +0.0000i	0.0000 +0.0000i	0.0000 +0.0000i	0.0000 +0.0000i	0.0000 +0.0000i
$w_{bt,\mathbf{q}_1}^{2,1}$	-37.5948 +78.7889i	0.0000 +0.0000i	0.0000 +0.0000i	0.0000 +0.0000i	0.0000 +0.0000i	0.0000 +0.0000i	0.0000 +0.0000i
$w_{bt,-2\mathbf{q}_1}^{0,0}$	0.3823 +0.2358i	0.2845 -0.3131i	0.3269 +0.2325i	0.2671 -0.3085i	0.3159 +0.2278i	0.3073 +0.2176i	0.3020 +0.1955i
$w_{bt,-2\mathbf{q}_1}^{1,0}$	0.3601 +0.4737i	0.4518 -0.5269i	0.5385 +0.5095i	0.6289 -0.4561i	0.7196 +0.4097i	0.7983 +0.3665i	0.9493 +0.3684i
$w_{bt,-2\mathbf{q}_1}^{2,0}$	1.2703 +0.8752i	0.0000 +0.0000i	0.0000 +0.0000i	0.0000 +0.0000i	0.0000 +0.0000i	0.0000 +0.0000i	0.0000 +0.0000i
$w_{bt,-2\mathbf{q}_1}^{1,1}$	-1.4042 -1.0691i	0.0000 +0.0000i	0.0000 +0.0000i	0.0000 +0.0000i	0.0000 +0.0000i	0.0000 +0.0000i	0.0000 +0.0000i
$w_{bt,-2\mathbf{q}_1}^{3,0}$	-0.2315 +5.9180i	0.0000 +0.0000i	0.0000 +0.0000i	0.0000 +0.0000i	0.0000 +0.0000i	0.0000 +0.0000i	0.0000 +0.0000i
$w_{bt,\mathbf{q}_1+b_{M_2}}^{0,0}$	0.0000 +0.0000i	-0.5372 -0.0874i	-0.5819 +0.0814i	-0.6653 -0.0716i	-0.7294 +0.0516i	-0.7771 +0.0271i	-0.8435 -0.0253i
$w_{bt,\mathbf{q}_1+b_{M_2}}^{1,0}$	0.0000 +0.0000i	0.1092 +0.6278i	0.5522 -0.4672i	0.4275 +0.5308i	0.5337 -0.2817i	0.4850 -0.1095i	0.3837 +0.3249i
$w_{bt,\mathbf{q}_1+b_{M_2}}^{0,1}$	0.0000 +0.0000i	0.5161 +0.5348i	0.2481 -0.5728i	0.5565 +0.4080i	0.6165 -0.4131i	0.7994 -0.2404i	1.1008 +0.1365i

TABLE VIII: Interlayer potential term parameters (meV) for the reduced model of  $t\text{MoTe}_2$  based on DFT with quick basis selection (continued)

Parameter	3.89°	3.48°	3.15°	2.88°	2.65°	2.45°	2.13°
$w_{bt,2\mathbf{b}_{M_2}+\mathbf{q}_3}^{0,0}$	0.0000 +0.0000i	0.0000 +0.0000i	0.1381 +0.0810i	0.0000 +0.0000i	0.1746 +0.1566i	0.1843 +0.1841i	0.2000 +0.2179i
$w_{bt,2\mathbf{b}_{M_2}+\mathbf{q}_3}^{1,0}$	0.0000 +0.0000i	0.0000 +0.0000i	-0.0443 -0.0149i	0.0000 +0.0000i	-0.0294 -0.1659i	-0.0274 -0.2434i	-0.0681 -0.3550i
$w_{bt,2\mathbf{b}_{M_2}+\mathbf{q}_3}^{0,1}$	0.0000 +0.0000i	0.0000 +0.0000i	0.0725 -0.3024i	0.0000 +0.0000i	0.0965 -0.4386i	0.1066 -0.5037i	0.1731 -0.6399i

TABLE IX: Kinetic term parameters ( $m_e$ ) for the full model of  $t\text{MoTe}_2$  based on DFT with standard basis selection

Parameter	3.89°	3.48°	3.15°	2.88°	2.65°	2.45°	2.13°
$m^{(1,1)}$	-0.6290	-0.6119	-0.6065	-0.6063	-0.6050	-0.6296	-0.6142
$m^{(3,0)}$	1.3947	1.3256	1.3514	1.3225	1.2931	1.5681	1.4665
$m^{(2,2)}$	0.0701	0.0622	0.0604	0.0581	0.0567	0.0749	0.0646
$m^{(4,1)}$	-0.1323	-0.1116	-0.1208	-0.1086	-0.0982	-0.2311	-0.1845
$m^{(3,3)}$	-0.0111	-0.0080	-0.0077	-0.0065	-0.0058	-0.0164	-0.0104
$m^{(6,0)}$	12.6650	-2.0632	0.4985	0.4344	0.4296	0.9395	0.4309
$m^{(5,2)}$	0.0267	0.0188	0.0224	0.0176	0.0141	0.0000	0.0000
$m^{(4,4)}$	0.0030	0.0016	0.0016	0.0011	0.0009	0.0000	0.0000
$m^{(7,1)}$	0.1481	0.0438	-0.0433	-0.0332	-0.0323	0.0000	0.0000
$m^{(6,3)}$	-0.0140	-0.0079	-0.0106	-0.0071	-0.0048	0.0000	0.0000
$m^{(9,0)}$	-3.2103	-2.2691	-6.4626	-6.7820	-9.6389	0.0000	0.0000
$m^{(5,5)}$	-0.0018	-0.0007	-0.0008	-0.0005	-0.0003	0.0000	0.0000
$m^{(8,2)}$	-0.0273	-0.0077	0.0143	0.0097	0.0099	0.0000	0.0000

TABLE X: Intralayer potential term parameters (meV) for the full model of  $t\text{MoTe}_2$  based on DFT with standard basis selection

Parameter	3.89°	3.48°	3.15°	2.88°	2.65°	2.45°	2.13°
$V_{b,b_{M_1}}^{0,0}$	-0.1200 -3.5940i	-0.1132 +3.9385i	-0.0315 -3.4708i	-0.1023 +2.9937i	-0.0271 -2.7491i	-0.0347 -2.3510i	-0.0426 -1.5803i
$V_{b,b_{M_1}}^{1,0}$	-1.3330 -9.8741i	-0.7287 +3.9900i	-1.2982 -10.7303i	0.5266 -1.4880i	-1.0359 -11.1370i	-0.8939 -11.0962i	-1.0495 -10.6338i
$V_{b,b_{M_1}}^{0,1}$	-0.7285 -4.5535i	-1.6397 +11.6200i	-0.0933 -2.2851i	-1.0684 +10.8185i	-0.2432 -0.3291i	-0.2922 +0.4577i	0.1723 +1.8129i
$V_{b,b_{M_1}}^{2,0}$	-0.1693 -35.5222i	-2.3608 -45.9456i	3.3932 -42.1345i	0.3988 -29.8951i	2.3535 -44.6941i	1.7688 -44.9749i	1.8275 -44.6072i
$V_{b,b_{M_1}}^{1,1}$	2.5042 +11.1474i	2.2974 -14.0014i	1.7774 +15.4316i	3.2775 -8.6276i	-0.5137 +18.8286i	-1.5088 +19.8503i	-4.0348 +28.8148i
$V_{b,b_{M_1}}^{0,2}$	-1.3478 +36.7777i	-1.0718 +42.7901i	1.8324 +44.5211i	0.5466 +25.3219i	1.6131 +48.0321i	1.6205 +48.4464i	0.1358 +44.7863i

TABLE X: Intralayer potential term parameters (meV) for the full model of  $t\text{MoTe}_2$  based on DFT with standard basis selection (continued)

Parameter	3.89°	3.48°	3.15°	2.88°	2.65°	2.45°	2.13°
$V_{b,b_{M_1}}^{3,0}$	6.4450 -14.4462i	14.8206 -44.9263i	-0.6943 -8.4729i	8.5615 -3.8641i	2.9153 -10.0510i	5.4140 -10.5338i	-1.9079 -0.8134i
$V_{b,b_{M_1}}^{-2,1}$	3.6725 +80.6102i	0.5092 -88.6333i	10.1076 +79.2253i	-17.4404 -4.7603i	6.7047 +102.7439i	3.3792 +110.2733i	33.3025 +100.8985i
$V_{b,b_{M_1}}^{1,2}$	-2.4782 +88.1108i	14.4298 -115.5473i	-5.0895 +88.2799i	4.8839 -56.9779i	8.3104 +75.3297i	16.8978 +68.4568i	0.1826 +47.3600i
$V_{b,b_{M_1}}^{0,3}$	10.7772 +39.7510i	9.0930 +18.2980i	-2.0822 +30.7567i	-1.6744 -3.2533i	-5.4341 +29.1373i	-8.0768 +27.9729i	2.0920 +19.1344i
$V_{b,b_{M_1}}^{4,0}$	17.2675 -11.0916i	21.4020 +38.7871i	7.8501 -2.6960i	0.0000 +0.0000i	18.4758 -13.3750i	26.3712 -21.6318i	1.0586 -44.1141i
$V_{b,b_{M_1}}^{3,1}$	28.7037 +246.1192i	68.5484 +375.7886i	-76.8126 +329.7861i	0.0000 +0.0000i	-71.7141 +385.1938i	-61.2588 +401.8266i	-89.6626 +370.7658i
$V_{b,b_{M_1}}^{2,2}$	-43.1685 -71.5988i	-64.8863 +95.5996i	-74.2962 -88.8969i	0.0000 +0.0000i	-73.4564 -148.4809i	-72.2377 -185.1059i	-3.5437 -533.6777i
$V_{b,b_{M_1}}^{1,3}$	42.9966 -269.5526i	46.4081 -323.5813i	-43.3210 -344.7707i	0.0000 +0.0000i	-60.4471 -408.2632i	-75.1984 -421.8169i	-10.9806 -298.8536i
$V_{b,b_{M_1}}^{0,4}$	14.9738 -26.4242i	21.6684 +16.2978i	19.8021 -39.5864i	0.0000 +0.0000i	26.0107 -46.0040i	28.2158 -46.1160i	19.5446 -27.4037i
$V_{b,b_{M_1}}^{5,0}$	-32.9952 -46.0023i	-46.2393 -77.9979i	-33.1386 -21.8038i	0.0000 +0.0000i	-43.4033 -11.0155i	-46.0208 +3.5017i	0.0000 +0.0000i
$V_{b,b_{M_1}}^{4,1}$	-121.2696 +59.7347i	-285.6348 +114.1302i	42.8973 -75.8056i	0.0000 +0.0000i	-76.1903 -28.6310i	-202.2686 +23.0414i	0.0000 +0.0000i
$V_{b,b_{M_1}}^{-3,2}$	65.7909 -583.3844i	54.9187 -261.3387i	238.5659 -594.7679i	0.0000 +0.0000i	390.4237 -790.2523i	498.9101 -833.3176i	0.0000 +0.0000i
$V_{b,b_{M_1}}^{2,3}$	53.9420 +111.7753i	20.5806 +948.9492i	250.8876 -1.2457i	0.0000 +0.0000i	199.8471 -32.3467i	128.2047 -81.3933i	0.0000 +0.0000i
$V_{b,b_{M_1}}^{1,4}$	-165.7008 -112.4541i	-201.7701 -107.0928i	10.0016 +20.8845i	0.0000 +0.0000i	102.4349 +51.5375i	202.2072 +49.5957i	0.0000 +0.0000i
$V_{b,b_{M_1}}^{0,5}$	-30.2390 +52.2124i	-49.1196 +62.6477i	-57.5598 +45.0642i	0.0000 +0.0000i	-93.3766 +50.6151i	-116.5517 +44.7985i	0.0000 +0.0000i
$V_{b,b_{M_1}+b_{M_2}}^{0,0}$	-0.2213 -0.0583i	-0.2044 -0.0377i	-0.1238 +0.0113i	-0.0920 -0.0561i	-0.0655 +0.0645i	-0.0421 +0.0670i	-0.0108 +0.0675i
$V_{b,b_{M_1}+b_{M_2}}^{1,0}$	0.6618 -0.3893i	0.6875 -0.7637i	0.2732 -0.4434i	0.4302 -0.4577i	-0.1650 -0.6168i	-0.2450 -0.6337i	-0.3210 -0.6244i
$V_{b,b_{M_1}+b_{M_2}}^{0,1}$	0.7284 +0.7318i	0.0967 +0.4221i	0.7104 +0.6782i	-0.1738 +0.5948i	0.3745 +0.3791i	0.2937 +0.3172i	0.0649 +0.2581i
$V_{b,b_{M_1}+b_{M_2}}^{-2,0}$	-3.0555 +3.4279i	-2.7375 +0.9363i	-0.3324 +0.1538i	-0.1643 -0.0784i	0.9883 -0.7838i	1.2642 -1.1498i	1.8439 -1.0000i
$V_{b,b_{M_1}+b_{M_2}}^{1,1}$	5.1820 +6.5369i	4.9845 +2.9468i	1.9605 +1.3323i	2.0714 -0.3073i	1.7935 +0.3640i	1.4757 +0.2314i	1.5360 +0.1833i
$V_{b,b_{M_1}+b_{M_2}}^{0,2}$	1.3894 -0.1356i	1.1662 -0.1222i	-1.5996 +0.5784i	0.3211 -0.2902i	-1.1393 +1.7052i	-1.0436 +2.1806i	1.0430 -0.0116i
$V_{b,b_{M_1}+b_{M_2}}^{-3,0}$	-9.2851 +2.8973i	-9.9527 +6.1223i	-0.6308 +1.2943i	0.4732 +0.4620i	0.3772 +2.1540i	0.5595 +2.3972i	0.7935 +1.2103i
$V_{b,b_{M_1}+b_{M_2}}^{-2,1}$	-4.3685 +7.6508i	-7.5625 +11.5311i	-3.6658 +3.4930i	-2.4615 +2.8360i	-5.0242 +2.1991i	-7.9500 +0.4045i	-17.0554 -5.3391i

TABLE X: Intralayer potential term parameters (meV) for the full model of  $t\text{MoTe}_2$  based on DFT with standard basis selection (continued)

Parameter	3.89°	3.48°	3.15°	2.88°	2.65°	2.45°	2.13°
$V_{b,b_{M_1}+b_{M_2}}^{1,2}$	-12.7496 -14.3880i	-8.7934 -10.3297i	-4.3293 -7.9322i	3.1602 -4.3042i	-3.4126 -5.5604i	-2.8453 -5.6562i	-0.7553 -6.7358i
$V_{b,b_{M_1}+b_{M_2}}^{0,3}$	-11.2494 -1.4275i	-11.5428 -0.1608i	-1.3096 -4.2838i	0.5456 +0.9930i	-0.6465 -4.1436i	-0.7286 -4.3953i	-1.2989 -3.9352i
$V_{b,b_{M_1}+b_{M_2}}^{4,0}$	54.4414 +3.5247i	52.8580 +29.2062i	-10.2595 -1.0025i	0.0000 +0.0000i	-16.3463 +6.4193i	-19.5463 +12.7662i	14.2580 -19.7599i
$V_{b,b_{M_1}+b_{M_2}}^{3,1}$	102.7684 -143.2248i	162.4789 -110.5936i	-0.0022 +20.2548i	0.0000 +0.0000i	-0.5756 +56.9231i	9.3517 +80.0673i	6.3406 +49.2744i
$V_{b,b_{M_1}+b_{M_2}}^{2,2}$	-106.9212 -117.0538i	-77.2099 -118.8385i	10.3519 +0.5040i	0.0000 +0.0000i	64.9132 +9.3126i	108.2052 +11.7091i	95.3940 -0.2787i
$V_{b,b_{M_1}+b_{M_2}}^{1,3}$	6.1731 +27.9308i	11.8700 +22.8400i	46.5338 -20.9527i	0.0000 +0.0000i	69.3055 -63.9529i	86.9205 -92.6545i	-30.2834 +84.9657i
$V_{b,b_{M_1}+b_{M_2}}^{0,4}$	10.7551 -8.6097i	17.6212 -8.4177i	0.8281 -3.9831i	0.0000 +0.0000i	-0.8408 -10.6146i	-2.6656 -14.8991i	2.7670 -7.4295i
$V_{b,b_{M_1}+b_{M_2}}^{5,0}$	-44.2315 -24.1682i	-27.9372 -47.6098i	13.6453 +9.7768i	0.0000 +0.0000i	35.9839 +2.2545i	52.9791 -5.5017i	0.0000 +0.0000i
$V_{b,b_{M_1}+b_{M_2}}^{4,1}$	-206.4082 +100.2551i	-307.5329 -36.2942i	57.7504 -62.1385i	0.0000 +0.0000i	80.7858 -180.0354i	83.5915 -274.2216i	0.0000 +0.0000i
$V_{b,b_{M_1}+b_{M_2}}^{3,2}$	31.6032 +382.2228i	-83.6707 +437.5019i	7.2278 -46.4362i	0.0000 +0.0000i	-53.5418 -113.4285i	-103.4426 -142.7987i	0.0000 +0.0000i
$V_{b,b_{M_1}+b_{M_2}}^{2,3}$	221.8514 +29.7514i	190.7511 +65.7322i	-94.7375 +21.8263i	0.0000 +0.0000i	-290.0782 +113.1498i	-459.9306 +197.3040i	0.0000 +0.0000i
$V_{b,b_{M_1}+b_{M_2}}^{1,4}$	0.0000 +0.0000i	0.0000 +0.0000i	-35.0468 +92.4017i	0.0000 +0.0000i	-40.3553 +215.8528i	-38.8696 +314.6228i	0.0000 +0.0000i
$V_{b,2b_{M_1}}^{0,0}$	0.1080 -0.3446i	0.1213 +0.6310i	0.0855 -0.7720i	0.0394 +1.0005i	0.0663 -1.2006i	0.0480 -1.3780i	0.0296 -1.6195i
$V_{b,2b_{M_1}}^{1,0}$	0.4523 -0.7325i	-0.2835 +2.3858i	0.0024 -1.9509i	-0.2683 +2.2328i	-0.1509 -3.0536i	-0.1635 -3.5293i	-0.2579 -4.2449i
$V_{b,2b_{M_1}}^{0,1}$	-0.2014 -1.2353i	0.5056 +1.6322i	-0.2390 -2.6466i	-0.0171 +2.6892i	-0.1728 -3.2564i	-0.1210 -3.3635i	-0.0144 -3.2084i
$V_{b,2b_{M_1}}^{2,0}$	2.7247 -3.4719i	1.3069 -3.4591i	0.1526 -8.5461i	-0.6896 -6.6547i	0.0728 -13.6184i	-0.1424 -15.9451i	0.1209 -19.8963i
$V_{b,2b_{M_1}}^{1,1}$	-0.4734 -4.0188i	-4.6397 +0.0079i	-3.3769 -3.9492i	0.6253 +1.7377i	-3.7933 -2.8050i	-4.0754 -2.0211i	-5.2884 +1.3923i
$V_{b,2b_{M_1}}^{0,2}$	-0.9239 -1.2222i	-1.1551 +7.4309i	0.3600 +3.2484i	-0.4813 +8.1466i	0.5987 +7.9706i	0.5647 +10.4984i	-0.1727 +14.6493i
$V_{b,2b_{M_1}}^{3,0}$	-11.5191 -2.5283i	-11.5218 +7.0494i	8.2046 -6.2844i	4.5562 -5.2084i	9.3676 -7.2751i	8.8347 -6.5865i	0.1662 -6.4488i
$V_{b,2b_{M_1}}^{2,1}$	-25.2588 +5.3427i	-16.6814 -21.4245i	13.2417 +17.9087i	-4.4923 -19.9809i	16.7406 +38.8199i	15.5192 +51.1041i	25.1496 +61.4634i
$V_{b,2b_{M_1}}^{1,2}$	-7.6815 +34.1813i	2.9652 -5.2930i	-1.8307 +59.6010i	-3.8624 -22.5142i	-5.5400 +86.6056i	-6.4123 +96.6025i	2.2314 +112.3593i
$V_{b,2b_{M_1}}^{0,3}$	0.9616 +14.8246i	16.0974 +3.2282i	-1.2783 +17.8196i	3.3846 +0.8297i	-3.6471 +24.3206i	-5.1164 +25.7751i	-5.0322 +26.7302i
$V_{b,2b_{M_1}}^{4,0}$	45.8426 -5.9630i	27.3075 -85.6825i	-16.4027 +7.8988i	0.0000 +0.0000i	-19.0623 +1.5049i	-17.8356 -5.3355i	6.4953 -18.4356i

TABLE X: Intralayer potential term parameters (meV) for the full model of  $t\text{MoTe}_2$  based on DFT with standard basis selection (continued)

Parameter	3.89°	3.48°	3.15°	2.88°	2.65°	2.45°	2.13°
$V_{b,2b_{M_1}}^{3,1}$	61.6927 +9.4053i	31.0538 -77.5901i	-61.2772 +71.6535i	0.0000 +0.0000i	-75.0627 +88.2338i	-67.2013 +89.4412i	-64.6562 +150.2005i
$V_{b,2b_{M_1}}^{2,2}$	29.6602 -13.5495i	50.1356 +39.1185i	-22.4811 -58.5188i	0.0000 +0.0000i	-11.0875 -130.5717i	17.8921 -171.2557i	-2.9255 -260.7484i
$V_{b,2b_{M_1}}^{1,3}$	11.4730 -46.5942i	-45.3383 -62.0918i	-4.4918 -94.8331i	0.0000 +0.0000i	4.3681 -161.9530i	17.5182 -190.3169i	15.5106 -223.5040i
$V_{b,2b_{M_1}}^{0,4}$	-1.6283 -10.3358i	-18.7456 +10.1103i	4.6991 -6.6937i	0.0000 +0.0000i	9.5014 -10.4267i	12.3342 -10.7016i	16.4123 -10.9080i
$V_{b,2b_{M_1}}^{5,0}$	-38.6101 -7.1203i	-37.9268 +86.3706i	12.7392 -26.8981i	0.0000 +0.0000i	16.9744 -41.3791i	20.5000 -43.4908i	0.0000 +0.0000i
$V_{b,2b_{M_1}}^{4,1}$	-118.9616 +41.4821i	9.6347 +287.1939i	42.5221 -33.5930i	0.0000 +0.0000i	33.7783 +7.2486i	8.3552 +42.1335i	0.0000 +0.0000i
$V_{b,2b_{M_1}}^{3,2}$	0.0000 +0.0000i	0.0000 +0.0000i	47.5010 -53.5081i	0.0000 +0.0000i	52.3922 -42.4642i	20.1245 -31.7937i	0.0000 +0.0000i
$V_{b,2b_{M_1}}^{2,3}$	0.0000 +0.0000i	0.0000 +0.0000i	72.9427 +67.9534i	0.0000 +0.0000i	94.6415 +109.8446i	35.3180 +115.3457i	0.0000 +0.0000i
$V_{b,2b_{M_1}+b_{M_2}}^{0,0}$	-0.0646 -0.0137i	-0.0621 -0.0105i	-0.0761 +0.0363i	-0.0616 -0.0524i	0.0000 +0.0000i	-0.0425 +0.0727i	-0.0309 +0.0555i
$V_{b,2b_{M_1}+b_{M_2}}^{1,0}$	0.1498 +0.0588i	0.0720 -0.1092i	0.3331 +0.0747i	0.2291 -0.3574i	0.0000 +0.0000i	0.0003 -0.0711i	-0.2373 -0.2140i
$V_{b,2b_{M_1}+b_{M_2}}^{0,1}$	0.0475 +0.0994i	0.1702 -0.0317i	0.2872 +0.3339i	0.2043 -0.1311i	0.0000 +0.0000i	0.1836 +0.3178i	0.0331 +0.2080i
$V_{b,2b_{M_1}+b_{M_2}}^{2,0}$	-0.2576 -0.0811i	0.8302 -1.9223i	-0.7545 +0.9113i	-0.2825 +0.1494i	0.0000 +0.0000i	0.6415 +0.8074i	1.6494 +0.8838i
$V_{b,2b_{M_1}+b_{M_2}}^{1,1}$	0.1564 +0.5412i	-0.2531 -2.8139i	0.8551 +1.1317i	-0.1239 -0.6136i	0.0000 +0.0000i	2.7789 +0.2047i	4.6919 +1.4667i
$V_{b,2b_{M_1}+b_{M_2}}^{0,2}$	0.5298 +0.3648i	-0.8864 -1.0653i	0.3175 +0.3493i	-0.5968 -0.9755i	0.0000 +0.0000i	0.4079 +0.1838i	0.8401 +0.4729i
$V_{b,2b_{M_1}+b_{M_2}}^{3,0}$	-2.6937 -0.0911i	-4.5543 +5.4902i	0.1739 +2.5823i	-0.0861 +0.9941i	0.0000 +0.0000i	-1.1873 +7.4308i	-0.2330 -0.5732i
$V_{b,2b_{M_1}+b_{M_2}}^{2,1}$	-1.5492 +4.2276i	-0.4265 +15.1471i	-5.4775 +4.6577i	1.1134 +2.9447i	0.0000 +0.0000i	-10.4170 +10.9195i	-19.3355 -9.5795i
$V_{b,2b_{M_1}+b_{M_2}}^{1,2}$	0.7946 -1.6439i	2.3747 +6.1787i	-7.6250 -4.5023i	0.6191 +1.8589i	0.0000 +0.0000i	-15.9206 -2.4058i	-21.6061 -12.1474i
$V_{b,2b_{M_1}+b_{M_2}}^{0,3}$	-0.9697 -0.6687i	0.3772 +0.1842i	-2.3083 -1.8973i	0.5796 +0.2384i	0.0000 +0.0000i	-2.8231 -1.7530i	-1.7663 -2.6237i
$V_{b,2b_{M_1}+b_{M_2}}^{4,0}$	1.3747 +1.6718i	5.3020 -2.3513i	0.7909 -7.2398i	0.0000 +0.0000i	0.0000 +0.0000i	15.1442 -27.4679i	0.1696 -7.0750i
$V_{b,2b_{M_1}+b_{M_2}}^{3,1}$	9.7192 -5.3914i	7.2743 -16.3216i	10.9398 -41.1597i	0.0000 +0.0000i	0.0000 +0.0000i	3.6437 -111.8090i	9.9956 +21.0503i
$V_{b,2b_{M_1}+b_{M_2}}^{2,2}$	-2.4672 -5.9576i	-3.6379 -15.5942i	9.0278 -19.5683i	0.0000 +0.0000i	0.0000 +0.0000i	18.3629 -42.0122i	66.2583 +26.9218i
$V_{b,2b_{M_1}+b_{M_2}}^{1,3}$	0.0000 +0.0000i	0.0000 +0.0000i	15.4778 +3.0158i	0.0000 +0.0000i	0.0000 +0.0000i	33.3955 +1.9330i	24.6542 +24.9548i
$V_{b,2b_{M_1}+b_{M_2}}^{5,0}$	0.0000 +0.0000i	0.0000 +0.0000i	-4.3780 +5.0989i	0.0000 +0.0000i	0.0000 +0.0000i	-31.0444 +14.5186i	0.0000 +0.0000i

TABLE X: Intralayer potential term parameters (meV) for the full model of  $t\text{MoTe}_2$  based on DFT with standard basis selection (continued)

Parameter	3.89°	3.48°	3.15°	2.88°	2.65°	2.45°	2.13°
$V_{b,2b_{M_1}+b_{M_2}}^{4,1}$	0.0000 +0.0000i	0.0000 +0.0000i	-12.2634 +44.1086i	0.0000 +0.0000i	0.0000 +0.0000i	-44.7745 +180.5112i	0.0000 +0.0000i
$V_{b,2b_{M_1}+b_{M_2}}^{3,2}$	0.0000 +0.0000i	0.0000 +0.0000i	13.3627 +74.8523i	0.0000 +0.0000i	0.0000 +0.0000i	90.4236 +232.2229i	0.0000 +0.0000i
$V_{b,3b_{M_1}}^{0,0}$	0.0000 +0.0000i	0.0000 +0.0000i	0.0000 +0.0000i	0.0000 +0.0000i	0.0000 +0.0000i	0.0637 -0.3073i	0.0475 -0.4886i
$V_{b,3b_{M_1}}^{1,0}$	0.0000 +0.0000i	0.0000 +0.0000i	0.0000 +0.0000i	0.0000 +0.0000i	0.0000 +0.0000i	-0.2551 -0.2449i	-0.1654 -1.1361i
$V_{b,3b_{M_1}}^{0,1}$	0.0000 +0.0000i	0.0000 +0.0000i	0.0000 +0.0000i	0.0000 +0.0000i	0.0000 +0.0000i	-0.3923 -1.2101i	-0.0114 -1.7204i
$V_{b,3b_{M_1}}^{2,0}$	0.0000 +0.0000i	0.0000 +0.0000i	0.0000 +0.0000i	0.0000 +0.0000i	0.0000 +0.0000i	3.8178 -9.7568i	5.0553 -6.2578i
$V_{b,3b_{M_1}}^{1,1}$	0.0000 +0.0000i	0.0000 +0.0000i	0.0000 +0.0000i	0.0000 +0.0000i	0.0000 +0.0000i	5.5690 -3.1451i	0.7839 -0.0093i
$V_{b,3b_{M_1}}^{0,2}$	0.0000 +0.0000i	0.0000 +0.0000i	0.0000 +0.0000i	0.0000 +0.0000i	0.0000 +0.0000i	0.0317 +2.3793i	-1.2624 +3.2118i
$V_{b,3b_{M_1}}^{3,0}$	0.0000 +0.0000i	0.0000 +0.0000i	0.0000 +0.0000i	0.0000 +0.0000i	0.0000 +0.0000i	2.7122 +37.6487i	-15.0680 +5.1913i
$V_{b,3b_{M_1}}^{2,1}$	0.0000 +0.0000i	0.0000 +0.0000i	0.0000 +0.0000i	0.0000 +0.0000i	0.0000 +0.0000i	-46.1041 +36.9773i	-31.9225 +2.9732i
$V_{b,3b_{M_1}}^{1,2}$	0.0000 +0.0000i	0.0000 +0.0000i	0.0000 +0.0000i	0.0000 +0.0000i	0.0000 +0.0000i	-16.7720 +1.2533i	-7.8946 +13.6061i
$V_{b,3b_{M_1}}^{0,3}$	0.0000 +0.0000i	0.0000 +0.0000i	0.0000 +0.0000i	0.0000 +0.0000i	0.0000 +0.0000i	2.3596 +3.2405i	3.7292 +5.1543i
$V_{b,3b_{M_1}}^{4,0}$	0.0000 +0.0000i	0.0000 +0.0000i	0.0000 +0.0000i	0.0000 +0.0000i	0.0000 +0.0000i	-42.8890 -101.5828i	15.7182 -24.8134i
$V_{b,3b_{M_1}}^{3,1}$	0.0000 +0.0000i	0.0000 +0.0000i	0.0000 +0.0000i	0.0000 +0.0000i	0.0000 +0.0000i	34.4216 -159.2768i	36.0774 +31.3855i
$V_{b,3b_{M_1}}^{2,2}$	0.0000 +0.0000i	0.0000 +0.0000i	0.0000 +0.0000i	0.0000 +0.0000i	0.0000 +0.0000i	77.0322 +20.9754i	61.3903 +7.6516i
$V_{b,3b_{M_1}}^{5,0}$	0.0000 +0.0000i	0.0000 +0.0000i	0.0000 +0.0000i	0.0000 +0.0000i	0.0000 +0.0000i	53.4503 +50.4854i	0.0000 +0.0000i
$V_{b,3b_{M_1}}^{4,1}$	0.0000 +0.0000i	0.0000 +0.0000i	0.0000 +0.0000i	0.0000 +0.0000i	0.0000 +0.0000i	47.4588 +321.1803i	0.0000 +0.0000i

TABLE XI: Interlayer potential term parameters (meV) for the full model of  $t\text{MoTe}_2$  based on DFT with standard selection

Parameter	3.89°	3.48°	3.15°	2.88°	2.65°	2.45°	2.13°
$w_{bt,\mathbf{q}_1}^{0,0}$	-1.5294 +0.4806i	-1.7639 -0.1428i	-1.2961 +0.3248i	-1.5731 -0.0740i	-1.1882 +0.2384i	-1.1329 +0.2051i	-1.0280 +0.1502i
$w_{bt,\mathbf{q}_1}^{1,0}$	3.4444 -1.8623i	3.2432 +7.8920i	3.6652 -2.2542i	3.7670 +6.3924i	4.0707 -2.0912i	4.2463 -2.0093i	4.4565 -1.8084i
$w_{bt,\mathbf{q}_1}^{2,0}$	41.2787 -4.6185i	40.6596 -1.2708i	43.4659 -1.5015i	30.6718 +1.5089i	44.9943 -0.4453i	45.6129 -0.0338i	46.5930 +1.1415i

TABLE XI: Interlayer potential term parameters (meV) for the full model of  $t\text{MoTe}_2$  based on DFT with standard selection (continued)

Parameter	3.89°	3.48°	3.15°	2.88°	2.65°	2.45°	2.13°
$w_{bt,\mathbf{q}_1}^{1,1}$	1.0860 -6.6119i	5.0733 -1.1683i	-2.4607 -3.9865i	3.1456 -1.7752i	-1.2311 -3.3883i	-0.9171 -3.1607i	-0.2623 -2.6906i
$w_{bt,\mathbf{q}_1}^{3,0}$	-34.0472 +8.2111i	-40.2516 +16.3390i	-32.7332 +7.0471i	-20.8656 +4.7666i	-34.1349 +5.2250i	-34.4262 +4.5796i	-25.3541 +3.4457i
$w_{bt,\mathbf{q}_1}^{2,1}$	-51.9047 +8.9135i	-48.7946 -38.9820i	-61.5625 +33.2170i	-56.1823 -28.9836i	-66.2989 +29.9031i	-68.6334 +28.3180i	-70.0068 +19.2686i
$w_{bt,\mathbf{q}_1}^{4,0}$	20.5112 -34.5249i	45.3831 +1.8772i	42.2887 -32.4149i	0.0000 +0.0000i	56.3085 -32.6279i	61.7179 -31.5765i	73.6682 -22.0969i
$w_{bt,\mathbf{q}_1}^{3,1}$	-168.9318 +30.1334i	-200.6905 +45.5618i	-187.1690 -12.4060i	0.0000 +0.0000i	-201.5958 -24.3390i	-209.9127 -30.3776i	-221.7074 -60.9993i
$w_{bt,\mathbf{q}_1}^{2,2}$	-39.1033 +17.0882i	-29.8199 -7.7404i	2.9017 +0.5434i	0.0000 +0.0000i	-12.9325 -3.7315i	-19.6661 -4.6261i	-43.8817 -9.8840i
$w_{bt,\mathbf{q}_1}^{5,0}$	-35.5145 +31.1884i	-47.8112 -50.9732i	-17.6616 +27.7939i	0.0000 +0.0000i	-16.9192 +30.6084i	-13.6094 +32.1595i	0.0000 +0.0000i
$w_{bt,\mathbf{q}_1}^{4,1}$	232.5651 -3.1534i	264.1921 +23.6488i	198.2270 +13.5337i	0.0000 +0.0000i	229.9741 +15.1393i	240.7811 +12.1187i	0.0000 +0.0000i
$w_{bt,\mathbf{q}_1}^{3,2}$	101.3449 +20.6358i	-0.2863 -171.7486i	195.0445 -253.4979i	0.0000 +0.0000i	177.4068 -250.5947i	157.9674 -238.1958i	0.0000 +0.0000i
$w_{bt,-2\mathbf{q}_1}^{0,0}$	0.4093 +0.2010i	0.2870 -0.3043i	0.3690 +0.2175i	0.2341 -0.3130i	0.3702 +0.2197i	0.3659 +0.2126i	0.3745 +0.1940i
$w_{bt,-2\mathbf{q}_1}^{1,0}$	0.4104 +0.8454i	0.2570 -0.7151i	0.4712 +0.8943i	0.6081 -1.4109i	0.6023 +0.9005i	0.6629 +0.8883i	0.7936 +1.1203i
$w_{bt,-2\mathbf{q}_1}^{2,0}$	0.4561 -0.2261i	-2.1143 -1.8032i	2.2576 -0.5357i	-0.9243 -0.0316i	3.2116 -0.7898i	3.7514 -0.8758i	5.3890 -0.9904i
$w_{bt,-2\mathbf{q}_1}^{1,1}$	-0.6226 +1.2190i	-1.9425 +1.3895i	-0.4256 +0.9769i	0.3951 +1.6248i	-0.4405 +1.0020i	-0.4182 +1.1173i	-2.5638 +1.6754i
$w_{bt,-2\mathbf{q}_1}^{3,0}$	3.2638 +7.3432i	-1.3963 -8.7536i	-0.5173 +9.8974i	-1.6377 -6.0204i	-0.0818 +8.7299i	0.1435 +7.8930i	-0.9373 +3.7744i
$w_{bt,-2\mathbf{q}_1}^{2,1}$	-10.8365 +1.9210i	-4.9925 -4.1887i	-5.8466 -0.9985i	-5.8180 +13.1229i	-3.5895 -0.4631i	-2.2930 +0.1652i	-0.7779 -21.0123i
$w_{bt,-2\mathbf{q}_1}^{4,0}$	0.1816 +5.4950i	3.4200 -5.7293i	9.3892 +1.4396i	0.0000 +0.0000i	22.4417 +5.6246i	30.5116 +8.5558i	18.4334 +2.2011i
$w_{bt,-2\mathbf{q}_1}^{3,1}$	5.2388 +5.3153i	-4.8410 +24.4316i	-11.6297 +11.9477i	0.0000 +0.0000i	-15.1336 +8.3311i	-19.1575 +4.2537i	-24.4102 +6.5230i
$w_{bt,-2\mathbf{q}_1}^{2,2}$	-16.4675 -4.6547i	19.6455 +1.5399i	-17.7034 -11.2525i	0.0000 +0.0000i	-25.6358 -21.2955i	-31.0025 -29.1779i	-3.0893 -58.0776i
$w_{bt,-2\mathbf{q}_1}^{5,0}$	-12.7634 -1.3651i	-6.8136 +5.1938i	-13.8004 +15.7015i	0.0000 +0.0000i	-22.9221 +37.6554i	-30.2581 +54.3959i	0.0000 +0.0000i
$w_{bt,-2\mathbf{q}_1}^{4,1}$	-32.2619 -19.5441i	-32.7449 +11.4422i	-10.8708 -80.0715i	0.0000 +0.0000i	3.8407 -118.8627i	17.2340 -143.3116i	0.0000 +0.0000i
$w_{bt,-2\mathbf{q}_1}^{3,2}$	13.8840 -60.7258i	12.0253 +104.8919i	8.4810 -48.9438i	0.0000 +0.0000i	0.3022 -118.1329i	-11.2134 -170.1225i	0.0000 +0.0000i
$w_{bt,\mathbf{q}_1+\mathbf{b}_{M_2}}^{0,0}$	-0.4619 +0.1301i	-0.6789 -0.2023i	-0.7151 +0.2147i	-0.7882 -0.2422i	-0.8644 +0.2298i	-0.9081 +0.2269i	-0.9516 +0.2110i
$w_{bt,\mathbf{q}_1+\mathbf{b}_{M_2}}^{1,0}$	0.5450 +0.0373i	-0.4876 +1.4341i	0.7397 +0.0076i	-0.3837 +1.7106i	0.8718 -0.0605i	0.9415 -0.0937i	1.0181 -0.1830i



TABLE XI: Interlayer potential term parameters (meV) for the full model of  $t\text{MoTe}_2$  based on DFT with standard selection (continued)

Parameter	3.89°	3.48°	3.15°	2.88°	2.65°	2.45°	2.13°
$w_{bt, \mathbf{q}_1 + \mathbf{b}_{M_2}}^{0,1}$	-0.3558 -0.7682i	0.6355 -0.0064i	-0.4822 -1.6048i	0.8238 +0.1296i	-0.4406 -2.0248i	-0.4026 -2.1442i	-0.3215 -2.2204i
$w_{bt, \mathbf{q}_1 + \mathbf{b}_{M_2}}^{2,0}$	4.5512 -1.9861i	4.1920 -1.1226i	7.3202 -1.8114i	3.7956 -0.1873i	9.4721 -1.8600i	10.2939 -1.7677i	10.8859 -0.5176i
$w_{bt, \mathbf{q}_1 + \mathbf{b}_{M_2}}^{1,1}$	-1.1223 -0.0160i	-0.2981 +0.0819i	0.6026 -1.0427i	-0.5700 +3.3687i	1.0756 -1.5926i	1.2134 -1.6797i	2.6916 -2.8508i
$w_{bt, \mathbf{q}_1 + \mathbf{b}_{M_2}}^{0,2}$	2.0408 +0.5678i	6.6039 +2.2308i	4.5677 +0.6811i	6.8717 +0.7689i	6.2809 +0.8260i	6.9770 +0.8215i	7.0265 +0.9603i
$w_{bt, \mathbf{q}_1 + \mathbf{b}_{M_2}}^{3,0}$	-1.1361 -1.2161i	-4.6704 +3.0271i	-1.1490 -0.3012i	-1.6859 -0.9850i	-3.5120 -0.0964i	-4.8365 -0.1819i	-5.1468 +0.4534i
$w_{bt, \mathbf{q}_1 + \mathbf{b}_{M_2}}^{2,1}$	1.7868 +12.3915i	4.9950 -4.6410i	-4.6087 +12.3931i	-2.3818 -5.5674i	-6.5233 +16.8111i	-7.5437 +18.3268i	-9.3865 +20.9519i
$w_{bt, \mathbf{q}_1 + \mathbf{b}_{M_2}}^{1,2}$	2.9435 -0.6087i	-1.2514 -14.1928i	-0.5230 +7.3730i	-8.9491 -17.5239i	-1.2034 +11.0218i	-1.7739 +12.9301i	-2.1864 +17.2556i
$w_{bt, \mathbf{q}_1 + \mathbf{b}_{M_2}}^{0,3}$	-3.4226 -1.1156i	-1.4574 +1.7829i	-4.6034 -0.4170i	-2.2804 +5.0162i	-4.9432 -1.0828i	-4.8368 -1.3764i	-4.0035 -3.1215i
$w_{bt, \mathbf{q}_1 + \mathbf{b}_{M_2}}^{4,0}$	4.3701 +1.2766i	4.1935 -1.8959i	11.4271 -14.5644i	0.0000 +0.0000i	13.5210 -14.9312i	14.7352 -13.2552i	12.6883 -0.4083i
$w_{bt, \mathbf{q}_1 + \mathbf{b}_{M_2}}^{3,1}$	-27.3936 +13.7501i	-70.9840 -10.8334i	-53.3753 +14.4967i	0.0000 +0.0000i	-71.6149 +24.3187i	-80.8689 +28.6577i	-62.9920 -21.7104i
$w_{bt, \mathbf{q}_1 + \mathbf{b}_{M_2}}^{2,2}$	3.2468 -36.7215i	7.3435 +90.9770i	-20.2899 -42.6150i	0.0000 +0.0000i	-20.7706 -53.2395i	-15.2530 -60.5210i	-61.4597 -17.2715i
$w_{bt, \mathbf{q}_1 + \mathbf{b}_{M_2}}^{1,3}$	-19.9203 +20.0164i	-20.5918 -23.5796i	-49.7984 +10.4818i	0.0000 +0.0000i	-71.6531 +4.1311i	-85.1266 +0.6188i	-43.8658 -23.0009i
$w_{bt, \mathbf{q}_1 + \mathbf{b}_{M_2}}^{0,4}$	1.2017 -4.4587i	3.2580 +1.5196i	5.6684 -1.1215i	0.0000 +0.0000i	9.0889 -0.6728i	11.0753 -0.0629i	6.6952 -2.6693i
$w_{bt, \mathbf{q}_1 + \mathbf{b}_{M_2}}^{5,0}$	4.2886 -3.4613i	-6.6095 -0.3638i	-13.7409 -2.2751i	0.0000 +0.0000i	-10.2609 -3.9835i	-5.5951 -6.8906i	0.0000 +0.0000i
$w_{bt, \mathbf{q}_1 + \mathbf{b}_{M_2}}^{4,1}$	1.6969 +15.2989i	55.7745 +33.9411i	46.6446 +58.3150i	0.0000 +0.0000i	87.3580 +61.5207i	111.2099 +63.5642i	0.0000 +0.0000i
$w_{bt, \mathbf{q}_1 + \mathbf{b}_{M_2}}^{3,2}$	-67.8439 -51.4494i	133.3092 -149.6247i	-21.5076 -15.3240i	0.0000 +0.0000i	-60.5509 -50.3787i	-92.4694 -76.4789i	0.0000 +0.0000i
$w_{bt, \mathbf{q}_1 + \mathbf{b}_{M_2}}^{2,3}$	68.7264 +32.4333i	-160.5994 -2.2997i	119.8127 +25.6811i	0.0000 +0.0000i	137.1282 +69.4706i	143.7989 +113.8435i	0.0000 +0.0000i
$w_{bt, \mathbf{q}_1 + \mathbf{b}_{M_2}}^{1,4}$	0.0000 +0.0000i	0.0000 +0.0000i	40.3477 -51.5654i	0.0000 +0.0000i	48.8920 -81.5717i	46.1673 -104.0863i	0.0000 +0.0000i
$w_{bt, 2\mathbf{b}_{M_2} + \mathbf{q}_3}^{0,0}$	0.0832 -0.0290i	0.1395 -0.0041i	0.1305 +0.0168i	0.1472 -0.0483i	0.1717 +0.0757i	0.1845 +0.0968i	0.2029 +0.1264i
$w_{bt, 2\mathbf{b}_{M_2} + \mathbf{q}_3}^{1,0}$	0.0315 -0.0044i	0.2115 -0.1261i	-0.0127 +0.1133i	0.2973 +0.0266i	-0.0981 +0.1404i	-0.1440 +0.1564i	-0.1723 +0.1814i
$w_{bt, 2\mathbf{b}_{M_2} + \mathbf{q}_3}^{0,1}$	0.2338 +0.1404i	0.0398 -0.1250i	0.2222 +0.0819i	-0.0947 -0.0248i	0.2141 -0.0127i	0.2222 -0.0643i	0.2381 -0.1172i
$w_{bt, 2\mathbf{b}_{M_2} + \mathbf{q}_3}^{2,0}$	-0.7181 +0.7070i	-1.0107 +0.2665i	-0.4971 +0.8302i	-0.0185 +0.5578i	-1.1966 +0.3077i	-1.7225 +0.0792i	-1.1288 -2.3071i
$w_{bt, 2\mathbf{b}_{M_2} + \mathbf{q}_3}^{1,1}$	0.5300 -0.2277i	-1.4925 +0.9386i	1.4992 -0.3440i	0.6332 -0.3231i	-0.1047 -0.0061i	-1.0176 +0.3902i	-2.3679 -0.5796i

TABLE XI: Interlayer potential term parameters (meV) for the full model of  $t\text{MoTe}_2$  based on DFT with standard selection (continued)

Parameter	3.89°	3.48°	3.15°	2.88°	2.65°	2.45°	2.13°
$w_{bt,2\mathbf{b}_{M_2}+\mathbf{q}_3}^{0,2}$	-0.2028 -0.4878i	-1.1942 -0.0577i	0.0900 -1.1841i	-1.2701 +0.2885i	0.4657 -0.8427i	0.7309 -0.4912i	-0.2693 -1.1686i
$w_{bt,2\mathbf{b}_{M_2}+\mathbf{q}_3}^{3,0}$	-0.6157 -1.4374i	1.5987 +6.9120i	0.7759 -6.7452i	-0.0800 -0.3630i	7.1134 -1.2342i	12.7149 +2.8674i	-4.8544 +8.5618i
$w_{bt,2\mathbf{b}_{M_2}+\mathbf{q}_3}^{2,1}$	-5.1446 -2.5204i	15.3290 -3.0313i	-14.4770 -15.8421i	-1.6233 -3.9781i	2.4433 -21.1427i	16.4929 -26.0245i	13.9867 +16.7089i
$w_{bt,2\mathbf{b}_{M_2}+\mathbf{q}_3}^{1,2}$	-2.8649 +1.2732i	1.6557 +4.1054i	-8.7205 +8.1569i	3.8440 +4.7813i	-4.0429 -2.0422i	-1.5380 -11.4718i	25.9900 +1.8942i
$w_{bt,2\mathbf{b}_{M_2}+\mathbf{q}_3}^{0,3}$	-0.3721 +0.0255i	0.6655 -1.5827i	0.0381 +2.3436i	-0.3701 -1.4142i	-1.8648 +1.7431i	-3.6403 +1.1216i	-0.3701 -3.5282i
$w_{bt,2\mathbf{b}_{M_2}+\mathbf{q}_3}^{4,0}$	0.9231 +7.5384i	9.7396 -21.1936i	-19.1385 +21.9260i	0.0000 +0.0000i	-36.2117 +1.0123i	-51.4117 -21.6421i	12.2042 -5.3033i
$w_{bt,2\mathbf{b}_{M_2}+\mathbf{q}_3}^{3,1}$	23.6789 -1.1393i	-43.3988 -35.3379i	21.4334 +60.9362i	0.0000 +0.0000i	-67.7791 +65.0237i	-155.8077 +64.4559i	-7.0705 -26.8617i
$w_{bt,2\mathbf{b}_{M_2}+\mathbf{q}_3}^{2,2}$	9.9889 +3.4244i	2.4468 +3.2072i	78.1143 +22.7494i	0.0000 +0.0000i	55.4075 +106.5019i	22.5177 +188.4086i	-64.7723 -76.1190i
$w_{bt,2\mathbf{b}_{M_2}+\mathbf{q}_3}^{1,3}$	3.5615 +1.7714i	-0.4121 +1.7055i	11.2313 -19.0146i	0.0000 +0.0000i	25.0803 -0.9158i	40.2366 +18.5741i	-37.0608 +72.5536i
$w_{bt,2\mathbf{b}_{M_2}+\mathbf{q}_3}^{5,0}$	1.0207 -1.4320i	-15.0932 +6.9924i	31.8396 -0.3526i	0.0000 +0.0000i	47.6263 +36.1209i	57.7651 +76.4713i	0.0000 +0.0000i
$w_{bt,2\mathbf{b}_{M_2}+\mathbf{q}_3}^{4,1}$	-34.6276 -22.8014i	24.2119 +87.1181i	15.2699 -92.3237i	0.0000 +0.0000i	124.2473 -62.0935i	242.6091 -5.1401i	0.0000 +0.0000i
$w_{bt,2\mathbf{b}_{M_2}+\mathbf{q}_3}^{3,2}$	0.0000 +0.0000i	0.0000 +0.0000i	-48.6796 -91.8064i	0.0000 +0.0000i	112.1555 -253.4121i	306.4947 -406.2398i	0.0000 +0.0000i
$w_{bt,2\mathbf{b}_{M_2}+\mathbf{q}_3}^{2,3}$	0.0000 +0.0000i	0.0000 +0.0000i	-100.4084 +28.9199i	0.0000 +0.0000i	-202.6004 -56.2355i	-286.1866 -168.3626i	0.0000 +0.0000i
$w_{bt,4\mathbf{q}_1}^{0,0}$	0.0000 +0.0000i	0.0000 +0.0000i	0.0000 +0.0000i	-0.0558 -0.0173i	-0.0552 +0.0149i	-0.0667 +0.0200i	-0.0845 +0.0267i
$w_{bt,4\mathbf{q}_1}^{1,0}$	0.0000 +0.0000i	0.0000 +0.0000i	0.0000 +0.0000i	-0.0510 +0.0948i	-0.0409 -0.0421i	-0.0136 -0.0496i	0.0322 -0.0663i
$w_{bt,4\mathbf{q}_1}^{2,0}$	0.0000 +0.0000i	0.0000 +0.0000i	0.0000 +0.0000i	-0.0591 -0.0361i	0.5732 +0.0406i	0.9460 -0.0452i	1.6091 -0.2489i
$w_{bt,4\mathbf{q}_1}^{1,1}$	0.0000 +0.0000i	0.0000 +0.0000i	0.0000 +0.0000i	0.4660 +0.4168i	0.5240 -0.7794i	0.5113 -0.7275i	0.3810 -0.3999i
$w_{bt,4\mathbf{q}_1}^{3,0}$	0.0000 +0.0000i	0.0000 +0.0000i	0.0000 +0.0000i	0.0725 +0.1460i	0.3808 +1.1057i	-0.0829 +1.6608i	-1.5360 +2.2930i
$w_{bt,4\mathbf{q}_1}^{2,1}$	0.0000 +0.0000i	0.0000 +0.0000i	0.0000 +0.0000i	0.5636 -1.3837i	-1.2020 +0.2488i	-1.5307 +0.4104i	-0.7305 +1.0836i
$w_{bt,4\mathbf{q}_1}^{4,0}$	0.0000 +0.0000i	0.0000 +0.0000i	0.0000 +0.0000i	0.0000 +0.0000i	1.2094 -1.5205i	2.2241 -1.0335i	0.9666 +1.3120i
$w_{bt,4\mathbf{q}_1}^{3,1}$	0.0000 +0.0000i	0.0000 +0.0000i	0.0000 +0.0000i	0.0000 +0.0000i	-7.1418 +6.6469i	-12.3241 +6.7989i	-22.2557 -2.2319i
$w_{bt,4\mathbf{q}_1}^{2,2}$	0.0000 +0.0000i	0.0000 +0.0000i	0.0000 +0.0000i	0.0000 +0.0000i	-7.5172 +3.7609i	-10.0392 +1.8935i	-14.7744 -5.1883i
$w_{bt,4\mathbf{q}_1}^{5,0}$	0.0000 +0.0000i	0.0000 +0.0000i	0.0000 +0.0000i	0.0000 +0.0000i	0.6294 -2.3751i	1.6054 -3.5073i	0.0000 +0.0000i

TABLE XI: Interlayer potential term parameters (meV) for the full model of  $t\text{MoTe}_2$  based on DFT with standard selection (continued)

Parameter	3.89°	3.48°	3.15°	2.88°	2.65°	2.45°	2.13°
$w_{bt,4\mathbf{q}_1}^{4,1}$	0.0000 +0.0000i	0.0000 +0.0000i	0.0000 +0.0000i	0.0000 +0.0000i	11.4118 -3.6052i	14.0232 -1.2161i	0.0000 +0.0000i
$w_{bt,\mathbf{q}_1+2\mathbf{b}_{M_2}}^{0,0}$	0.0000 +0.0000i	0.0000 +0.0000i	0.0000 +0.0000i	0.0000 +0.0000i	0.0000 +0.0000i	-0.2181 +0.0550i	-0.3139 +0.0793i
$w_{bt,\mathbf{q}_1+2\mathbf{b}_{M_2}}^{1,0}$	0.0000 +0.0000i	0.0000 +0.0000i	0.0000 +0.0000i	0.0000 +0.0000i	0.0000 +0.0000i	0.3234 +0.0918i	0.3380 +0.0605i
$w_{bt,\mathbf{q}_1+2\mathbf{b}_{M_2}}^{0,1}$	0.0000 +0.0000i	0.0000 +0.0000i	0.0000 +0.0000i	0.0000 +0.0000i	0.0000 +0.0000i	-0.2058 -0.2487i	-0.2283 -0.4369i
$w_{bt,\mathbf{q}_1+2\mathbf{b}_{M_2}}^{2,0}$	0.0000 +0.0000i	0.0000 +0.0000i	0.0000 +0.0000i	0.0000 +0.0000i	0.0000 +0.0000i	3.0498 -0.3982i	3.5439 -0.7542i
$w_{bt,\mathbf{q}_1+2\mathbf{b}_{M_2}}^{1,1}$	0.0000 +0.0000i	0.0000 +0.0000i	0.0000 +0.0000i	0.0000 +0.0000i	0.0000 +0.0000i	0.6960 -1.5255i	1.2025 -1.5586i
$w_{bt,\mathbf{q}_1+2\mathbf{b}_{M_2}}^{0,2}$	0.0000 +0.0000i	0.0000 +0.0000i	0.0000 +0.0000i	0.0000 +0.0000i	0.0000 +0.0000i	0.2256 +0.0430i	0.6577 +0.2308i
$w_{bt,\mathbf{q}_1+2\mathbf{b}_{M_2}}^{3,0}$	0.0000 +0.0000i	0.0000 +0.0000i	0.0000 +0.0000i	0.0000 +0.0000i	0.0000 +0.0000i	3.6778 -8.4846i	-0.5879 -3.1630i
$w_{bt,\mathbf{q}_1+2\mathbf{b}_{M_2}}^{2,1}$	0.0000 +0.0000i	0.0000 +0.0000i	0.0000 +0.0000i	0.0000 +0.0000i	0.0000 +0.0000i	-19.3924 +4.1226i	-3.0352 +6.1292i
$w_{bt,\mathbf{q}_1+2\mathbf{b}_{M_2}}^{1,2}$	0.0000 +0.0000i	0.0000 +0.0000i	0.0000 +0.0000i	0.0000 +0.0000i	0.0000 +0.0000i	-0.0566 +9.3243i	-4.0532 +4.1376i
$w_{bt,\mathbf{q}_1+2\mathbf{b}_{M_2}}^{0,3}$	0.0000 +0.0000i	0.0000 +0.0000i	0.0000 +0.0000i	0.0000 +0.0000i	0.0000 +0.0000i	0.0060 +1.2469i	0.9032 +0.5955i
$w_{bt,\mathbf{q}_1+2\mathbf{b}_{M_2}}^{4,0}$	0.0000 +0.0000i	0.0000 +0.0000i	0.0000 +0.0000i	0.0000 +0.0000i	0.0000 +0.0000i	-17.2652 +7.7654i	-3.6091 +2.6465i
$w_{bt,\mathbf{q}_1+2\mathbf{b}_{M_2}}^{3,1}$	0.0000 +0.0000i	0.0000 +0.0000i	0.0000 +0.0000i	0.0000 +0.0000i	0.0000 +0.0000i	18.6975 +104.1233i	-14.5258 +5.4850i
$w_{bt,\mathbf{q}_1+2\mathbf{b}_{M_2}}^{2,2}$	0.0000 +0.0000i	0.0000 +0.0000i	0.0000 +0.0000i	0.0000 +0.0000i	0.0000 +0.0000i	54.8668 -48.3237i	-13.0313 +12.3474i
$w_{bt,\mathbf{q}_1+2\mathbf{b}_{M_2}}^{1,3}$	0.0000 +0.0000i	0.0000 +0.0000i	0.0000 +0.0000i	0.0000 +0.0000i	0.0000 +0.0000i	2.1623 -8.8695i	2.5690 -22.1989i
$w_{bt,\mathbf{q}_1+2\mathbf{b}_{M_2}}^{5,0}$	0.0000 +0.0000i	0.0000 +0.0000i	0.0000 +0.0000i	0.0000 +0.0000i	0.0000 +0.0000i	15.5538 -3.5782i	0.0000 +0.0000i
$w_{bt,\mathbf{q}_1+2\mathbf{b}_{M_2}}^{4,1}$	0.0000 +0.0000i	0.0000 +0.0000i	0.0000 +0.0000i	0.0000 +0.0000i	0.0000 +0.0000i	57.2298 -102.6990i	0.0000 +0.0000i
$w_{bt,\mathbf{q}_1+2\mathbf{b}_{M_2}}^{3,2}$	0.0000 +0.0000i	0.0000 +0.0000i	0.0000 +0.0000i	0.0000 +0.0000i	0.0000 +0.0000i	-228.4807 -132.5953i	0.0000 +0.0000i

TABLE XII: Kinetic term parameters ( $m_e$ ) for the reduced model of  $t\text{MoTe}_2$  based on DFT with standard basis selection

Parameter	3.89°	3.48°	3.15°	2.88°	2.65°	2.45°	2.13°
$m^{(1,1)}$	-0.6440	-0.6508	-0.6473	-0.6337	-0.6262	-0.6296	-0.6133



TABLE XIV: Interlayer potential term parameters (meV) for the reduced model of  $t\text{MoTe}_2$  based on DFT with standard basis selection (continued)

Parameter	3.89°	3.48°	3.15°	2.88°	2.65°	2.45°	2.13°
$w_{bt,\mathbf{q}_1}^{1,1}$	-10.7707 -4.8946i	0.0000 +0.0000i	0.0000 +0.0000i	0.0000 +0.0000i	0.0000 +0.0000i	0.0000 +0.0000i	0.0000 +0.0000i
$w_{bt,\mathbf{q}_1}^{3,0}$	-24.7826 -4.0028i	0.0000 +0.0000i	0.0000 +0.0000i	0.0000 +0.0000i	0.0000 +0.0000i	0.0000 +0.0000i	0.0000 +0.0000i
$w_{bt,\mathbf{q}_1}^{2,1}$	-31.3375 +70.9930i	0.0000 +0.0000i	0.0000 +0.0000i	0.0000 +0.0000i	0.0000 +0.0000i	0.0000 +0.0000i	0.0000 +0.0000i
$w_{bt,-2\mathbf{q}_1}^{0,0}$	0.3923 +0.2455i	0.2807 -0.2837i	0.3322 +0.2350i	0.2670 -0.2831i	0.3257 +0.2312i	0.3197 +0.2220i	0.3147 +0.2018i
$w_{bt,-2\mathbf{q}_1}^{1,0}$	0.0681 +0.6804i	0.2317 -0.5987i	0.2872 +0.5743i	0.3902 -0.5340i	0.4747 +0.4984i	0.5566 +0.4749i	0.6813 +0.5111i
$w_{bt,-2\mathbf{q}_1}^{2,0}$	0.5935 +0.4513i	0.0000 +0.0000i	0.0000 +0.0000i	0.0000 +0.0000i	0.0000 +0.0000i	0.0000 +0.0000i	0.0000 +0.0000i
$w_{bt,-2\mathbf{q}_1}^{1,1}$	-1.1855 -0.9569i	0.0000 +0.0000i	0.0000 +0.0000i	0.0000 +0.0000i	0.0000 +0.0000i	0.0000 +0.0000i	0.0000 +0.0000i
$w_{bt,-2\mathbf{q}_1}^{3,0}$	-0.4245 +6.2855i	0.0000 +0.0000i	0.0000 +0.0000i	0.0000 +0.0000i	0.0000 +0.0000i	0.0000 +0.0000i	0.0000 +0.0000i
$w_{bt,\mathbf{q}_1+\mathbf{b}_{M_2}}^{0,0}$	0.0000 +0.0000i	-0.5551 -0.1236i	-0.6019 +0.1165i	-0.6972 -0.1090i	-0.7644 +0.0904i	-0.8198 +0.0674i	-0.8879 +0.0187i
$w_{bt,\mathbf{q}_1+\mathbf{b}_{M_2}}^{1,0}$	0.0000 +0.0000i	-0.0213 +0.5539i	0.4562 -0.5058i	0.2803 +0.5249i	0.4742 -0.3089i	0.4547 -0.1317i	0.3983 +0.3020i
$w_{bt,\mathbf{q}_1+\mathbf{b}_{M_2}}^{0,1}$	0.0000 +0.0000i	0.4369 +0.5896i	0.1079 -0.5303i	0.4819 +0.4407i	0.4521 -0.4413i	0.6272 -0.3059i	0.8907 +0.0047i
$w_{bt,2\mathbf{b}_{M_2}+\mathbf{q}_3}^{0,0}$	0.0000 +0.0000i	0.0000 +0.0000i	0.1401 +0.0734i	0.0000 +0.0000i	0.1778 +0.1466i	0.1894 +0.1730i	0.2062 +0.2028i
$w_{bt,2\mathbf{b}_{M_2}+\mathbf{q}_3}^{1,0}$	0.0000 +0.0000i	0.0000 +0.0000i	-0.0212 -0.0986i	0.0000 +0.0000i	-0.0156 -0.2373i	-0.0275 -0.3075i	-0.0866 -0.4050i
$w_{bt,2\mathbf{b}_{M_2}+\mathbf{q}_3}^{0,1}$	0.0000 +0.0000i	0.0000 +0.0000i	0.1746 -0.2210i	0.0000 +0.0000i	0.1894 -0.3469i	0.1934 -0.4068i	0.2620 -0.5225i

TABLE XV: Kinetic term parameters ( $m_e$ ) for the full model of  $t\text{WSe}_2$  based on DFT with quick basis selection

Parameter	3.89°	3.48°	3.15°	2.88°	2.65°	2.45°	2.13°
$m^{(1,1)}$	-0.3742	-0.3788	-0.3715	-0.3701	-0.3750	-0.3713	-0.3668
$m^{(3,0)}$	1.4591	1.2957	1.2412	1.2165	1.1930	1.1717	1.1468
$m^{(2,2)}$	0.0379	0.0395	0.0356	0.0350	0.0368	0.0346	0.0317
$m^{(4,1)}$	-0.2042	-0.1319	-0.1140	-0.1091	-0.0995	-0.0912	-0.0805
$m^{(3,3)}$	-0.0050	-0.0052	-0.0040	-0.0042	-0.0044	-0.0037	-0.0027
$m^{(6,0)}$	0.3467	0.2152	0.1545	0.1565	0.1730	0.1439	0.1044
$m^{(5,2)}$	0.2080	0.0358	0.0263	0.0285	0.0228	0.0186	0.0134
$m^{(4,4)}$	0.0012	0.0011	0.0007	0.0011	0.0011	0.0008	0.0004
$m^{(7,1)}$	-0.0890	-0.0674	-0.0354	-0.0150	-0.0141	-0.0100	-0.0054
$m^{(6,3)}$	0.0329	-0.0362	-0.0225	0.0000	0.0000	0.0000	0.0000
$m^{(9,0)}$	0.8449	2.6952	1.3035	0.0000	0.0000	0.0000	0.0000

TABLE XV: Kinetic term parameters ( $m_e$ ) for the full model of  $tWSe_2$  based on DFT with quick basis selection (continued)

Parameter	3.89°	3.48°	3.15°	2.88°	2.65°	2.45°	2.13°
$m^{(5,5)}$	-0.0006	-0.0005	-0.0003	0.0000	0.0000	0.0000	0.0000
$m^{(8,2)}$	-0.0276	-0.0059	-0.0030	0.0000	0.0000	0.0000	0.0000

TABLE XVI: Intralayer potential term parameters (meV) for the full model of  $tWSe_2$  based on DFT with quick basis selection

Parameter	3.89°	3.48°	3.15°	2.88°	2.65°	2.45°	2.13°
$V_{b,b_{M_1}}^{0,0}$	-0.1222 -1.2489i	-0.1193 -1.3645i	-0.1206 -1.4292i	-0.1063 -1.4495i	-0.1038 -1.4243i	-0.0977 -1.3206i	-0.0843 -1.0448i
$V_{b,b_{M_1}}^{1,0}$	-1.0320 -6.2431i	-1.1277 -7.0645i	-1.1965 -7.8493i	-1.3193 -8.1281i	-1.3149 -8.7639i	-1.2837 -9.1403i	-1.1367 -8.9846i
$V_{b,b_{M_1}}^{0,1}$	0.0611 -4.3291i	0.0344 -3.9170i	0.0434 -3.4040i	-0.2905 -2.6829i	-0.3297 -2.0586i	-0.3741 -1.3826i	-0.2097 -0.3157i
$V_{b,b_{M_1}}^{-2,0}$	-1.5161 -26.7681i	-1.6718 -31.3323i	-1.9447 -35.7410i	1.4580 -38.4323i	1.3432 -42.0794i	1.2294 -44.4275i	-0.2800 -43.8232i
$V_{b,b_{M_1}}^{1,1}$	3.1686 +1.5509i	3.1322 +3.1542i	3.1147 +4.8481i	2.3772 +5.5773i	2.1016 +7.2425i	1.7004 +8.6743i	-1.1961 +15.9635i
$V_{b,b_{M_1}}^{0,2}$	-0.7984 +25.0116i	-1.1856 +30.4357i	-1.5403 +35.7085i	1.0806 +39.1549i	0.8428 +43.3535i	0.6611 +46.2139i	-2.0173 +48.1438i
$V_{b,b_{M_1}}^{3,0}$	1.6444 -6.2855i	1.8366 -8.2211i	2.1702 -10.0162i	-1.1167 -4.1631i	-0.7761 -4.7683i	-0.2075 -5.0291i	3.6886 -1.3012i
$V_{b,b_{M_1}}^{-2,1}$	1.3545 +61.7439i	3.9200 +81.0291i	6.9777 +100.9839i	9.7028 +89.1906i	10.6914 +105.2454i	11.2836 +118.0520i	13.0175 +83.3226i
$V_{b,b_{M_1}}^{1,2}$	-13.7979 +52.8544i	-15.3382 +54.3530i	-17.0840 +53.8930i	-5.0249 +55.4498i	-3.3105 +53.0164i	-0.8390 +48.4558i	-6.2682 +49.7081i
$V_{b,b_{M_1}}^{0,3}$	3.0315 +30.9539i	3.7589 +34.8747i	4.4317 +38.3096i	-1.5361 +29.7210i	-1.7514 +31.4537i	-2.0868 +32.2321i	-2.6603 +26.8152i
$V_{b,b_{M_1}}^{-4,0}$	9.6038 -1.2401i	10.8284 -3.1716i	12.1351 -5.8731i	8.4263 +6.2905i	10.3982 +6.0359i	12.6161 +4.9443i	-14.3078 -20.6510i
$V_{b,b_{M_1}}^{3,1}$	22.2211 +159.8106i	28.1640 +208.1806i	36.1882 +261.6863i	-48.8514 +300.6176i	-55.6429 +357.6370i	-60.3965 +407.4653i	-15.6577 +318.2517i
$V_{b,b_{M_1}}^{-2,2}$	-33.9648 +5.9292i	-40.6363 +1.1169i	-47.2528 -8.0542i	-70.7725 +1.2958i	-77.4130 -11.7781i	-80.0137 -28.6384i	58.7704 -233.4168i
$V_{b,b_{M_1}}^{-1,3}$	14.6634 -141.3782i	22.3308 -195.3184i	30.8163 -257.5311i	-39.3509 -286.7114i	-42.5941 -346.3424i	-45.5860 -398.9462i	69.4788 -402.6119i
$V_{b,b_{M_1}}^{0,4}$	11.1828 -13.2054i	14.7028 -17.6541i	18.1831 -21.7488i	16.4937 -34.9295i	19.5747 -39.9027i	22.1241 -43.4516i	9.3867 -21.1848i
$V_{b,b_{M_1}}^{5,0}$	-13.2730 -25.3217i	-16.2573 -33.3868i	-19.4722 -42.0625i	-22.9944 -18.0965i	-27.5290 -20.6975i	-30.7785 -21.7722i	0.0000 +0.0000i
$V_{b,b_{M_1}}^{-4,1}$	-39.6942 +2.5365i	-51.8345 +20.0689i	-70.4674 +44.1246i	40.3850 -113.6433i	39.7645 -136.3370i	29.4516 -157.5369i	0.0000 +0.0000i
$V_{b,b_{M_1}}^{-3,2}$	48.5976 -378.5911i	53.9235 -566.4767i	50.7227 -794.5324i	178.3586 -693.6572i	224.0478 -885.5547i	268.4636 -1064.4963i	0.0000 +0.0000i
$V_{b,b_{M_1}}^{-2,3}$	122.9346 -0.4279i	165.8073 +39.2681i	218.6828 +103.9888i	251.0529 +8.1065i	283.9758 +46.4243i	301.5584 +91.0626i	0.0000 +0.0000i
$V_{b,b_{M_1}}^{-1,4}$	-56.5226 -102.7945i	-86.0957 -127.0557i	-123.1173 -150.9536i	13.2314 +13.5929i	16.0884 +31.9309i	24.4531 +53.4217i	0.0000 +0.0000i

TABLE XVI: Intralayer potential term parameters (meV) for the full model of  $tWSe_2$  based on DFT with quick basis selection (continued)

Parameter	3.89°	3.48°	3.15°	2.88°	2.65°	2.45°	2.13°
$V_{b,b_{M_1}}^{0,5}$	-11.6817 +20.7905i	-17.8464 +32.1011i	-25.0790 +45.5137i	-35.5496 +35.7652i	-43.8263 +44.6697i	-51.6015 +51.8446i	0.0000 +0.0000i
$V_{b,b_{M_1}+b_{M_2}}^{-0,0}$	-0.0876 -0.0718i	-0.0838 -0.0328i	-0.0808 +0.0023i	-0.0614 +0.0468i	-0.0515 +0.0772i	-0.0402 +0.0964i	-0.0154 +0.1183i
$V_{b,b_{M_1}+b_{M_2}}^{1,0}$	0.5382 -0.1160i	0.4470 -0.1428i	0.3306 -0.1880i	0.1676 -0.1683i	-0.0128 -0.2461i	-0.1510 -0.3071i	-0.3645 -0.3991i
$V_{b,b_{M_1}+b_{M_2}}^{0,1}$	0.4746 +0.5365i	0.4446 +0.4911i	0.3918 +0.4157i	0.3141 +0.2911i	0.1785 +0.1565i	0.0565 +0.0556i	-0.2121 -0.0934i
$V_{b,b_{M_1}+b_{M_2}}^{-2,0}$	-1.7298 +1.3998i	-1.6282 +1.4558i	-1.3565 +1.4066i	-0.3981 -0.1472i	0.3572 -0.5680i	0.9746 -0.9339i	1.8123 -1.0904i
$V_{b,b_{M_1}+b_{M_2}}^{-1,1}$	2.6408 +2.9204i	2.9827 +2.9464i	3.4110 +2.8466i	1.0435 +0.5958i	0.9451 +0.0404i	0.7929 -0.3627i	0.1842 -0.6406i
$V_{b,b_{M_1}+b_{M_2}}^{0,2}$	-0.1267 -0.7501i	0.0505 -0.6500i	0.2738 -0.4928i	-0.5717 +0.1823i	-0.3387 +0.6195i	-0.1165 +1.0322i	0.9084 +1.2067i
$V_{b,b_{M_1}+b_{M_2}}^{3,0}$	-1.4309 +1.1185i	-2.2741 +1.4802i	-3.0034 +1.9562i	0.0473 +0.0339i	0.5393 +0.4125i	0.9936 +0.8030i	1.6704 +1.4977i
$V_{b,b_{M_1}+b_{M_2}}^{-2,1}$	-2.6413 +2.3476i	-3.4937 +3.1608i	-4.1746 +3.9839i	-2.7302 +2.6048i	-1.8799 +3.3661i	-1.3090 +3.9019i	-0.3050 +2.3868i
$V_{b,b_{M_1}+b_{M_2}}^{-1,2}$	-5.8933 -3.5711i	-7.1974 -4.3683i	-8.5156 -4.6785i	-3.4673 -2.9329i	-3.0240 -1.5434i	-2.3320 -0.3979i	1.8942 +2.4878i
$V_{b,b_{M_1}+b_{M_2}}^{0,3}$	-1.7931 +0.3174i	-2.7083 +0.1511i	-3.5225 +0.1061i	0.0526 -1.5375i	0.6188 -1.3796i	1.1592 -1.3262i	1.9073 -1.0862i
$V_{b,b_{M_1}+b_{M_2}}^{-4,0}$	9.5918 -9.8196i	16.3726 -8.7969i	24.4920 -7.6358i	-4.2970 -1.0204i	-5.2807 -0.5032i	-6.1338 +0.2815i	2.2037 -8.7881i
$V_{b,b_{M_1}+b_{M_2}}^{-3,1}$	7.8030 -46.8104i	17.8025 -62.4581i	27.4833 -80.2536i	-2.3065 +10.0972i	-10.6117 +19.6441i	-17.1167 +29.1135i	-15.3428 +5.8092i
$V_{b,b_{M_1}+b_{M_2}}^{-2,2}$	-48.8225 -29.1128i	-62.5905 -43.6792i	-81.1867 -59.3644i	-2.1951 +0.5977i	6.1619 +6.6573i	15.4537 +12.2496i	25.8066 +0.4767i
$V_{b,b_{M_1}+b_{M_2}}^{-1,3}$	-0.0014 +7.3668i	-1.8979 +9.9187i	-4.7872 +12.9042i	13.7364 -6.3802i	16.8528 -14.6205i	20.3678 -23.1657i	-17.4287 +4.8682i
$V_{b,b_{M_1}+b_{M_2}}^{-0,4}$	-0.2200 -2.2031i	1.5638 -3.4100i	3.7554 -5.0328i	1.0131 -1.4443i	1.5357 -2.9361i	1.8569 -4.6321i	1.7531 +0.4270i
$V_{b,b_{M_1}+b_{M_2}}^{-5,0}$	-13.7159 +5.7050i	-20.2722 +1.7961i	-28.7193 -4.2487i	3.7098 +3.8813i	7.1366 +2.4802i	11.1014 +0.7214i	0.0000 +0.0000i
$V_{b,b_{M_1}+b_{M_2}}^{-4,1}$	-20.1812 +54.2999i	-48.1949 +69.9813i	-86.2781 +88.3284i	25.5127 -20.9336i	35.4916 -39.2070i	43.1894 -63.1743i	0.0000 +0.0000i
$V_{b,b_{M_1}+b_{M_2}}^{-3,2}$	63.7463 +94.5793i	80.4934 +149.8409i	106.9606 +223.6108i	19.8908 -33.8914i	18.1390 -68.8377i	15.3171 -102.8754i	0.0000 +0.0000i
$V_{b,b_{M_1}+b_{M_2}}^{-2,3}$	77.2385 -10.2621i	120.7600 -3.4739i	182.4008 +2.2712i	-10.3223 +6.0901i	-34.0416 +16.0064i	-64.4742 +27.1098i	0.0000 +0.0000i
$V_{b,b_{M_1}+b_{M_2}}^{-1,4}$	0.0000 +0.0000i	0.0000 +0.0000i	0.0000 +0.0000i	-19.4208 +31.2335i	-27.8144 +50.1461i	-37.2442 +75.0236i	0.0000 +0.0000i
$V_{b,2b_{M_1}}^{0,0}$	0.0000 +0.0000i	0.0000 +0.0000i	0.0000 +0.0000i	0.0815 -0.1248i	0.0734 -0.1798i	0.0642 -0.2381i	0.0441 -0.3585i
$V_{b,2b_{M_1}}^{1,0}$	0.0000 +0.0000i	0.0000 +0.0000i	0.0000 +0.0000i	-0.0915 -0.6601i	-0.1605 -0.9344i	-0.2127 -1.2084i	-0.2214 -1.7226i

TABLE XVI: Intralayer potential term parameters (meV) for the full model of  $tWSe_2$  based on DFT with quick basis selection (continued)

Parameter	3.89°	3.48°	3.15°	2.88°	2.65°	2.45°	2.13°
$V_{b,2b_{M_1}}^{0,1}$	0.0000 +0.0000i	0.0000 +0.0000i	0.0000 +0.0000i	-0.1748 -1.0204i	-0.1863 -1.3192i	-0.1926 -1.5420i	-0.1848 -1.8999i
$V_{b,2b_{M_1}}^{2,0}$	0.0000 +0.0000i	0.0000 +0.0000i	0.0000 +0.0000i	0.2805 -3.4178i	0.2090 -4.9037i	0.1338 -6.3801i	0.0266 -9.1475i
$V_{b,2b_{M_1}}^{1,1}$	0.0000 +0.0000i	0.0000 +0.0000i	0.0000 +0.0000i	-1.3667 -2.0164i	-1.4291 -2.3682i	-1.4535 -2.4766i	-1.3743 -1.5195i
$V_{b,2b_{M_1}}^{0,2}$	0.0000 +0.0000i	0.0000 +0.0000i	0.0000 +0.0000i	0.1852 +1.2317i	0.3196 +2.2449i	0.4083 +3.4376i	-0.0403 +6.2859i
$V_{b,2b_{M_1}}^{3,0}$	0.0000 +0.0000i	0.0000 +0.0000i	0.0000 +0.0000i	3.3427 -2.7353i	4.0592 -3.5317i	4.5989 -4.1718i	0.6995 -1.5547i
$V_{b,2b_{M_1}}^{2,1}$	0.0000 +0.0000i	0.0000 +0.0000i	0.0000 +0.0000i	7.9498 +8.8357i	10.4266 +13.0279i	12.1451 +17.8466i	1.9683 +21.8038i
$V_{b,2b_{M_1}}^{1,2}$	0.0000 +0.0000i	0.0000 +0.0000i	0.0000 +0.0000i	0.3149 +20.6701i	-0.6035 +28.4038i	-1.7818 +35.3991i	-6.6658 +48.4655i
$V_{b,2b_{M_1}}^{0,3}$	0.0000 +0.0000i	0.0000 +0.0000i	0.0000 +0.0000i	-1.3776 +7.4252i	-1.9284 +10.1433i	-2.4543 +12.6153i	-3.8546 +15.2995i
$V_{b,2b_{M_1}}^{4,0}$	0.0000 +0.0000i	0.0000 +0.0000i	0.0000 +0.0000i	-7.7360 +4.9698i	-10.4407 +5.5147i	-12.8185 +5.3206i	-2.0247 -7.8112i
$V_{b,2b_{M_1}}^{3,1}$	0.0000 +0.0000i	0.0000 +0.0000i	0.0000 +0.0000i	-37.7932 +27.2706i	-49.1626 +40.4254i	-58.2780 +53.4029i	-7.4931 +61.9795i
$V_{b,2b_{M_1}}^{2,2}$	0.0000 +0.0000i	0.0000 +0.0000i	0.0000 +0.0000i	-23.8854 -22.1800i	-31.6841 -30.4975i	-36.1244 -40.8931i	25.9009 -60.9635i
$V_{b,2b_{M_1}}^{1,3}$	0.0000 +0.0000i	0.0000 +0.0000i	0.0000 +0.0000i	-1.0944 -38.6400i	-1.8116 -57.4335i	-1.5509 -78.1766i	30.4769 -104.8951i
$V_{b,2b_{M_1}}^{0,4}$	0.0000 +0.0000i	0.0000 +0.0000i	0.0000 +0.0000i	2.7237 -2.3523i	3.9585 -3.5096i	5.2101 -4.6070i	4.9639 -5.8027i
$V_{b,2b_{M_1}}^{5,0}$	0.0000 +0.0000i	0.0000 +0.0000i	0.0000 +0.0000i	4.2956 -10.6640i	5.8590 -14.8953i	7.4514 -19.0627i	0.0000 +0.0000i
$V_{b,2b_{M_1}}^{4,1}$	0.0000 +0.0000i	0.0000 +0.0000i	0.0000 +0.0000i	33.0788 -13.8578i	47.1757 -15.0249i	59.5787 -12.3591i	0.0000 +0.0000i
$V_{b,2b_{M_1}}^{3,2}$	0.0000 +0.0000i	0.0000 +0.0000i	0.0000 +0.0000i	48.8988 -27.6547i	68.0480 -46.7082i	85.1130 -67.8205i	0.0000 +0.0000i
$V_{b,2b_{M_1}}^{2,3}$	0.0000 +0.0000i	0.0000 +0.0000i	0.0000 +0.0000i	40.5562 +40.4875i	67.3287 +54.4634i	94.3269 +71.5792i	0.0000 +0.0000i
$V_{b,2b_{M_1}+b_{M_2}}^{0,0}$	0.0000 +0.0000i	0.0000 +0.0000i	0.0000 +0.0000i	0.0278 -0.0102i	0.0355 -0.0145i	0.0409 -0.0217i	0.0000 +0.0000i
$V_{b,2b_{M_1}+b_{M_2}}^{-1,0}$	0.0000 +0.0000i	0.0000 +0.0000i	0.0000 +0.0000i	-0.0137 -0.0390i	-0.0301 -0.0541i	-0.0544 -0.0776i	0.0000 +0.0000i
$V_{b,2b_{M_1}+b_{M_2}}^{0,1}$	0.0000 +0.0000i	0.0000 +0.0000i	0.0000 +0.0000i	-0.0228 -0.0902i	-0.0518 -0.1487i	-0.0844 -0.2231i	0.0000 +0.0000i
$V_{b,2b_{M_1}+b_{M_2}}^{2,0}$	0.0000 +0.0000i	0.0000 +0.0000i	0.0000 +0.0000i	0.7041 -0.3196i	0.8992 -0.7127i	1.0926 -1.2299i	0.0000 +0.0000i
$V_{b,2b_{M_1}+b_{M_2}}^{-1,1}$	0.0000 +0.0000i	0.0000 +0.0000i	0.0000 +0.0000i	0.1759 +0.2638i	0.3290 +0.1595i	0.5559 +0.0134i	0.0000 +0.0000i
$V_{b,2b_{M_1}+b_{M_2}}^{0,2}$	0.0000 +0.0000i	0.0000 +0.0000i	0.0000 +0.0000i	-0.1622 +0.1201i	-0.1540 +0.1859i	-0.1203 +0.3040i	0.0000 +0.0000i



TABLE XVI: Intralayer potential term parameters (meV) for the full model of  $tWSe_2$  based on DFT with quick basis selection (continued)

Parameter	3.89°	3.48°	3.15°	2.88°	2.65°	2.45°	2.13°
$V_{b,2b_{M_1}+b_{M_2}}^{3,0}$	0.0000 +0.0000i	0.0000 +0.0000i	0.0000 +0.0000i	-1.4713 +1.3214i	-1.4458 +2.7419i	-1.3236 +4.7042i	0.0000 +0.0000i
$V_{b,2b_{M_1}+b_{M_2}}^{2,1}$	0.0000 +0.0000i	0.0000 +0.0000i	0.0000 +0.0000i	-3.9632 -0.6024i	-5.6511 +0.3429i	-7.6407 +2.0443i	0.0000 +0.0000i
$V_{b,2b_{M_1}+b_{M_2}}^{1,2}$	0.0000 +0.0000i	0.0000 +0.0000i	0.0000 +0.0000i	-0.2238 -0.8740i	-0.7579 -0.9941i	-1.5464 -1.0385i	0.0000 +0.0000i
$V_{b,2b_{M_1}+b_{M_2}}^{0,3}$	0.0000 +0.0000i	0.0000 +0.0000i	0.0000 +0.0000i	0.1933 +0.2066i	0.2695 +0.4389i	0.3490 +0.7300i	0.0000 +0.0000i
$V_{b,2b_{M_1}+b_{M_2}}^{4,0}$	0.0000 +0.0000i	0.0000 +0.0000i	0.0000 +0.0000i	1.8462 -4.0441i	0.4197 -7.8443i	-2.0268 -13.4719i	0.0000 +0.0000i
$V_{b,2b_{M_1}+b_{M_2}}^{3,1}$	0.0000 +0.0000i	0.0000 +0.0000i	0.0000 +0.0000i	6.5779 -2.5447i	7.5969 -7.2011i	8.3361 -14.9535i	0.0000 +0.0000i
$V_{b,2b_{M_1}+b_{M_2}}^{2,2}$	0.0000 +0.0000i	0.0000 +0.0000i	0.0000 +0.0000i	3.3545 +3.2934i	6.2386 +5.0518i	10.2577 +6.9634i	0.0000 +0.0000i
$V_{b,2b_{M_1}+b_{M_2}}^{5,0}$	0.0000 +0.0000i	0.0000 +0.0000i	0.0000 +0.0000i	-0.2187 +2.2527i	1.5770 +4.2740i	4.5823 +7.5150i	0.0000 +0.0000i
$V_{b,2b_{M_1}+b_{M_2}}^{4,1}$	0.0000 +0.0000i	0.0000 +0.0000i	0.0000 +0.0000i	-7.2975 +7.9801i	-5.9806 +17.5978i	-1.5435 +34.0408i	0.0000 +0.0000i

TABLE XVII: Interlayer potential term parameters (meV) for the full model of  $tWSe_2$  based on DFT with quick basis selection

Parameter	3.89°	3.48°	3.15°	2.88°	2.65°	2.45°	2.13°
$w_{bt,\mathbf{q}_1}^{0,0}$	-1.5555 +0.6453i	-1.5626 +0.5906i	-1.5516 +0.5446i	-1.4628 +0.5055i	-1.4392 +0.4691i	-1.4107 +0.4365i	-1.3504 +0.3686i
$w_{bt,\mathbf{q}_1}^{1,0}$	10.3189 -3.0129i	11.0250 -2.9568i	11.6688 -2.9061i	12.3393 -3.2604i	12.8802 -3.2071i	13.3327 -3.1307i	13.6510 -2.6990i
$w_{bt,\mathbf{q}_1}^{2,0}$	36.8862 -4.0139i	37.9556 -2.8452i	39.1189 -1.9364i	41.1790 -0.8469i	42.2805 -0.2300i	43.1377 +0.3050i	43.5504 +0.9619i
$w_{bt,\mathbf{q}_1}^{1,1}$	-6.5362 +0.5277i	-5.9060 +1.0738i	-5.3277 +1.4748i	-9.8047 -0.4981i	-9.1920 -0.5169i	-8.6823 -0.5723i	-6.6245 +2.2016i
$w_{bt,\mathbf{q}_1}^{3,0}$	-41.6618 +6.2763i	-44.5386 +5.6079i	-47.0099 +5.0751i	-43.3325 +4.6681i	-44.8408 +3.7666i	-45.8788 +3.0200i	-30.1807 +5.7980i
$w_{bt,\mathbf{q}_1}^{2,1}$	-83.0724 +27.9134i	-93.4599 +25.1717i	-102.3584 +21.2885i	-130.7495 +51.0639i	-143.0680 +51.6052i	-154.1858 +51.4992i	-116.5374 +24.1390i
$w_{bt,\mathbf{q}_1}^{4,0}$	38.3277 -42.8287i	45.7377 -45.9913i	51.8141 -49.3781i	69.0756 -46.0896i	77.4548 -47.5598i	84.9780 -48.3337i	100.7315 -22.6182i
$w_{bt,\mathbf{q}_1}^{3,1}$	-120.3224 +8.9309i	-122.6365 +1.7316i	-125.7644 -3.5344i	-162.9968 -29.7425i	-176.6892 -37.0201i	-190.4307 -44.3366i	-184.4705 -33.2036i
$w_{bt,\mathbf{q}_1}^{2,2}$	-3.3039 -10.9699i	-14.6521 -20.1288i	-28.6592 -31.0733i	37.8117 +5.2215i	34.1804 +5.9893i	30.2270 +7.0829i	-13.9778 -84.2439i
$w_{bt,\mathbf{q}_1}^{5,0}$	-77.8108 +22.8263i	-93.2206 +31.5688i	-111.7073 +43.9193i	-100.1696 +32.6110i	-112.0878 +34.5837i	-122.6441 +36.3836i	0.0000 +0.0000i
$w_{bt,\mathbf{q}_1}^{4,1}$	225.8543 +29.8574i	268.4545 +23.5454i	320.6616 +9.4897i	239.0620 +65.4695i	275.3541 +74.7632i	311.6071 +82.3481i	0.0000 +0.0000i

TABLE XVII: Interlayer potential term parameters (meV) for the full model of  $tWSe_2$  based on DFT with quick basis selection (continued)

Parameter	3.89°	3.48°	3.15°	2.88°	2.65°	2.45°	2.13°
$w_{bt, \mathbf{q}_1}^{3,2}$	278.9283 -89.6432i	335.1422 -44.9085i	374.0698 +32.1071i	720.6046 -379.2375i	867.6221 -424.0331i	1017.7006 -462.4674i	0.0000 +0.0000i
$w_{bt, -2\mathbf{q}_1}^{0,0}$	0.2850 +0.0539i	0.2879 +0.0712i	0.2899 +0.0859i	0.2851 +0.1054i	0.2848 +0.1156i	0.2845 +0.1196i	0.2966 +0.1193i
$w_{bt, -2\mathbf{q}_1}^{1,0}$	0.7784 +0.6579i	0.8356 +0.6790i	0.9166 +0.7039i	0.9425 +0.7438i	1.0313 +0.7745i	1.1197 +0.7915i	1.3048 +0.9824i
$w_{bt, -2\mathbf{q}_1}^{2,0}$	0.1800 +0.4639i	0.3922 +0.4884i	0.6837 +0.4814i	1.3663 +0.4078i	1.7086 +0.3961i	2.0704 +0.3373i	3.1202 -0.0032i
$w_{bt, -2\mathbf{q}_1}^{1,1}$	0.5697 +0.4179i	0.5923 +0.4655i	0.6399 +0.6189i	0.6259 +0.2776i	0.6502 +0.2956i	0.6824 +0.3748i	-0.5040 +0.7077i
$w_{bt, -2\mathbf{q}_1}^{3,0}$	1.9726 +3.6649i	2.2326 +3.9437i	2.5091 +4.2928i	1.7359 +6.1916i	2.0398 +6.4838i	2.3898 +6.4937i	3.6069 +4.3530i
$w_{bt, -2\mathbf{q}_1}^{2,1}$	-12.9060 +1.3296i	-13.5889 +0.6897i	-14.5528 +0.2534i	-13.1604 -2.9759i	-13.5268 -3.8690i	-13.9948 -4.3758i	-15.1003 -16.8051i
$w_{bt, -2\mathbf{q}_1}^{4,0}$	2.8324 +2.7961i	4.8170 +3.5647i	6.8604 +4.4465i	4.8093 +4.8720i	7.7070 +7.6197i	11.3328 +10.6154i	4.7718 +11.3466i
$w_{bt, -2\mathbf{q}_1}^{3,1}$	-5.4786 -2.7315i	-4.0707 -6.6935i	-2.7699 -11.5255i	-5.9283 -9.8514i	-5.5694 -16.9323i	-5.5947 -24.6309i	-0.4321 -32.2313i
$w_{bt, -2\mathbf{q}_1}^{2,2}$	-13.3908 +1.5486i	-16.0691 +0.4196i	-19.6850 -2.3332i	-20.2098 -0.4660i	-24.5755 -1.6640i	-29.6960 -3.9203i	-22.3664 -14.8856i
$w_{bt, -2\mathbf{q}_1}^{5,0}$	-6.5309 +1.8069i	-4.7762 +3.3829i	-2.0998 +5.1135i	-8.5977 +9.5616i	-10.4672 +15.0843i	-12.4960 +23.0401i	0.0000 +0.0000i
$w_{bt, -2\mathbf{q}_1}^{4,1}$	-17.7993 -26.0968i	-15.6049 -31.0140i	-12.8970 -37.1812i	-5.7387 -52.6560i	4.2528 -65.3821i	15.9858 -78.8300i	0.0000 +0.0000i
$w_{bt, -2\mathbf{q}_1}^{3,2}$	14.6571 -17.5492i	15.1868 -26.3728i	16.9537 -42.0210i	15.2898 -20.2073i	10.3619 -34.7902i	3.3332 -58.2874i	0.0000 +0.0000i
$w_{bt, \mathbf{q}_1 + \mathbf{b}_{M_2}}^{0,0}$	0.0000 +0.0000i	0.0000 +0.0000i	0.0000 +0.0000i	-0.3014 +0.0642i	-0.4147 +0.0869i	-0.5055 +0.1006i	-0.6533 +0.1170i
$w_{bt, \mathbf{q}_1 + \mathbf{b}_{M_2}}^{1,0}$	0.0000 +0.0000i	0.0000 +0.0000i	0.0000 +0.0000i	1.0839 -0.0944i	1.3773 -0.1659i	1.6262 -0.2180i	2.0158 -0.2975i
$w_{bt, \mathbf{q}_1 + \mathbf{b}_{M_2}}^{0,1}$	0.0000 +0.0000i	0.0000 +0.0000i	0.0000 +0.0000i	0.1360 -0.7189i	0.2670 -1.0388i	0.4030 -1.2796i	0.6223 -1.6246i
$w_{bt, \mathbf{q}_1 + \mathbf{b}_{M_2}}^{2,0}$	0.0000 +0.0000i	0.0000 +0.0000i	0.0000 +0.0000i	3.5853 -1.0831i	4.8002 -1.2430i	5.8089 -1.3438i	7.3066 -1.2708i
$w_{bt, \mathbf{q}_1 + \mathbf{b}_{M_2}}^{1,1}$	0.0000 +0.0000i	0.0000 +0.0000i	0.0000 +0.0000i	-0.1860 +1.3866i	0.1123 +1.6577i	0.3334 +1.8765i	1.0695 +1.6966i
$w_{bt, \mathbf{q}_1 + \mathbf{b}_{M_2}}^{0,2}$	0.0000 +0.0000i	0.0000 +0.0000i	0.0000 +0.0000i	2.0084 +0.7507i	2.8273 +1.0482i	3.5507 +1.2763i	4.5168 +1.1262i
$w_{bt, \mathbf{q}_1 + \mathbf{b}_{M_2}}^{3,0}$	0.0000 +0.0000i	0.0000 +0.0000i	0.0000 +0.0000i	-1.8015 -0.5620i	-3.0872 -0.3325i	-4.3664 -0.1909i	-5.4558 -1.0216i
$w_{bt, \mathbf{q}_1 + \mathbf{b}_{M_2}}^{2,1}$	0.0000 +0.0000i	0.0000 +0.0000i	0.0000 +0.0000i	-9.3540 +9.1064i	-12.8705 +11.7410i	-16.0044 +13.8310i	-17.2554 +15.9246i
$w_{bt, \mathbf{q}_1 + \mathbf{b}_{M_2}}^{1,2}$	0.0000 +0.0000i	0.0000 +0.0000i	0.0000 +0.0000i	-4.6981 +0.5055i	-6.7366 +2.7696i	-8.7304 +4.8106i	-6.3406 +10.1090i
$w_{bt, \mathbf{q}_1 + \mathbf{b}_{M_2}}^{0,3}$	0.0000 +0.0000i	0.0000 +0.0000i	0.0000 +0.0000i	-1.8441 -0.5304i	-2.8286 -1.5153i	-3.5814 -2.4608i	-2.5461 -2.5596i

TABLE XVII: Interlayer potential term parameters (meV) for the full model of  $tWSe_2$  based on DFT with quick basis selection (continued)

Parameter	3.89°	3.48°	3.15°	2.88°	2.65°	2.45°	2.13°
$w_{bt, \mathbf{q}_1 + \mathbf{b}_{M_2}}^{4,0}$	0.0000 +0.0000i	0.0000 +0.0000i	0.0000 +0.0000i	8.0910 -4.5452i	10.8819 -5.2847i	13.4606 -5.1068i	11.5819 +1.0441i
$w_{bt, \mathbf{q}_1 + \mathbf{b}_{M_2}}^{3,1}$	0.0000 +0.0000i	0.0000 +0.0000i	0.0000 +0.0000i	-15.6022 +1.4144i	-20.4952 +1.5723i	-24.8910 +1.4013i	-29.9460 -2.0915i
$w_{bt, \mathbf{q}_1 + \mathbf{b}_{M_2}}^{2,2}$	0.0000 +0.0000i	0.0000 +0.0000i	0.0000 +0.0000i	-5.5274 -35.1804i	-6.9522 -47.5429i	-6.5161 -58.8199i	-23.2043 -46.6297i
$w_{bt, \mathbf{q}_1 + \mathbf{b}_{M_2}}^{1,3}$	0.0000 +0.0000i	0.0000 +0.0000i	0.0000 +0.0000i	-17.0717 -6.9603i	-24.5700 -14.7214i	-32.8380 -23.6809i	-22.9754 -16.7535i
$w_{bt, \mathbf{q}_1 + \mathbf{b}_{M_2}}^{0,4}$	0.0000 +0.0000i	0.0000 +0.0000i	0.0000 +0.0000i	0.0202 -1.0291i	0.3063 -0.5834i	0.7861 +0.1684i	8.3973 -5.4793i
$w_{bt, \mathbf{q}_1 + \mathbf{b}_{M_2}}^{5,0}$	0.0000 +0.0000i	0.0000 +0.0000i	0.0000 +0.0000i	-10.0630 -4.9676i	-12.8657 -7.1829i	-14.5737 -10.2411i	0.0000 +0.0000i
$w_{bt, \mathbf{q}_1 + \mathbf{b}_{M_2}}^{4,1}$	0.0000 +0.0000i	0.0000 +0.0000i	0.0000 +0.0000i	9.0862 +19.7285i	13.0157 +19.1553i	16.1471 +15.5724i	0.0000 +0.0000i
$w_{bt, \mathbf{q}_1 + \mathbf{b}_{M_2}}^{3,2}$	0.0000 +0.0000i	0.0000 +0.0000i	0.0000 +0.0000i	13.5740 -2.2947i	18.8303 -4.7188i	23.0189 -6.8534i	0.0000 +0.0000i
$w_{bt, \mathbf{q}_1 + \mathbf{b}_{M_2}}^{2,3}$	0.0000 +0.0000i	0.0000 +0.0000i	0.0000 +0.0000i	79.8565 +43.0460i	105.4207 +64.9509i	126.9117 +95.3477i	0.0000 +0.0000i
$w_{bt, \mathbf{q}_1 + \mathbf{b}_{M_2}}^{1,4}$	0.0000 +0.0000i	0.0000 +0.0000i	0.0000 +0.0000i	33.1817 +5.0467i	57.5895 +14.0096i	85.0958 +24.0737i	0.0000 +0.0000i
$w_{bt, 2\mathbf{b}_{M_2} + \mathbf{q}_3}^{0,0}$	0.0000 +0.0000i	0.0000 +0.0000i	0.0000 +0.0000i	0.0842 -0.0258i	0.1033 -0.0112i	0.1169 +0.0036i	0.0000 +0.0000i
$w_{bt, 2\mathbf{b}_{M_2} + \mathbf{q}_3}^{1,0}$	0.0000 +0.0000i	0.0000 +0.0000i	0.0000 +0.0000i	-0.1616 +0.1523i	-0.2025 +0.1754i	-0.2352 +0.1892i	0.0000 +0.0000i
$w_{bt, 2\mathbf{b}_{M_2} + \mathbf{q}_3}^{0,1}$	0.0000 +0.0000i	0.0000 +0.0000i	0.0000 +0.0000i	0.1128 +0.1342i	0.1041 +0.1087i	0.0957 +0.0687i	0.0000 +0.0000i
$w_{bt, 2\mathbf{b}_{M_2} + \mathbf{q}_3}^{2,0}$	0.0000 +0.0000i	0.0000 +0.0000i	0.0000 +0.0000i	-0.5304 +0.1677i	-0.6465 +0.0591i	-0.7909 -0.0595i	0.0000 +0.0000i
$w_{bt, 2\mathbf{b}_{M_2} + \mathbf{q}_3}^{1,1}$	0.0000 +0.0000i	0.0000 +0.0000i	0.0000 +0.0000i	0.1355 -0.5836i	-0.0097 -0.6528i	-0.2156 -0.6283i	0.0000 +0.0000i
$w_{bt, 2\mathbf{b}_{M_2} + \mathbf{q}_3}^{0,2}$	0.0000 +0.0000i	0.0000 +0.0000i	0.0000 +0.0000i	-0.5027 -0.4351i	-0.4636 -0.4874i	-0.3852 -0.4462i	0.0000 +0.0000i
$w_{bt, 2\mathbf{b}_{M_2} + \mathbf{q}_3}^{3,0}$	0.0000 +0.0000i	0.0000 +0.0000i	0.0000 +0.0000i	-0.5474 -1.9466i	0.6348 -1.3498i	2.6041 -0.0548i	0.0000 +0.0000i
$w_{bt, 2\mathbf{b}_{M_2} + \mathbf{q}_3}^{2,1}$	0.0000 +0.0000i	0.0000 +0.0000i	0.0000 +0.0000i	-4.1973 -3.7784i	-1.9870 -5.8386i	2.3058 -8.3385i	0.0000 +0.0000i
$w_{bt, 2\mathbf{b}_{M_2} + \mathbf{q}_3}^{1,2}$	0.0000 +0.0000i	0.0000 +0.0000i	0.0000 +0.0000i	-0.1141 +1.7389i	0.4803 +0.7196i	1.3523 -1.4482i	0.0000 +0.0000i
$w_{bt, 2\mathbf{b}_{M_2} + \mathbf{q}_3}^{0,3}$	0.0000 +0.0000i	0.0000 +0.0000i	0.0000 +0.0000i	0.1212 +0.7841i	-0.1977 +0.9012i	-0.7118 +0.8548i	0.0000 +0.0000i
$w_{bt, 2\mathbf{b}_{M_2} + \mathbf{q}_3}^{4,0}$	0.0000 +0.0000i	0.0000 +0.0000i	0.0000 +0.0000i	-2.2874 +9.8886i	-5.9493 +7.4764i	-11.5575 +0.5352i	0.0000 +0.0000i
$w_{bt, 2\mathbf{b}_{M_2} + \mathbf{q}_3}^{3,1}$	0.0000 +0.0000i	0.0000 +0.0000i	0.0000 +0.0000i	21.5201 +13.7126i	8.9715 +19.9814i	-18.5649 +24.6815i	0.0000 +0.0000i
$w_{bt, 2\mathbf{b}_{M_2} + \mathbf{q}_3}^{2,2}$	0.0000 +0.0000i	0.0000 +0.0000i	0.0000 +0.0000i	24.1533 -2.0701i	25.6329 +11.5045i	19.7997 +36.2439i	0.0000 +0.0000i

TABLE XVII: Interlayer potential term parameters (meV) for the full model of  $tWSe_2$  based on DFT with quick basis selection (continued)

Parameter	3.89°	3.48°	3.15°	2.88°	2.65°	2.45°	2.13°
$w_{bt,2b_{M_2}+q_3}^{1,3}$	0.0000 +0.0000i	0.0000 +0.0000i	0.0000 +0.0000i	4.2298 -5.4305i	7.3359 -3.8520i	12.0320 +0.3294i	0.0000 +0.0000i
$w_{bt,2b_{M_2}+q_3}^{5,0}$	0.0000 +0.0000i	0.0000 +0.0000i	0.0000 +0.0000i	8.2488 -5.1479i	11.6939 -0.5587i	15.3053 +10.6114i	0.0000 +0.0000i
$w_{bt,2b_{M_2}+q_3}^{4,1}$	0.0000 +0.0000i	0.0000 +0.0000i	0.0000 +0.0000i	-17.3146 -34.9084i	0.8406 -38.1226i	40.5428 -27.9851i	0.0000 +0.0000i
$w_{bt,2b_{M_2}+q_3}^{3,2}$	0.0000 +0.0000i	0.0000 +0.0000i	0.0000 +0.0000i	-35.2483 -7.7293i	-20.9670 -37.8133i	26.4161 -88.6810i	0.0000 +0.0000i
$w_{bt,2b_{M_2}+q_3}^{2,3}$	0.0000 +0.0000i	0.0000 +0.0000i	0.0000 +0.0000i	-35.2630 +22.2522i	-57.9236 +13.4750i	-87.4989 -13.6683i	0.0000 +0.0000i

TABLE XVIII: Kinetic term parameters ( $m_e$ ) for the reduced model of  $tWSe_2$  based on DFT with quick basis selection

Parameter	3.89°	3.48°	3.15°	2.88°	2.65°	2.45°	2.13°
$m^{(1,1)}$	-0.3965	-0.3860	-0.3860	-0.3803	-0.3750	-0.3713	-0.3853

TABLE XIX: Intralayer potential term parameters (meV) for the reduced model of  $tWSe_2$  based on DFT with quick basis selection

Parameter	3.89°	3.48°	3.15°	2.88°	2.65°	2.45°	2.13°
$V_{b,b_{M_1}}^{0,0}$	-0.1913 -1.2485i	-0.1762 -1.3517i	-0.1669 -1.4073i	-0.1567 -1.4314i	-0.1439 -1.3999i	-0.1286 -1.2921i	-0.0598 -1.0488i
$V_{b,b_{M_1}}^{-1,0}$	-0.4066 -6.3732i	-0.6328 -7.2648i	-0.8188 -8.1045i	-0.9840 -8.9102i	-1.1117 -9.5387i	-1.1983 -9.8904i	-0.9508 -8.7636i
$V_{b,b_{M_1}}^{0,1}$	-0.0652 -3.7127i	-0.0689 -3.3704i	-0.0383 -2.9257i	-0.0593 -2.3935i	-0.1007 -1.8066i	-0.1447 -1.1752i	-0.2901 -1.3467i
$V_{b,b_{M_1}}^{2,0}$	9.7572 -32.1432i	10.0103 -37.1088i	9.9871 -41.9246i	10.1418 -46.5919i	9.9096 -50.4116i	9.3107 -52.8176i	0.3733 -38.7032i
$V_{b,b_{M_1}}^{1,1}$	6.5502 -1.5134i	6.7676 -1.7685i	6.9057 -2.0282i	7.1451 -2.2278i	7.3472 -2.3578i	7.3941 -2.5075i	-1.0326 +26.2541i
$V_{b,b_{M_1}}^{-0,2}$	-1.2546 +29.5330i	-1.5859 +34.3473i	-1.8994 +38.9635i	-2.0313 +43.4155i	-2.0594 +47.0410i	-1.9897 +49.3347i	2.4546 +52.2043i
$V_{b,b_{M_1}}^{3,0}$	-27.6183 +16.0654i	-30.5199 +17.1749i	-32.6387 +18.1845i	-34.3750 +18.7236i	-34.1981 +19.2402i	-32.0344 +19.5151i	0.0000 +0.0000i
$V_{b,b_{M_1}}^{2,1}$	-51.4849 +105.3457i	-55.1189 +138.4381i	-57.0249 +174.1857i	-59.3747 +211.9248i	-59.3516 +248.2216i	-56.3812 +279.8551i	0.0000 +0.0000i

TABLE XX: Interlayer potential term parameters (meV) for the reduced model of  $tWSe_2$  based on DFT with quick basis selection

Parameter	3.89°	3.48°	3.15°	2.88°	2.65°	2.45°	2.13°
$w_{bt,q_1}^{0,0}$	-1.4353 +0.6807i	-1.4659 +0.6316i	-1.4714 +0.5859i	-1.4457 +0.5286i	-1.4218 +0.4902i	-1.3944 +0.4548i	-1.3615 +0.3423i

TABLE XX: Interlayer potential term parameters (meV) for the reduced model of  $tWSe_2$  based on DFT with quick basis selection (continued)

Parameter	3.89°	3.48°	3.15°	2.88°	2.65°	2.45°	2.13°
$w_{bt, \mathbf{q}_1}^{1,0}$	11.1468 -3.7369i	11.7726 -3.6184i	12.3556 -3.5287i	12.6550 -3.3937i	13.1239 -3.3038i	13.5219 -3.1885i	12.2244 -1.7896i
$w_{bt, \mathbf{q}_1}^{2,0}$	39.3527 -5.4324i	41.0136 -3.9625i	42.4871 -2.7414i	43.3656 -1.5919i	44.4125 -0.6968i	45.0791 +0.0157i	42.4213 +0.4730i
$w_{bt, \mathbf{q}_1}^{1,1}$	-14.7780 -0.8024i	-14.6769 -1.2283i	-14.7217 -1.6199i	-14.6642 -2.0556i	-14.9222 -2.4869i	-15.0942 -2.8917i	-10.5945 +3.1713i
$w_{bt, \mathbf{q}_1}^{3,0}$	-34.4507 -9.0606i	-36.2372 -11.1027i	-37.5416 -12.8291i	-37.1984 -14.2029i	-37.8977 -15.1069i	-38.6026 -15.4044i	0.0000 +0.0000i
$w_{bt, \mathbf{q}_1}^{2,1}$	-78.9933 +64.9710i	-90.9334 +70.9916i	-101.6991 +77.5258i	-110.5890 +84.1201i	-119.2994 +90.9022i	-127.2793 +95.7934i	0.0000 +0.0000i
$w_{bt, -2\mathbf{q}_1}^{0,0}$	0.2976 +0.0966i	0.2961 +0.1075i	0.2952 +0.1191i	0.2907 +0.1315i	0.2878 +0.1396i	0.2855 +0.1421i	0.2852 +0.1393i
$w_{bt, -2\mathbf{q}_1}^{1,0}$	0.5248 +0.6304i	0.6068 +0.6476i	0.6927 +0.6668i	0.7555 +0.6711i	0.8321 +0.6766i	0.9087 +0.6726i	1.0885 +0.6888i
$w_{bt, -2\mathbf{q}_1}^{2,0}$	0.4074 +1.0741i	0.5685 +0.9723i	0.7737 +0.8321i	0.9670 +0.6428i	1.1913 +0.3962i	1.4402 +0.1350i	1.4050 -0.0880i
$w_{bt, -2\mathbf{q}_1}^{1,1}$	-0.4489 -1.8491i	-0.2780 -1.8867i	-0.1610 -1.9460i	-0.1502 -2.0039i	-0.1989 -2.0930i	-0.3153 -2.1772i	-0.7344 -2.3647i
$w_{bt, -2\mathbf{q}_1}^{3,0}$	-0.0884 +3.8059i	-0.1631 +4.3926i	-0.2142 +4.9179i	-0.2230 +5.2604i	0.0299 +5.3952i	0.4830 +5.2417i	0.0000 +0.0000i